LAWRENCE
LIVERMORE
NATIONAL
LABORATORY

UCRL-TH-225651

Fast Ignition Experimental and Theoretical Studies

K.U. Akli

October 20, 2006

This work was performed under the auspices of the U.S. Department of Energy by University of California, Lawrence Livermore National Laboratory under Contract W-7405-Eng-48.

Fast Ignition Experimental and Theoretical Studies

by

Kramer Ugerthen Akli

B.A. (Moscow Engineering and Physics Institute) 1998
M.S. (University of California Davis) 2002

A dissertation submitted in partial satisfaction of the
requirements for the degree of
Doctor of Philosophy

in

Engineering-Applied Science

in the

GRADUATE DIVISION
of the
UNIVERSITY OF CALIFORNIA, DAVIS

Committee in charge:
Prof. Richard R. Freeman, Chair
Dr. Michael H. Key
Dr. William L. Kruer

2006

Fast Ignition Experimental and Theoretical Studies

Kramer Ugerthen Akli

Abstract

Fast Ignition Experimental and Theoretical Studies

by

Kramer Ugerthen Akli

Doctor of Philosophy in Engineering-Applied Science

University of California, Davis

Prof. Richard R. Freeman, Chair

We are becoming dependent on energy more today than we were a century ago, and with increasing world population and booming economies, sooner or later our energy sources will be exhausted. Moreover, our economy and welfare strongly depends on foreign oil and in the shadow of political uncertainties, there is an urgent need for a reliable, safe, and cheap energy source. Thermonuclear fusion, if achieved, is that source of energy which not only will satisfy our demand for today but also for centuries to come. Today, there are two major approaches to achieve fusion: magnetic confinement fusion (MFE) and inertial confinement fusion (ICF). This dissertation explores the inertial confinement fusion using the fast ignition concept. Unlike the conventional approach where the same laser is used for compression and ignition, in fast ignition separate laser beams are used. This dissertation addresses three very im-

portant topics to fast ignition inertial confinement fusion. These are laser-to-electron coupling efficiency, laser-generated electron beam transport, and the associated isochoric heating.

First, an integrated fast ignition experiment is carried out with 0.9 kJ of energy in the compression beam and 70 J in the ignition beam. Measurements of absolute K_α yield from the imploded core revealed that about 17% of the laser energy is coupled to the suprathermal electrons. Modeling of the transport of these electrons and the associated isochoric heating, with the previously determined laser-to-electron conversion efficiency, showed a maximum target temperature of 166 eV at the front where the electron flux is higher and the density is lower. The contribution of the potential, induced by charge separation, in opposing the motion of the electrons was moderate. Second, temperature sensitivity of Cu K_α imaging efficiency using a spherical Bragg reflecting crystal is investigated. It was found that due to the shifting and broadening of the K_α line, with increasing temperature, both the brightness and the pattern of K_α intensity are affected. Finally, x-ray spectroscopy of a 500 J 0.7 ps laser-solid interactions showed the formation of a hot surface layer($\sim$1 μm) at the front of the target. PIC simulations confirm surface heating.

Prof. Richard R. Freeman
Dissertation Committee Chair

Contents

List of Figures

List of Tables

Acknowledgments

Chapter 1

Introduction

1.1 Motivation for this work

It has been over 50 years since the first steps toward achieving fusion were taken and fusion power plants seem as far from reality today as they were yesterday. The question is: do we really need to keep investing in fusion?

The short answer is yes. The fact is we are becoming more and more dependent on energy as never before. On a personal basis we need energy to cook our food, heat our houses, and drive our cars. As a society we need energy to grow our food, light our schools, and power our hospitals. As Fig. 1.1 shows, most of our energy consumption comes from fossil fuel such as oil, coal, and natural gas. These forms of energy are non-renewable and there are varying estimates of how many reserves are still out there. But one thing people agree on is that sooner or later they will be

exhausted. In addition, these mineral fuels are more abundant in certain countries than others and the thirst for them is already causing conflicts.

According to the energy information administration (EIA), the total world energy consumption in 2003 was 421 Quads [1] compared to only 283 Quads in 1980 (Fig. 1.2), and it is projected to reach 722 Quads by 2030 [1]. Even if we had limitless sources of fossil fuels, their impact on the environment would be a destructive one. Carbon dioxide is one of the green house gases causing global warming, and by burning fossil fuels a huge amount of it is released into the atmosphere.

It is clear that our dependence on energy is permanent and we need reliable and environment friendly sources. It is worthwhile to explore all of our options, if not for us, then for generations to come. Fusion will likely be the ultimate source of energy for the future. Achieving it has turned out to be a challenging task and scientists all over the world are teaming up in the pursuit of this dream. The work in this dissertation is no exception: It is motivated by the same reasons, driven by the same dream, and carried out in collaboration with national and international teams.

[1] Quad = One quadrillion British thermal units (BTU)

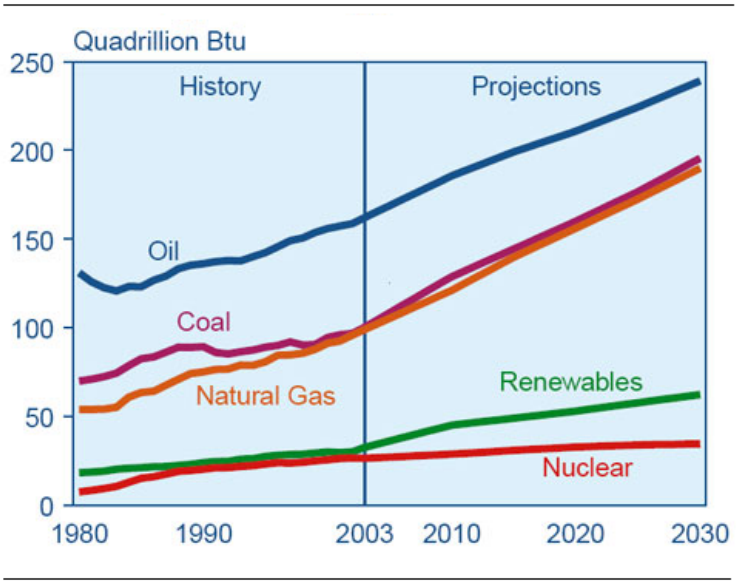

Figure 1.1: World Marketed Energy consumption by fuel type (1980-2030). Source: energy information administration (EIA), http://www.eia.doe.gov/oiaf/ieo.

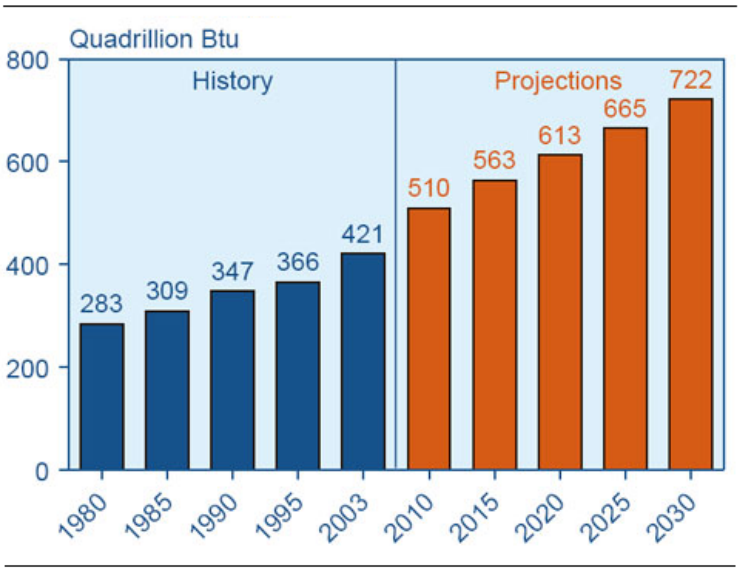

Figure 1.2: World Marketed Energy consumption (1980-2030). Source: energy information administration (EIA), http://www.eia.doe.gov/oiaf/ieo.

1.2 Inertial confinement fusion basics

1.2.1 Binding energy

Fusion is the nuclear reaction by which two light nuclei combine or fuse to form a heavier nucleus. It is an exothermic [2] reaction where mass is transformed to energy according to,

$$\Delta E = \Delta m \; c^2 \tag{1.1}$$

where c the speed of light in vacuum, Δm is the mass difference between the products and reactants. This mass defect was first discovered by Francis Aston using his newly invented mass spectrograph [2]. While attempting to find neon isotopes, Aston precisely measured the masses of different atoms including Hydrogen and Helium. He discovered that the mass of one Helium nucleus is smaller than the mass of four Hydrogen nuclei. This result was significant and led the Astrophysicist Arthur Eddington to suggest that the energy of stars is the result of the nuclear fusion of hydrogen [3].

" Aston has further shown concisely that the mass of the Helium atom is less than the sum of the masses of the four Hydrogen atoms which enters into it... There is a loss of mass in the synthesis amounting to 1 part in 120, the atomic weight of hydrogen being 1.008 and that of Helium is just 4.00... Now mass cannot be annihilated and the deficit can only represent the mass of the electrical energy liberated when helium

[2] An exothermic reaction is a reaction which is accompanied by energy release as opposed to an endothermic one

is made out of hydrogen. If 5% of a star's mass consists initially of hydrogen atoms, which are gradually being combined to form more complex elements, the total heat liberated will more than suffice for our demands, and we need look no further for the source of stars' energy......"

Arthur Eddington

British Association of advancement of Science 1920

Using Aston's results and Einstein's mass-energy equivalence principle, the mass M(A,Z) of a nucleus with mass number A and atomic number Z is given by the expression,

$$M(A,Z) = Zm_p + (A-Z)m_n - \Delta E(A,Z)\ c^2 \tag{1.2}$$

where m_p and m_n are the proton mass and neutron mass respectively. The energy, $\Delta E(A,Z)$, released when the neutrons and protons combine to form the nucleus is called the binding energy of the nucleus. This energy can be approximated by *Weizscker's* formula also known as the *semi-empirical formula* [4, 5],

$$\Delta E = \underbrace{\alpha\, A}_{nuclear\ attraction} - \overbrace{\beta\, A^{\frac{2}{3}}}^{surface\ effect} - \underbrace{\gamma\, \frac{Z^2}{A^{\frac{1}{3}}}}_{Coulomb\ force} - \overbrace{\zeta\, \frac{(\frac{a}{2}-Z)^2}{A}}^{strong\ force} - \underbrace{\delta\, A^{\frac{-3}{4}}}_{parity-parity} \tag{1.3}$$

where

$$\delta = \begin{cases} 34\ MeV & for\ even-even\ nuclei \\ 0\ MeV & for\ odd-odd\ nuclei \\ -34\ Mev & for\ even-odd\ nuclei \end{cases} \tag{1.4}$$

and

$$\begin{pmatrix} \alpha \\ \beta \\ \gamma \\ \zeta \end{pmatrix} = \begin{pmatrix} 15.75\ MeV \\ 17.8\ MeV \\ 0.71\ MeV \\ 94.8\ MeV \end{pmatrix} \tag{1.5}$$

The binding energy per nucleon, $\Delta E/A$, is plotted in Fig. (1.3) as a function of the number of nucleons. For elements up to Iron, the energy per nucleon increases with increasing A. This tells us that more energy will be released if we combine light nuclei to form a heavier one and this is exactly what nuclear fusion is about. The curve also tells us that energy is released if we split heavier elements (nuclear fission).

1.2.2 Possible fusion fuel

In order for two nuclei to fuse they must be brought close to each other such that the strong nuclear force dominates the repulsive Coulomb force. Since this Coulomb force preventing two nuclei from getting closer is an increasing function of the atomic number Z, the most promising fusion reactions are those involving Hydrogen and its

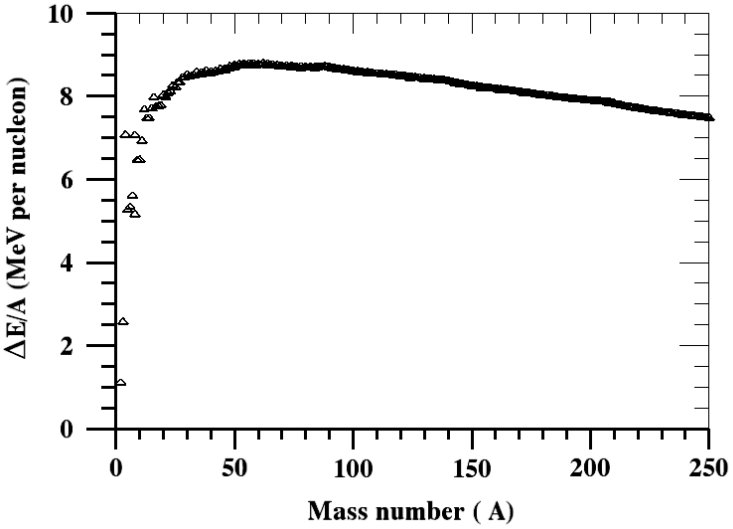

Figure 1.3: Binding energy per nucleon.

isotopes, namely Deuterium and Tritium. The most widely investigated reactions are the so-called DD-reaction and DT-reaction listed below.

The DD-reaction

$$D + D \longrightarrow \begin{cases} {}^3He + n + 3.27\ MeV \\ T + p + 4.03\ MeV \end{cases} \tag{1.6}$$

The DT-reaction

$$D + T \longrightarrow {}^4He + n + 17.6\ MeV \tag{1.7}$$

There are also other reactions of interest labelled as advanced fusion fuel such as,

$$B + p \longrightarrow^{4} He + 8.6\ MeV \tag{1.8}$$

The feasibility of these reactions for energy production on earth is often discussed in terms of both the cross section and the reaction rate. The rate of thermonuclear reaction is a function of the reaction cross section, temperature , and density. For a mixture of two species with densities n_1 and n_2, the reaction rate is given by the expression [6],

$$R_{ij} = \frac{n_i n_j}{1 + \delta_{ij}} \sigma v \quad interactions/(cm^3)\ (sec) \tag{1.9}$$

where σ is the reaction cross section and δ_{ij} is the Kronecker symbol .

If the fusion is " *Thermonuclear*", i.e. If the energy provided to the reacting particles is the result of heating the system to a temperature T, then we need to used the averaged σv. Assuming a Maxwellian distribution, equation (1.9) becomes,

$$R_{ij} = \frac{n_i n_j}{1 + \delta_{ij}} < \sigma v > \ = \frac{n_i n_j}{1 + \delta_{ij}} \left[\frac{8}{\pi \mu}\right]^{3/2} \left[\frac{1}{kT}\right]^{3/2} \int \sigma(E) E \exp - \left[\frac{E}{kT}\right]\ dE \tag{1.10}$$

where μ is the reduced mass of the interacting particles.

Since the DT-reaction has the highest reaction rate at relatively low fuel temperature, it is the easiest fuel to assemble and burn. However, the presence of neutrons as a product (see eq. (1.7)) makes it unattractive for fusion reactors.

1.2.3 Gain requirement

In order for fusion to be economically an attractive energy source it is necessary that the energy from thermonuclear reaction exceeds both the energy invested in achieving it and the losses due to radiation, reactor wall, conversion inefficiencies, etc. A simple estimate of the driver efficiency and target gain can be obtained using energy bookkeeping approach (Rosen 1999).

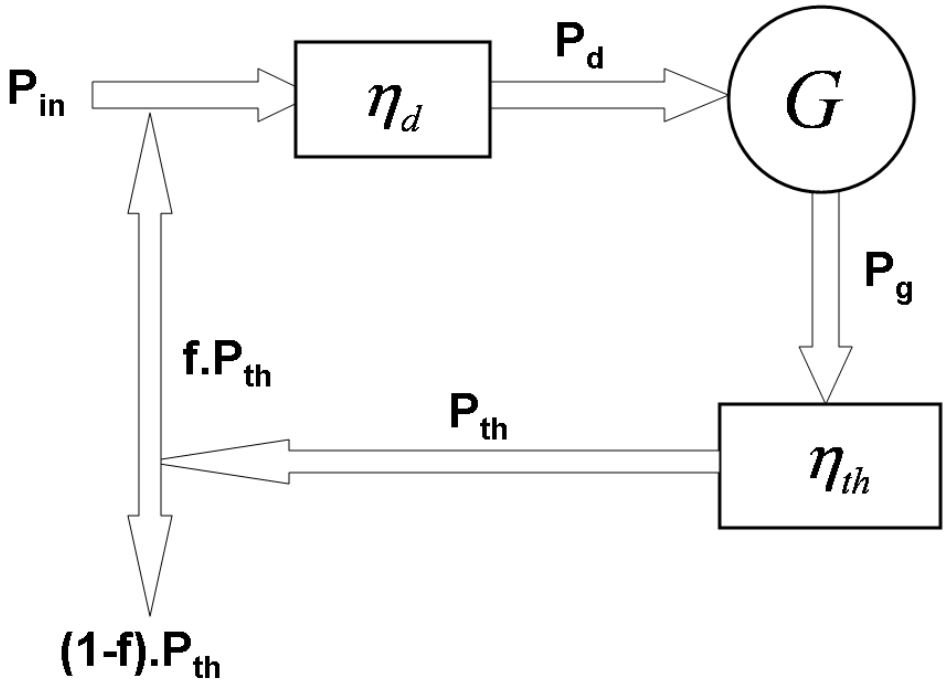

Figure 1.4: Power cycle. P_{in}, The input power (This could be the electrical power from the outlet). P_d, The power at the output of the driver. P_g, the power from thermonuclear fusion. P_{th}, the power after converting the thermal energy to electrical energy

Let P_{in} be the electrical power that we intend to invest in achieving fusion and let

η_d be the efficiency of conversion of this power to laser light power P_d. If we define the target gain as the ratio of the power obtained from the fusion reaction to the driver power, then

$$P_g = G\ P_d\ = G\ \eta_d\ P_{in} \tag{1.11}$$

taking into account the conversion efficiency from thermal to electrical power, the available electrical power is given by,

$$P_{th} = \eta_{th}\ P_g\ = G\ \eta_{th}\ \eta_d\ P_{in} \tag{1.12}$$

A fraction $f\ G\ \eta_{th}\ \eta_d\ P_{in}$ of this power is used to run the driver and the remaining fraction $(1-f)\ G\ \eta_{th}\ \eta_d\ P_{in}$ is send to the customers. The closer the factor $(1-f)$ to unity, the more electricity is available to customers. This can be achieved by using small values of f, however, f has a lower bound determined by the equation,

$$P_{in} = f_{min}\ G\ \eta_{th}\ \eta_d\ P_{in} \quad \Rightarrow \quad f_{min} = \frac{1}{G\ \eta_{th}\ \eta_d} \tag{1.13}$$

Using a typical η_{th} value of 40% and recycling less than 1/4 of the power to run the driver, we get

$$G\ \eta_d \geq 10 \tag{1.14}$$

Solid state lasers for example have an efficiency of 1-10% [7] and to fulfill the condition in eq. (1.16), gains of 100-1000 are needed.

1.2.4 Lawson criterion

It is a well known fact that hot, confined plasmas lose energy in various ways. These include losses due to radiation [8] and transport across the magnetic field lines [6]. Therefore, a fusion reactor would be useful only if the energy produced is more than the energy consumed in heating and confining the fuel. The minimum condition for the operation of the reactor was first derived by J. D. Lawson and reported in his article "Some Criteria for a Useful Thermonuclear Reactor" [9]. This condition known as "Lawson criterion" states that the product of the plasma density and confinement time must be bigger than or equal to a certain minimum value.

$$n\ \tau \geq 10^{14} s/cm^3 \quad for\ the\ DT-reaction \tag{1.15}$$

$$n\ \tau \geq 10^{16} s/cm^3 \quad for\ the\ DD-reaction \tag{1.16}$$

This criterion, which was first derived for magnetically confined plasmas, has an analogue for the inertially confined ones. But, Instead of $n\ \tau$ product, the Lawson criterion is expressed in the more convenient $\rho\ R$ product for ICF. Let ρ be the density of the fuel and let R be its radius. If we have a fuel consisting of 50% of Deuterium and 50% of Tritium, then according to eq. (1.10) the reaction rate is,

$$\frac{dn_T}{dt} = -n_T n_D < \sigma_{DT}\ v > \tag{1.17}$$

Since we have equimolar densities, $n_T = n_D = n/2$, then eq. (1.17) becomes,

$$\frac{dn}{dt} = -\frac{n^2}{2} < \sigma\ v > \tag{1.18}$$

integrating this expression from $t = 0$ to the disassembly time $t = \tau_d$ gives,

$$\int_0^{\tau_d} \frac{dn}{dt} = -\int_0^{\tau_d} \frac{n^2}{2} < \sigma\ v > \Rightarrow \frac{1}{n} - \frac{1}{n_0} = \frac{\tau_d}{2} < \sigma\ v > \tag{1.19}$$

here n_0 denotes the initial fuel density. The disassembly time of an assembled high pressure fuel, surrounded by vacuum, can be determined by [10],

$$\tau_d = \int_0^R \rho[(R - r')/C_s] \times 4\pi r'^2 dr'/(4/3)\pi\rho R^3 = \frac{R}{4C_s} \tag{1.20}$$

where C_s is the sound speed.

using this value for τ_d and $n_0 = \rho/m$ in eq. (1.19), we can express the burn fraction as,

$$f_b = \frac{n_0 - n}{n_0} = 1 - \frac{n}{n_0} = \frac{\rho R}{\rho R + \dfrac{8mC_s}{\underbrace{< \sigma\ v >}_{f(T)}}} \tag{1.21}$$

for DT fuel at 20 keV, the function $f(T)$ has a value of 6.3 g/cm^3. The burn fraction is therefore,

$$f_b = \frac{\rho R}{\rho R + 6.3\ g/cm^3} \tag{1.22}$$

If we burn 1/3 of the fuel [3], then the ρR product can be obtained by rearranging eq. (1.22),

$$\rho R = 3\ g/cm^2 \tag{1.23}$$

Unlike magnetic fusion where low densities and long confinement times are used to satisfy the Lawson criterion, in ICF high densities and short confinement times are

[3] In his original paper, A.E.R.E. report GP/R 1807, December 1955, declassified April 9th 1957, Lawson also used a typical value of 1/3

used to achieve the same goal. The high densities can be achieved by compressing the fuel using lasers or ion beams. The inertia of the imploding fuel keeps it together, long enough, for ignition and burn to happen. hence the name " Inertial confinement fusion". Energy from ICF has been demonstrated in devices known as "Hydrogen bombs" but achieving it in controlled fashion turned out to be a challenging task. Scientists all over the world are exploring and investigating new ways to achieve ICF. One such a scheme that has received a lot of attention in the last decade is fast ignition [11].

1.3 Fast ignition

The fast ignition approach to inertial confinement fusion (Tabak 1994) differs from the conventional approach (Lindl 1995) in that the compression and ignition are separated. First, a long pules high intensity laser beam is used to compress the fuel to the required densities. Then, a separate short-pules high-intensity laser is used to generate fast electrons. These relativistic electrons propagate to the dense core where they deposit their energy and ignite the fuel. Since a separate laser is used for ignition, the fuel symmetry requirements are less stringent in FI than conventional approach [12]. But the transport of these relativistic beams from the critical surface to the dense core is not well understood.

1.3.1 Energy requirements

The minimum electron beam energy, power, and intensity required for the ignition of a precompressed DT fuel were determined by Atzeni (1999) as follows:

$$E_{ign} = 140 \left[\frac{\rho}{100\ g/cm^3} \right]^{-1.85} \ kJ \tag{1.24}$$

$$E_{ign} = 2.6 \times 10^{15} \left[\frac{\rho}{100\ g/cm^3} \right]^{-1} \ W \tag{1.25}$$

$$E_{ign} = 2.4 \times 10^{19} \left[\frac{\rho}{100\ g/cm^3} \right]^{0.95} \ W/cm^2 \tag{1.26}$$

Compressing the fuel to a density of $\rho = 100\ g/cm^3$ will require at least 140 kJ of electron beam energy for ignition. On the other hand, If we compress the target to $\rho = 300\ g/cm^3$, the minimum electron energy required is only 18 kJ.

1.3.2 Alfven limit and electron beam transport

If this energy is carried by electrons with a mean energy of 1 MeV, then the associated current can reach a value of several MegaAmpers which is higher than the Alfven limit [13],

$$I_A \simeq \beta\ \gamma\ m\ c^3/e = 17\ \beta\ \gamma\ kA \tag{1.27}$$

In a conductor, a current higher than the Alfven limit cannot propagate because it is stopped by the self-generated magnetic field. In a plasma, the cold background electrons, moving in the opposite direction, tend to locally neutralize the forward currents. However, these opposite currents are susceptible to Weibel instability which may inhibit the electron transport into the dense core [14, 15, 16]. Beam filamentaion and anomalous stopping have been observed with both 2D and 3D PIC simulations [17, 18, 19].

The ability of the material to supply neutralizing return currents have been studied by Bell et al. (1997) using a 1D model. They concluded that the fast electrons propagated deep into the target only if the material is able to supply return currents. Otherwise, the electrons are confined to the surface of the target.

Experiments with CH targets by Koch et al. (2001) showed a columnar structure with enhanced heating at the edges of the column which they attributed to weibel instability [20].

Stephens et al. (2004) investigated the transport of ultrashort high-intensity laser-generated electron beam in solid targets using the tracer layer technique. They observed a divergence in the beam propagation with a 20° half angle.

1.3.3 Plasma resistivity

The response of the medium to the propagating fast electron beam depends on its resistivity. The classical Spitzer resistivity given by the expression,

$$\eta = 5.2 \times 10^{-5} \frac{Z \ln \Lambda}{T^{3/2}(eV)} \ (\Omega \ m) \tag{1.28}$$

is a decreasing function of temperature. Milchberg and Freeman (1988) showed that metals increase their resistivity with temperature, reach a maximum plateau over an extended interval of temperatures, and finally start to decrease at the highest temperatures [21]. As shown in Fig. 1.5, most materials used in electron beam transport studies are in the non-Spitzer regime when their temperature is less than 100 eV. If the possibility of high conductivity channels are to be verified, experiments in the Spitzer regime are needed.

1.3.4 Conversion efficiency

Also of great importance to fast ignition is the question of conversion efficiency of laser light to the relativistic electrons. Experiments with flat targets on the NOVA laser (Key et.al 1998, Wharton et al. 1998) showed more than 30% conversion efficiency at a laser intensity of $2 \times 10^{19} W/cm^2$.

Up to date only two independent integrated fast ignition experiments were conducted, both at a smaller scales than those envisaged for fast ignition. The first experiment conducted with 300 J ignitor beam achieved about 20% coupling effi-

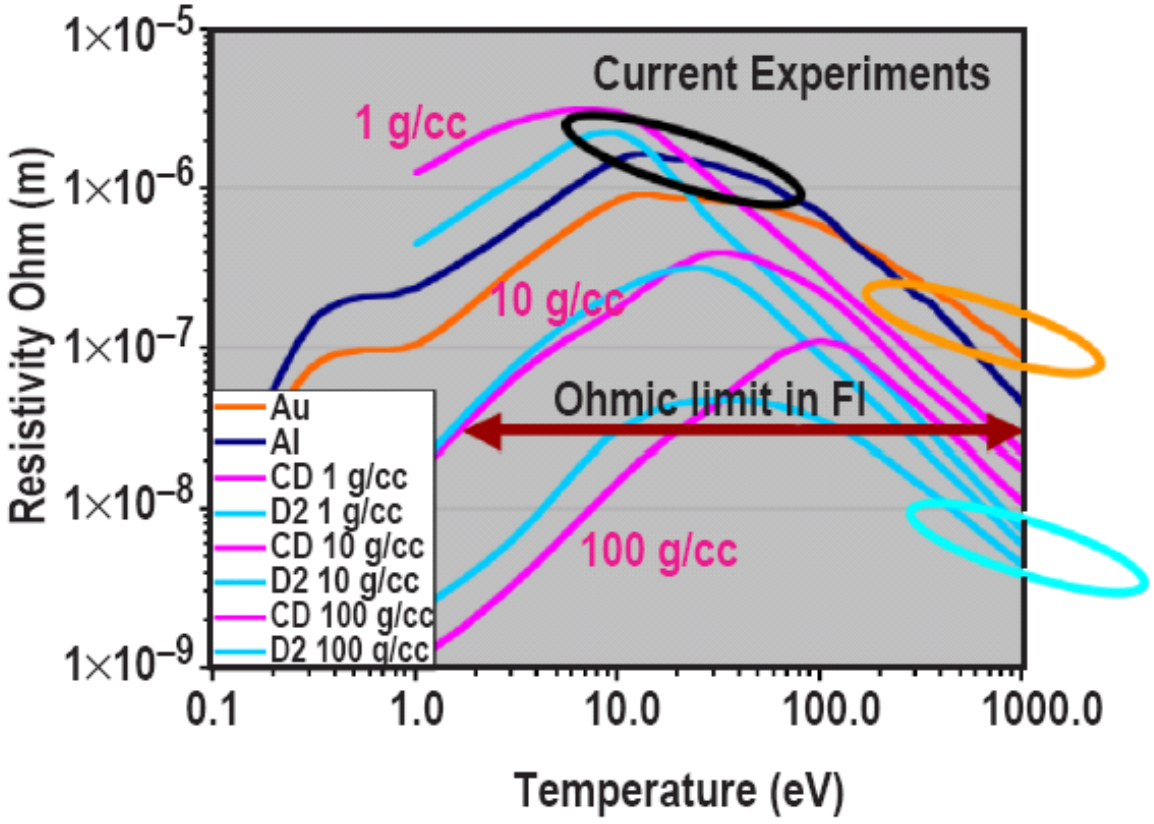

Figure 1.5: Resistivity of of various plasmas as a function of temperature. Source: M.H.Key, Current Trends in International Fusion Research, Washington DC, March 7-11, 2005

ciency (Kodama et al. 2002). The second experiment conducted with a 70 J igniter beam showed a 15% conversion efficiency (Key et. al 2006).

1.4 Structure of the dissertation

This dissertation explores inertial confinement fusion using the fast ignition concept. It addresses three very important topics to fast ignition inertial confinement

fusion. These are laser-to-electron coupling efficiency, laser-generated electron beam transport, and the associated isochoric heating.

The work in this dissertation is divided into three main chapters listed in the chronological order of the experiments.

Chapter 2 deals with the group's first integrated fast ignition experiment conducted in February 2003 on the Vulcan laser in the United Kingdom.

Chapter 3 discusses the issue of temperature sensitivity of Cu K_α imaging efficiency using a spherical Bragg reflecting crystal. The possibility of using this shifting as an independent temperature diagnostic is demonstrated.

In Chapter 4, the evidence of the formation of hot surface layers in laser-solid interactions is presented. The experimental data are supported by both spectroscopic modeling and PIC simulations.

Chapter 2

The Integrated Fast Ignition Experiment

The Integrated Fast Ignition experiment (IFIE) was conducted on the Vulcan laser at the Rutherford Appleton Laboratory with CD targets. These targets were spherical CD shells Cu doped for a probe to detect fast electrons through K_α emission. Six orthogonal beams delivering 0.9 kJ total energy in 1 ns drove the implosion, and at peak compression a 10 ps laser beam delivered 70 J to the target through a gold cone. We used a single hit CCD spectrometer and a time integrated K_α imager as diagnostics for the K_α fluorescence. Using the experimentally obtained absolute K_α yield and the extracted density profile, I developed a numerical model to estimate both the laser-to-electron conversion efficiency and the specific electron energy deposition by a divergent beam of hot electrons in the target. The model includes binary collisions

by the hot electrons, their energy loss in the potential induced by the forward current, and ohmic heating by the return currents driven by that potential.

The model shows that the conversion efficiency is about 17%, that the heating is bigger at the entry where the electron flux is higher and the density is lower, and that the electron flux at the rear side of the imploded core is reduced by an order of magnitude.

This chapter is structured as follows. A brief introduction to electron beam-based fast ignition (FI) is given in section (2.1). In section (2.2), the experimental setup is described including two diagnostics. Section (2.3) contains a summary of the experimental results of interest to this chapter. A detailed description of the numerical model is given in section (2.4), followed by a discussion of the modelled results in section (2.5).

2.1 Introduction

In the fast ignition approach to inertial confinement fusion the compression and ignition of the fuel are separated [11]. First, long-pulse high-intensity laser beams are used to compress the target to a density ~ 300 g/cm^3 [22, 23], then a separate short-pulse high-intensity laser beam is used to ignite it. The separation of the compression and ignition phases eliminates the need for timed shocks, but now the ignition task is deferred to the laser generated electrons. The coupling efficiency of laser energy to these electrons [24, 25], and their subsequent transport to the dense core where they

deposit their energy and ignite the fuel are the most important areas in fast ignition research today [26, 27, 28].

Early fast ignition related experiments were focused on the study of laser-generated electron transport in planar targets [29] [20] [30] [31] [32] [33] [34] and gas jets [35]. While these experiments answered many fundamental questions, ranging from laser absorption to electron transport and heating, they were conducted in conditions far from those envisaged for fast ignition. For example, they were conducted at densities less than or close to the solid densities, while fast ignition requires densities many orders of magnitude higher [36]. To our knowledge, only two independent so-called integrated fast ignition experiments were carried out: one in Japan with the GEKKO laser system [37, 38], the other, which is the subject of this chapter, with the Vulcan laser system [27, 39]. Since the original fast ignition scheme proposed by Tabak et al (1994) relies on laser hole boring to ignite the fuel, the coronal plasma created by the long pulse compression beams might inhibit the propagation of the igniter beam. As a solution, a cone inserted in the capsule was proposed as a guiding mechanism [40, 41, 42] by which the energy is deposited closer to the dense core and the under-dense plasma interference with the igniter pulse is eliminated by keeping a clear path.

The Japanese experiments carried out by Kodama et al. (2002) showed promising results for fast ignition. They observed an increase of 10^3 in the neutron yield from the thermonuclear DD-reaction and a 20% coupling efficiency to the core. These

results were achieved by compressing a polysterene CD shells to 50-100 g/cm^3 with a 2.5 kJ long pulse beam and heating it with a 300 J 0.6 ps laser pulse. In what follows, we report on similar integrated fast ignition studies, but with less energy in both long and short pulses. Another difference is that our experiments were conducted with a 10 ps igniter beam[1]. Our IFIE were undertaken in collaboration with other teams from the US as well as from the United Kingdom. The diagnostics were numerous and included a spherically bent Bragg imager, single hit CCD spectrometer [43], electron spectrometer, pinhole cameras, Ti radiography [44], proton imaging [45], etc. The experimental data used in this chapter were processed and analyzed by other members of the team. My contribution, in addition to some of the data acquisition, is the development and application of the numerical model mentioned earlier, using the experimentally obtained density profile and absolute K_α yield.

	RAL		**GEKKO**	
	Energy (J)	$\tau(ps)/\lambda(\mu m)$	Energy (J)	$\tau(ps)/\lambda(\mu m)$
Compression beam	0.9 kJ	1 ns / 1 μm	2.5 kJ	1.2 ns/ 0.532 μm
Igniter beam	70 J	10 ps / 1 μm	300 J	0.6 ps/ 1 μm

Table 2.1: RAL vs. GEKKO integrated fast ignition experimental parameters.

[1]for detailed comparison of experiment parameters refer to Table.2.1

2.2 Experimental setup

2.2.1 Vulcan laser system

Our integrated fast ignition experiments were conducted on the Vulcan laser at the Rutherford Appleton Laboratory in the United Kingdom. Vulcan is a Nd:glass laser operating at 1053 nm wavelength. It has the capability of delivering up to 2.6 kJ of energy in nanosecond pulses and 100 J in a picosecond [46]. In our experiments we used 6 orthogonal beams, each delivering up to 150 J of energy in a nanosecond pulse duration to compress the target. At the peak compression, a 70 J 10 ps laser pulse was used as an igniter beam via an inserted gold cone. The synchronization was jitter-free since both the igniter and the compression beams were derived from the same seed pulse.

2.2.2 Target description

The targets were made by General Atomics and consist of two main components: a spherical CD shell and a gold cone (Fig. 2.1). The spherical CD shell has a typical outer diameter of 500 μm and a thickness of 7 μm. The shell consisted of three layers: the inner layer was CD with a thickness of 1 μm; the middle layer was 30 or 70 nm of Cu; and the outer layer contained the remaining CD. A 950 μm long gold cone was inserted into the shell such that the distance from the tip of the cone to the center of the shell was 50 μm. The inner and outer full angles of the cone were 26° and

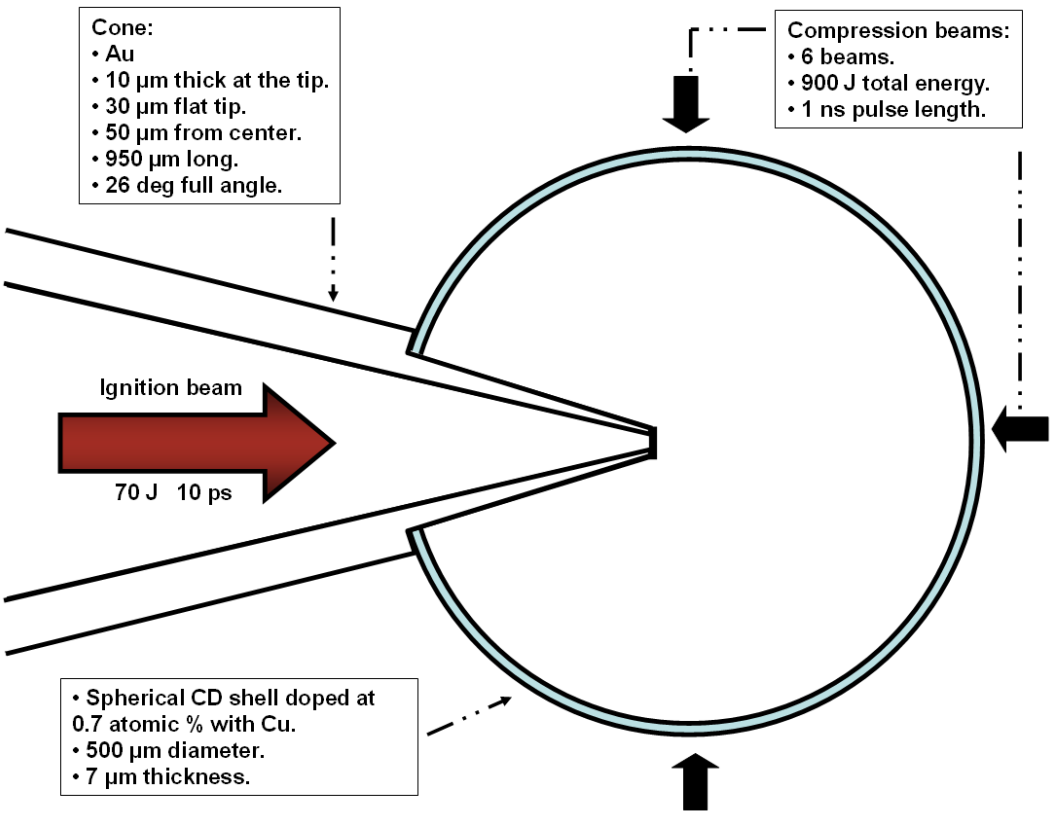

Figure 2.1: Schematics of spherical CD targets used in the integrated fast ignition experiment. The main components of the target are: the gold cone and the CD shell

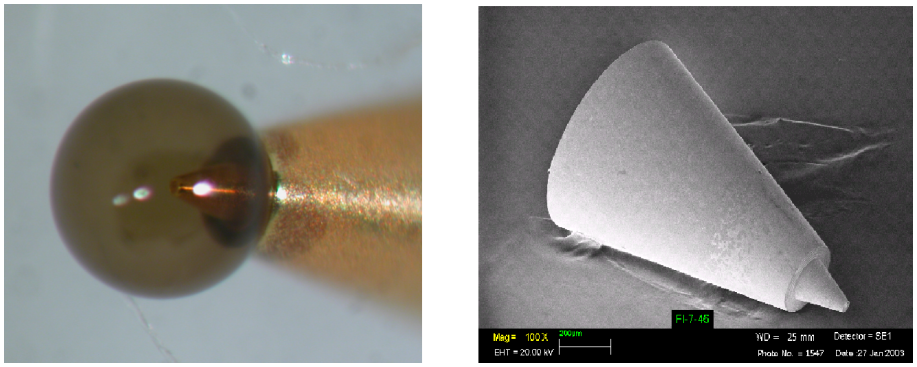

Figure 2.2: Pictures of the IFIE targets (courtesy of Richard Stephens from General Atomics): (a) A digital picture of the cone-shell assembly. (b) A scanning electron microscope image of the gold cone

34° respectively. The tip had a 30 μm lateral dimension and a thickness of 10 μm. A picture of the cone-shell assembly is shown in Figure 2.2-a, along with a scanning electron microscope (SEM) image of the Au cone.

2.2.3 Cu K_α Diagnostics

Two instruments were used as main diagnostics for the Cu K_α emission from the imploded target: a single hit CCD spectrometer and a spherically bent Bragg imager. These two instruments are described in detail in the next chapter and only a brief description is given here.

Single hit CCD spectrometer

The first instrument used to collect the generated x-rays was a single hit CCD spectrometer. It consists, primarily, of a charge-coupled device (CCD) operating in the single-photon counting regime. The condition of single-photon counting is satisfied when the flux of incoming radiation is low that the probability of two or more photons hitting the surface of the same pixel is negligible. This device has the ability to directly detect photons without the use of any optical elements. We used a back-illuminated CCD camera with 2048 x 2048 array and 13.5 μm pixel size [47].

Spherically bent Bragg imager

The second instrument is a monochromatic K_α imager, which consists of a spherically bent Bragg crystal coupled to a charge-coupled device (CCD). The crystal had a 38 cm radius of curvature and 3.082 $\mathring{A}$ 2d lattice spacing. When used in second diffraction order at a wavelength of 1.54 nm , monochromatic 2D spatially resolved Cu K_α images of the target are obtained. The K_α photons were collected with a Princeton Instruments CCD camera, cooled to -30 ° Celsius. The model used was TEK1024 $\times$ 1024DBT3 with 1024 $\times$ 1024 imaging array, 25 μm pixel size, and 16-bit recording resolution. A 25 μm Cu filter was located in front of the CCD to narrow the bandwidth of the radiation reaching the detector by reducing the number of photons with energies above the Cu K-Shell photoabsorption edge.

2.3 Experimental Data

2.3.1 Density of the imploded core

The densities of the imploded core at different phases of implosion were determined using a radiography technique. An 80 J 800 fs laser pulse interacting with a 25 μm thick Titanium foil created a burst of x-rays. A narrow band of x-rays centered at Ti K_α line was selected with a spherically bent Bragg crystal and used as a back-lighter source of radiation. Two-dimensional spatially resolved images are then obtained using a CCD to detect Ti K_α photons escaping from the target. By varying the

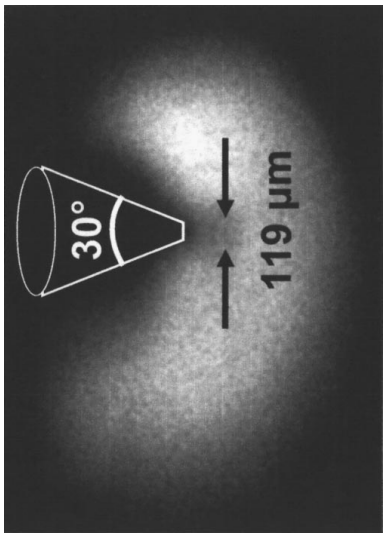

Figure 2.3: Monochromatic Ti K_α radiograph of an imploded target at 3.25 ns showing a 119 μm full width at half maximum at stagnation

delay between the compression beams and the beam creating the back-lighter source, snapshots of the target are obtained as it implodes. Such an image is shown in Fig. 2.3 in which a lineout through the middle showed a 119 μm full width at half maximum. It was also found that stagnation occurs at 3.25 ns after the compression has started [44].

The density profile of the imploded core was extracted from this image by the Abel inversion method. Such a density profile along with a gaussian fit are shown in Fig. 2.4. For more details on the radiography technique, source characterization, and data analysis the reader is refereed to James King's PhD dissertation [48].

In order to descretize the density on an equal spacing spatial grid, an analytical expression was used. It was obtained by fitting the experimental densities to a gaussian profile of the form,

$$\rho(r) = \frac{C}{\sigma\sqrt{2\pi}} \exp -\frac{(r)^2}{2\sigma^2} \tag{2.1}$$

where $C = 38$ and $\sigma = 15$.

The total mass of the modelled core is given by the following integral:

$$m = \int \rho(r)\ 4\ \pi\ r^2\ dr = \frac{C}{\sigma\sqrt{2\pi}} \int \exp -\frac{(r)^2}{2\sigma^2}\ 4\ \pi\ r^2\ dr = 2.057 \cdot 10^{-4} mg \tag{2.2}$$

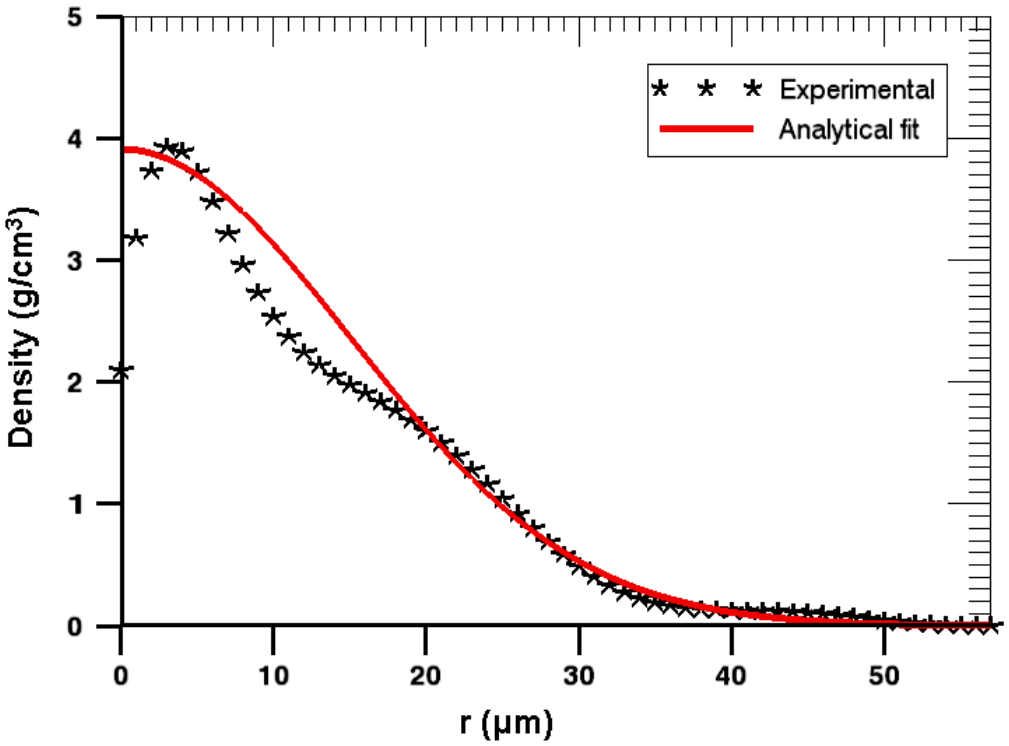

Figure 2.4: Density of the imploded core. Stars, the experimentally extracted densities as a function of the radial distance. Red solid line, the gaussian fit to the experimental data.

2.3.2 Absolute yield of Cu K_α

X-ray spectra similar to the one in Fig. 2.5-a were extracted by taking histograms or pulse-height distributions of the pixel values of the single-hit CCD spectrometer data. These spectra were then flattened by subtracting the background (Fig. 2.5-b) and used to determine the absolute number of K_α photons. This was done by summing the number of hits contained in the K_α-line shape and taking into account the solid angle, filter transmission, and quantum efficiency of the CCD in single-pixel analysis mode [47]. Within the low level of Cu K-shell emission pixel exposure, the

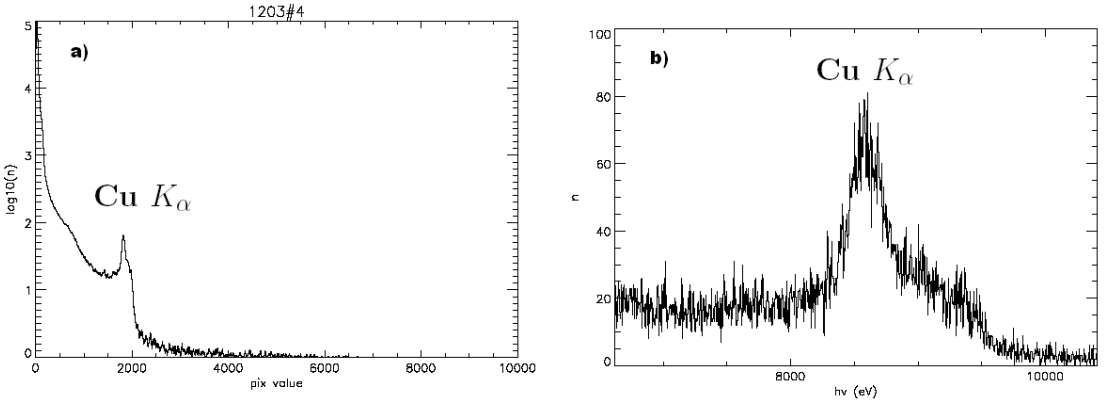

Figure 2.5: Typical single hit CCD spectrometer data. (a) The histograms or pulse-height distributions of the pixel values of the single-hit CCD spectrometer data. (b) The background-adjusted histogram- the absolute yield is obtained by summing the values under the Cu K_α-line shape

CCD is operating in a single-photon counting mode. The relative error bars are estimated to be $\sim$ 40% based on the standard deviation of several measurements at the same experimental condition. The absolute uncertainty is estimated to be a factor of 2.4 based on an estimated uncertainty in the CCD quantum efficiency for

single-pixel analysis [49] and the relative measurement error. Under the assumption that the emission is isotropic into a 4π steradian solid angle, the maximum absolute yield obtained for imploded targets was $1.1 \cdot 10^{11}$ ph/sr.

2.4 Numerical Model

In order to estimate the laser-to-electron coupling efficiency and the associated isochoric heating of the imploded targets, a numerical transport model was developed. The starting point of this model is the laser pulse itself. Most PIC and Hybrid-PIC codes either directly inject electrons into the target or use ideal gaussian profiles to simulate laser-plasma interactions. In real experiments the laser pulse is anything but a nice guassian. Fig. 2.6-a shows a 16-bit equivalent plane image of the focal spot. A horizontal lineout revealed that this pulse is gaussian-like in a small region around the peak with a FWHM $\sim$ 8 μm, followed by two secondary maxima and finally by broad wings (Fig. 2.6-b).

In the vertical direction the focal spot is wider, approximately 11 μm FWHM in the central spot (Fig. 2.7-a) which contains about 30% of the energy (2.7-b). The focal spot exhibits filament-like structures with 65% of the energy (region bounded by the oval).

Due to spontaneous stimulated emission (ASE), the main pulse is preceded, a few nanoseconds before the interaction, by a prepulse in the form of a pedestal. Modern day laser systems can reach intensities well above 10^{21} W/cm^2 and the prepulse can

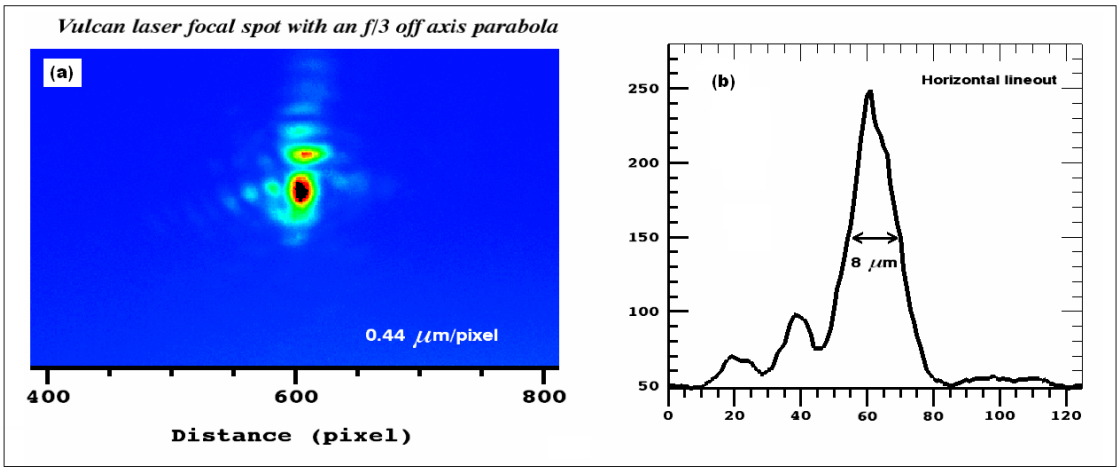

Figure 2.6: Vulcan laser focal spot. (a) 16-bit equivalent plane image of the focal spot. (b) A horizontal lineout through the middle of the central spot

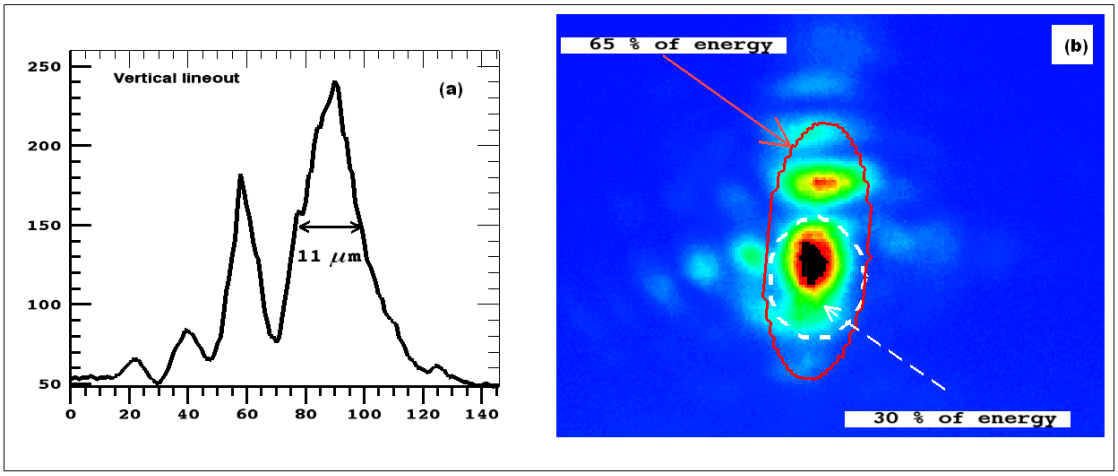

Figure 2.7: Vulcan laser focal spot. (a) A vertical lineout through the middle of the central spot. (b) 16-bit equivalent plane image of the focal spot.

be as high as 10^{15} W/cm^2. At these intensities the material of the target starts to ionize [50] and a low density coronal plasma is formed. The main pulse, lagging a few nanoseconds behind, interacts with this low density region first. As a result,

the propagation of the laser light is altered. For example, Bastiani et al. (1997) observed a weakening and angular broadening of a laser-generated electron beam in the presence of preformed plasmas of different scale lengths ($[1/n_e][dn_e/dx]^{-1}$).

I used the following experimentally based double gaussian profile to model the igniter beam:

$$I_{Laser}(r,t) = \underbrace{\exp\left[-\left(\frac{t-t_p}{\tau}\right)^2\right]}_{Temporal\ laser\ profile} \times \underbrace{\left\{ I_1 \exp\left[-\left(\frac{r}{R_1}\right)^2\right] + I_2 \exp\left[-\left(\frac{r}{R_2}\right)^2\right]\right\}}_{Spatial\ laser\ profile} \tag{2.3}$$

where $R_1 = 5\ \mu m$, $R_2 = 40\ \mu m$, $I_1 = 4\times10^{18}\ W/cm^2$, $I_2 = 1\times10^{17}\ W/cm^2$, $t_p = 5\ ps$, and $\tau = 2.5\ ps$.

The spatial profile in eq. (2.3) was obtained as a best fit to the experimental data in (Fig. 2.8-b). The temporal profile, 10 ps long, is taken to be a nice gaussian since the prepulse level was as low as $10^{11}\ W/cm^2$.

The laser light can only penetrate up to the critical surface, defined as the surface where the laser frequency is equal to the plasma frequency. This surface is usually characterized by its density known as the critical density, $n_{cr} = (\frac{m\epsilon\omega^2}{e^2})$, where ω is

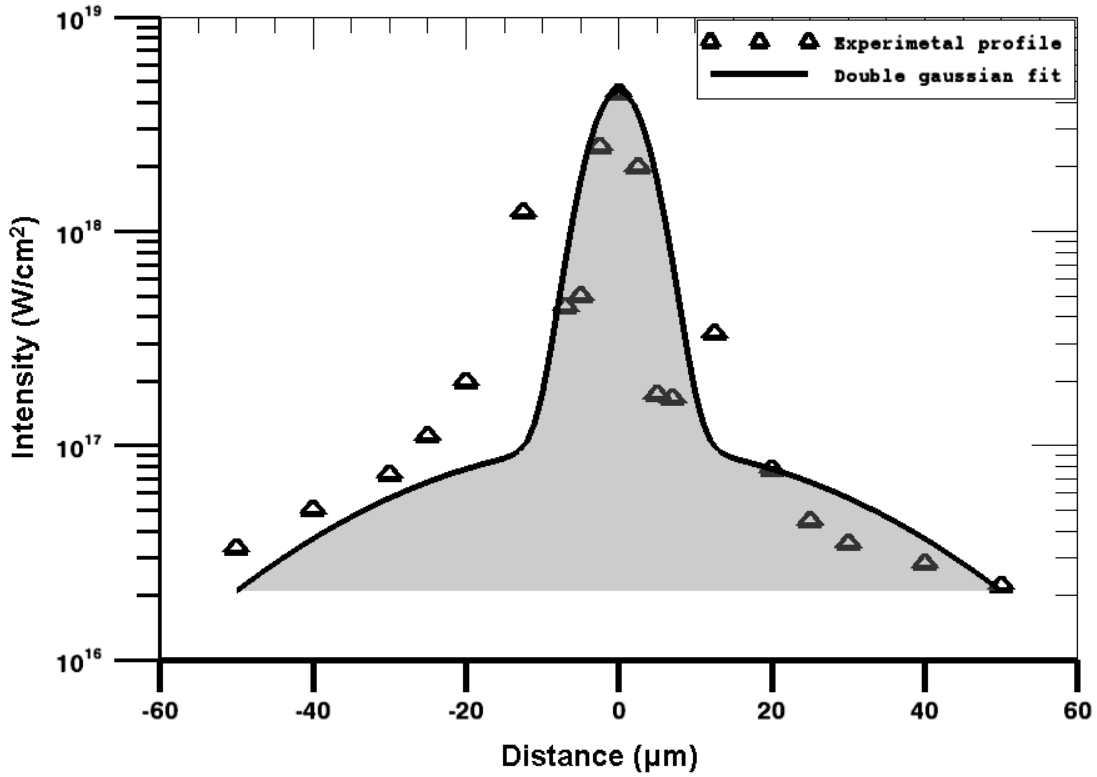

Figure 2.8: The vulcan laser profile. Triangles, the experimental laser profile obtained by taking a horizontal lineout through the middle of the 16-bit of the image in Fig. 2.6-a. Solid line, a double gaussian fit the experimental profile

the laser frequency and ϵ_0 is the permittivity of free space. In ultrashort ultra-intense laser-plasma interactions, electrons with energies comparable to or larger than the rest energy $m_e c^2$ are generated. The relativistic effects become important and a correction factor, γ, must be applied to the critical density, where γ is the Lorentz factor. As a result, the critical density is pushed inward toward higher densities and the laser pulse penetrates farther. For 1 μm laser light, the critical density is about $1.1 \cdot 10^{21}\ cm^{-3}$, but at our intensity of $4 \times 10^{18}\ W/cm^2$ the average energy of the hots

is of the order of 500 keV (see eq. (2.8)). Using the Lorentz factor which is ~ 2 for 500 keV electrons, the relativistic critical density is $2.1 \cdot 10^{21}\ cm^{-3}$.

In our calculations we assumed that the main pulse interacts directly with the imploded CD core and any interaction in the gold material of the cone is neglected. Since the imploded CD core had an initial temperature of 75 eV and an average charge state $\overline{Z} = +4$ [27], the electron density at this surface is $n_e|_{z=0} = (\overline{Z} \times n_i|_{z=0}) = 7 \times 10^{21}\ cm^{-3}$. So the hot electrons began their interaction in an overdense plasma starting at a density of $\sim 3n_{cr}$ and increasing up to $270n_{cr}$ at the center of the target.

The numerical model is implemented in cylindrical geometry with coordinates r, θ, and z (Fig. 2.9). A further simplification is made by eliminating the variable θ and working in concentric cylindrical zones of equal radii. Although this approach ignores electron scattering, it accounts for electron resistive inhibition [51, 52].

At time t_0, relativistic electrons are created at the front surface of the target ($z = 0$) in annular zones of surface $S_0(r) = 2\pi\ r\ dr$. Their local total energy is determined by the laser-to-electron conversion efficiency and the surface of the annulus where they reside,

$$E_{hots}(r,t) = \eta_{Laser}\ E_{Laser} \left[\frac{I_{Laser}(r,t)}{I_{peak}(t)}\right] \left[\frac{S_0(r)}{S_{focal}}\right] \tag{2.4}$$

where S_{focal} is the focal spot size.

These laser-generated relativistic electrons are then given a local temperature, derived

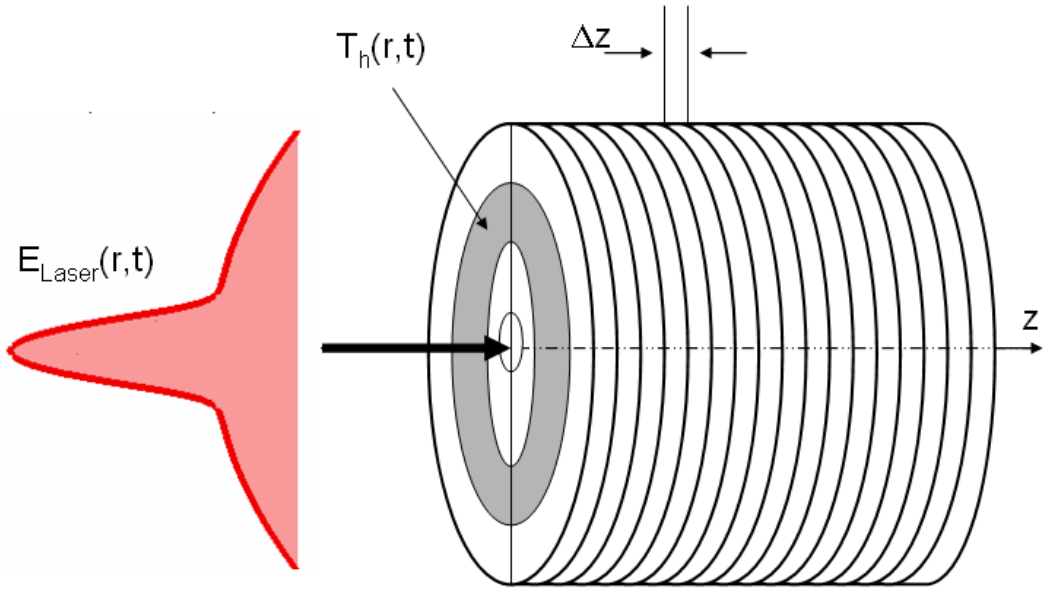

Figure 2.9: Problem geometry: z-axis, laser and electron propagation direction. radius r, radius of concentric zones

from laser intensity, according to the ponderomotive scaling law [53]:

$$T_h(r,t) = 511 \times \left\{ \sqrt{\left(1 + \frac{I_{Laser}(r,t)\ \lambda^2}{2.8 \cdot 10^{18}\ W/cm^2}\right)} - 1 \right\} keV \tag{2.5}$$

If these hot electrons have a local Maxwllian distribution in energies,

$$f(E,r,t) \propto \frac{\sqrt{E}}{T_h(r,t))^{3/2}} \times \exp\left[-\frac{E}{T_h(r,t)}\right], \tag{2.6}$$

then the quantity $N_h(r,t)\ f(E,r,t)\ dE$ gives the number of electrons in the annulus with energies in the interval $[E, E+dE]$, where $N_h(r,t) = E_{hots}(r,t)/\frac{3}{2} \times T_h(r,t)$ is their total number in that annulus. Knowing their total number and energy distribution, these electrons are followed through cylindrical zones of length Δz and volume $V(r,z) = S(r,z) \times \Delta z$, where $S(r,z) = 2\pi r(z)dr$ is the cross-sectional area of the

Time	$t_i = i\ \Delta t$	$\Delta t = 1ps$	$i = 1, 2..imax$
Energy	$E_j = j\ \Delta E$	$\Delta j = 10 - 100keV$	$j = 1, 2..jmax$
z-direction	$z_k = k\ \Delta z$	$\Delta z = 1\mu m$	$k = 1, 2..kmax$
r-direction	$r_l = l\ \Delta z$	$\Delta r = 1\mu m$	$l = 1, 2..lmax$

Table 2.2: Numerical model grids.

beam at depth z [2]. The dependence of the radial distance r on the propagation direction z is introduced to account for the divergence of the beam [33]. This dependence is given by the following expression:

$$r(z + \Delta z) = r(z) + \Delta z\ \tan(\theta),\ \theta = 20^\circ \tag{2.7}$$

As they traverse the target, the hot electrons lose energy due to collisions and radiation. They are also slowed down by the electric field induced by the charge separation. Several tallys are kept in memory as a function of the depth, z. These include the collisional energy loss, potential, and return currents to mention few. All the equations and mathematical expressions are descretized on four grids: one temporal, two spatial, and one for energy (see Table.2.2). Grid step-sizes are specified at the beginning of the calculation depending on the desired accuracy and CPU time.

[2] with the exception of the central zone all the cross-sectional areas have annular shapes

2.4.1 The collisional heating

The energy of an electron at the grid point $z + \Delta z$ is calculated from its energy at the previous grid point z by,

$$E(z+\Delta z) = E(z) - \int_z^{z+\Delta z} \underbrace{\left(\frac{dE}{dz}\right)_c}_{collisional} dz - \int_z^{z+\Delta z} \underbrace{\left(\frac{dE}{dz}\right)_r}_{radiative} dz \; - e \underbrace{\phi(z)}_{potential} \tag{2.8}$$

where $\left(\frac{dE}{dz}\right)_c$,$\left(\frac{dE}{dz}\right)_r$, $\phi(z)$ are the collisional stopping power, the radiative stopping power, and the electric potential due to charge separation respectively. The energy of the electrons is updated using all three terms in equation (2.8), but only the second term is needed to evaluate the collisional heating. The following expression from reference [54] was used for the collisional stopping power,

$$\left(\frac{dE}{dz}\right)_c = \frac{4\pi r_0^2 mc^2 nZ}{\beta^2}\left\{\ln\left(\frac{\beta\gamma\sqrt{\gamma-1}}{I}mc^2\right)\right\} +$$

$$+ \frac{4\pi r_0^2 mc^2 nZ}{\beta^2}\left\{\frac{1}{2\gamma^2}\left[\frac{(\gamma-1)^2}{8} + 1 - (\gamma^2+2\gamma-1)\ln 2\right]\right\} \tag{2.9}$$

The dependence of eq. (2.9) on the grid parameter z is embedded in the density, $n(z)$, of the imploded target.

For the radiative collisional power we used the following approximate expression [54],

$$\left(\frac{dE}{dz}\right)_r = \frac{ZE(MeV)}{750}\left(\frac{dE}{dz}\right)_c \tag{2.10}$$

where $\left(\frac{dE}{dz}\right)_c$ is the collisional stopping power from eq. (2.8). The total stopping power is therefore,

$$\left(\frac{dE}{dz}\right)_{Total} = \left[1 + \frac{ZE(MeV)}{750}\right]\left(\frac{dE}{dz}\right)_c \tag{2.11}$$

To optimize memory and CPU time it was sufficient to calculate and store $\left(\frac{dE}{dz}\right)_c$ and use eq. (2.11) for the total stopping power. In our experiment, the Bremsstrahlung emission was negligible due to the low Z of the target.

2.4.2 The Ohmic heating

An electron beam propagating in a conductor is susceptible to the action of self-generated magnetic fields. The higher the current the higher the magnetic field. The upper limit is reached when this azimuthal magnetic field is sufficient to stop the current from going forward and reverse the trajectories of the electrons. It is known as the Alfven limit and its value can be estimated by, [13],

$$I_A \simeq \beta\ \gamma\ m\ c^3/e \tag{2.12}$$

In plasmas the background electrons redistribute themselves in such a way that return currents are created. In our model the return current density is determined from the forward current density by the following expression,

$$\overrightarrow{j}_{return}(r,z,t) \approx -\overrightarrow{j}_{hots}(r,z,t) = e\int\ c\ \beta(E)\ n_h(r,z,t,E)\ dE\ \frac{\overrightarrow{z}}{\|\overrightarrow{z}\|} \tag{2.13}$$

where $n_h(r,z,t,E)\ dE$ is the number of hot electrons per unit volume with energies between E and $E + dE$ in a zone with given radius r and depth z at time t.

When this return current traverses the target, heat is dissipated due to the target resistance. The rate of heat dissipation per unit volume is proportional to $\overrightarrow{j_r}^2$. The proportionality factor which is temperature-dependent is the plasma resistivity. It is approximated by its maximum value of 3 $10^{-7}(\Omega$ m) at the plateau (see Fig. 1.5) if $T(r,z,t) < 100$ eV, above 100 eV the classical Spitzer resistivity is used [55],

$$\eta = 5.2 \times 10^{-5} \frac{Z \ln \Lambda}{T^{3/2}(eV)} \ (\Omega \ m) \tag{2.14}$$

2.4.3 Temperature of the imploded core as a function of depth

The temperature of the target as a function of depth is determined from collisional and ohmic heating by,

$$T(z) = A[\epsilon_{coll}(z) + \epsilon_{Ohmic}(z)] + B[\epsilon_{coll}(z) + \epsilon_{Ohmic}(z)]^{1.5} + C[\epsilon_{coll}(z) + \epsilon_{Ohmic}(z)]^{1.8} \tag{2.15}$$

where $\epsilon_{coll}(z)$ and $\epsilon_{Ohmic}(z)$ are the amounts of energy per unit of mass of CD deposited by collisions and return currents respectively. The constants A, B, and C were obtained as best fit to LANL SESAME equation of state tables provided by Steve Hatchett from LLNL.

$$A = 48.915 \qquad B = -33.424 \qquad C = 11.602$$

2.4.4 K-Shell electron impact ionization cross section

In order to use the absolute K_α yield as a measure of the isochoric heating, a K_α module was implemented. it runs in parallel with the transport module. in other words the number of Cu K_α photons induced by the hot electrons at a grid point z is calculated and stored as they move to the next grid point $z + \Delta z$. The expression used is of the form,

$$N_{ph}(r, z, t) = \int n_{Cu}(z)\ \Delta z\ \sigma(E)\ N_h(r, z, t, E)\ dE \tag{2.16}$$

where $N_h(r, z, t, E)\ dE$ is the number of hot electrons with energies between E and $E + dE$ in the zone, $n_{Cu}(z)$ is the copper number density, and $\sigma(E)$ is the electron impact ionization cross section in Cu. For the cross section we used the following formula from Deutsch-Mark's work [56],

$$\sigma(E) = 2\pi\ r_{1s}^2\ g_{1s}\ \Phi_{DM}(E)\ \Psi_{DM}(E)\ \Omega_{DM}(E) \tag{2.17}$$

where r_{1s} is the radius of maximum radial density of Cu 1s-shell from the tables of Desclaux [57], g_{1s} is a weighting factor, E_{1s} is the binding energy of 1s electrons, and the functions Φ_{DM}, Ψ_{DM}, Ω_{DM} are given by Eqs. (2.18-2.21),

$$\Phi_{DM}(U) = d\ \left(\frac{1}{U}\right)\left[\frac{(U-1)}{(U+1)}\right]^a\ \{b + c\ [1 - (2U)^{-1}]\ \ln\ [2.7 + \sqrt{(U-1)}\ ]\} \tag{2.18}$$

$$\Psi_{DM}(U)) = \left[1 + 2\ \frac{U^{1/4}}{J^2}\right] \tag{2.19}$$

$$\Omega_{DM}(U)) = \frac{(1+2J)}{(U+2J)} \left[\frac{(U+J)}{(1+J)^2}\right] \left\{\frac{[(1+U)(U+2J)(1+J)^2]}{[J^2(1+2J)+U(U+2J)(1+J^2)]}\right\}^{3/2} \quad (2.20)$$

$$U = E/E_{1s},\ a = 1.06,\ b = 0.23,\ c = 1.00,\ d = 1.1,\ and\ J = m_e c^2/E_{1s}. \quad (2.21)$$

2.5 Results and Discussion

Having described in detail the numerical model in previous section, we are ready to apply it to our integrated fast ignition experiment. But before we embark on this task, let us briefly summarize the experimental results that are used in our study:

- *The laser profile is based on the experimental laser pulse.*
- *The density profile is a gaussian fit to the experimental data obtained from radiography.*
- *The beam divergence is from previous experiments with flat targets from the work of Stephens et al (ref. [33])*
- *The maximum absolute K_α yield is 1.1×10^{11} photons/sr recorded by the single hit CCD spectrometer.*

The input parameters for the code are the total laser energy on target, E_{Laser} and laser-to-electron conversion efficiency, $\eta_{Laser} = E_{Laser}/E_{hots}$, where E_{hots} is the total

energy in the hot electrons. A set of computations are carried out by fixing E_{Laser} to the experimental value of 70 J and varying η_{Laser} from 2% to 80%. The absolute K_α yield is then calculated by integrating eq. 2.18 over the spatial and time variables (r,z,t) and taking into account the attenuation of Cu K_α emission in the material of the target before it reaches the detector. This calculated yield is plotted in Fig. 2.10 as a function of the conversion efficiency. At 2% conversion efficiency, a minimum yield of 1.26×10^{10} ph/sr is obtained. The calculated yield increases monotonically with increasing conversion efficiency and the maximum value of 5×10^{11} ph/sr is reached at $\eta_{Laser} = 80\%$. The maximum absolute yield obtained by the single hit CCD spectrometer was 1.1×10^{11} ph/sr. comparing this value to the calculated one yields a 17% conversion efficiency as indicated by the intersection of the curve and the dashed lines in Fig. 2.10. This laser to electrons conversion efficiency is in a good agreement with the value of 15% reported by Key et. al [27].

Using the conversion efficiency obtained above, a series of calculations were carried out to study the electron transport and the associated isochoric heating. The hot electrons are injected in a pre-compressed Cu-doped spherical CD fuel with a density profile given by Eq. (2.2). Their total energy is determined according to,

$$E_{Laser} \times \eta_{Laser} = 70J \times 17\% = 12J,$$

their intensity depends on the injection area which we assume to be 30 μm, the same size as the tip of the cone (K_α spot sizes many times bigger than the laser focal spot have been observed in flat targets, spot $\sim$ 70 μm [33]).

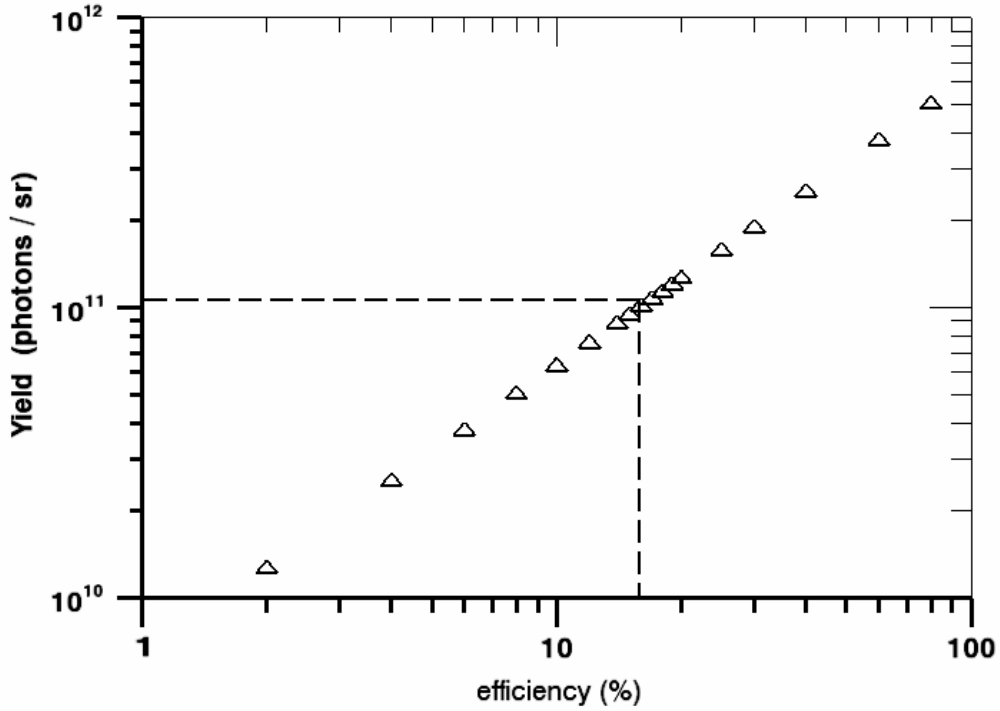

Figure 2.10: K_α yield vs. Coupling efficiency: Triangles, the modelled yield (ph/sr). Intersection of dashed horizontal and vertical lines, the maximum experimental K_α yield (ph/sr) obtained with the single hit CCD spectrometer.

Fig. 2.11 shows the hot electron distribution at three different locations in the target. The distribution $f_1(E)$ (solid black line) is the distribution at the entry surface in the plane $z = 0\ \mu m$, $f_2(E)$ (dashed blue line) is taken at a depth of $z = 20\ \mu m$, and finally $f_3(E)$ (dashed red line) is the distribution at the rear surface of the target which is at $z = 100\ \mu m$. Three important conclusions can be drawn from Fig. 2.11. First, there is a cut-off energy for each distribution. for example $f_2(E)$ has a cut-off energy of 12 keV indicating that electrons with energies $E \leq 12\ keV$ completely lose their energy in the first 20 microns due to collisions, radiation, and Ohmic potential.

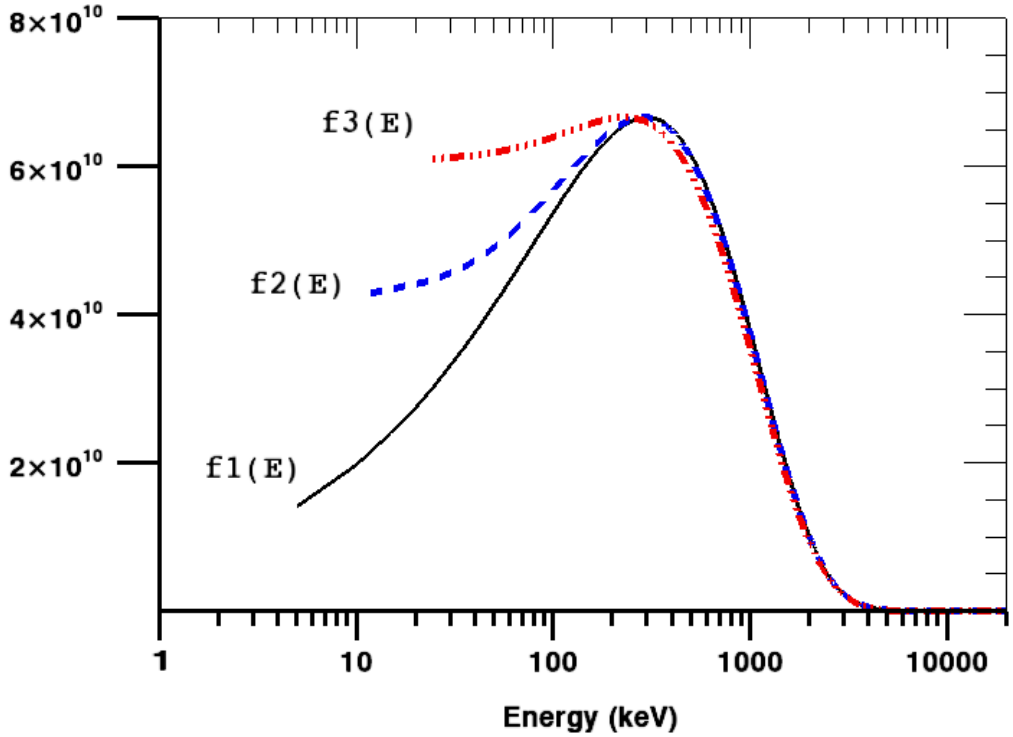

Figure 2.11: The hot electron distribution: solid black line ($f1(E)$), the distribution at the entry surface in the plane z=0 μm. dashed blue line ($f2(E)$), the distribution at the plane z=20 μm. dashed red line ($f3(E)$), the distribution at rear surface of the target which is at the plane z=100 μm.

By looking at cut-off energies at different depths the range of electrons in these experimental conditions can be inferred. Second, the energy corresponding to the peak of the distribution is shifting, though slowly, toward lower energies. Finally, the distribution deviates from the initial Maxwlellian as you move deep into the target.

The hot electron flux distributions were also obtained as functions of the depth into the target. These distributions are plotted in Fig. 2.12 for the depths mentioned earlier . The hot electron flux is distributed at the entry surface around an energy

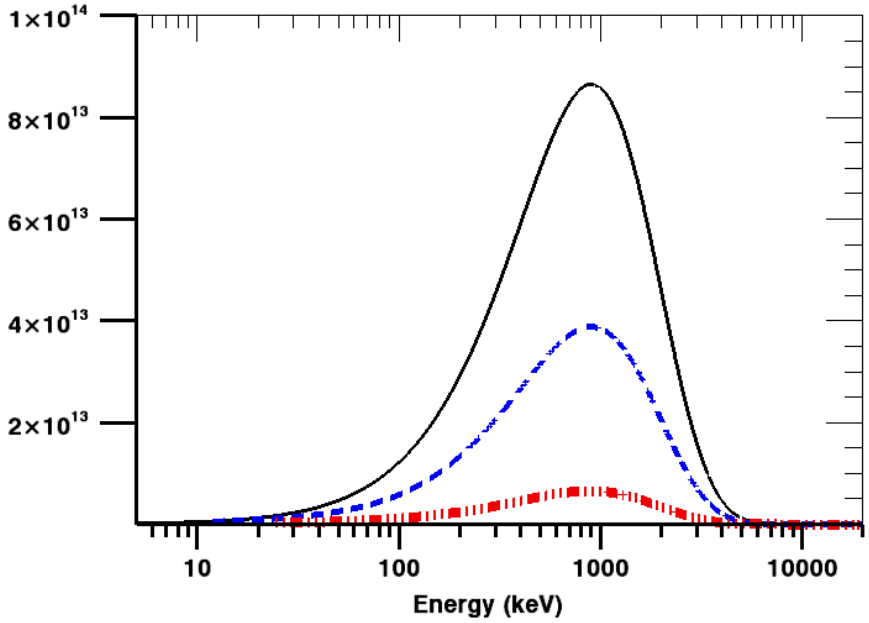

Figure 2.12: The hot electron flux distribution: solid black line, the flux distribution at the entry surface in the plane z=0 μm. dashed blue line, the flux distribution at the plane z=20 μm. dashed red line, the flux distribution at rear surface of the target which is at the plane z=100 μm.

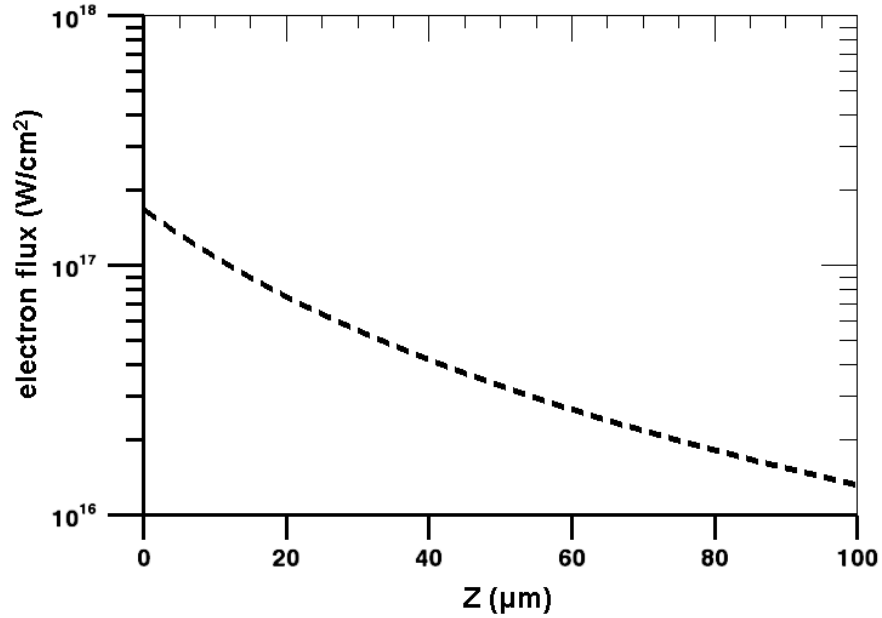

Figure 2.13: Hot electron flux as a function of the depth into the imploded core

$E_{peak} = 900\ keV$ with a full width at half maximum of $\Delta E = 1775\ keV$. With increasing depth z, the distribution is shifted toward higher energies. The peak of the distribution at the rear surface is located at 975 keV while the FWHM is increased by almost 20 keV. An integration of this distribution over energies gives the electron flux as a function of the depth into the imploded core. (Fig. 2.13).

The temperature of the isochorically heated target with and without the ohmic heating is plotted in Fig. 2.14. When the resistivity is turned on, the target reaches a maximum temperature of 155 eV as shown by the dashed line. The depth-dependent temperature of the imploded core decreases in a fashion similar to that of the electron flux (Fig. 2.13). The temperature is highest at the entry surface where the electron flux has its highest value of $1.68 \times 10^{17}\ W/cm^2$. The potential opposing the motion of the hot electrons is small compared to their mean energy and has a modest effect (solid line with squares). A plot of the temperature with the resistivity turned off shows that Ohmic heating contribution is higher at the entry surface and very small if not negligible beyond depth of 20 μm which is again consistent with the electron flux argument. The energy deposited in the target was about 0.96 J which corresponds to about 8% of the hot electron energy.

The results above were obtained using the classical expression for the stopping power in cold matter. But the imploded core has an initial temperature as a result of the compression by the long pulse beams. Taking an initial temperature of 75 eV and an average ionic charge $\overline{Z} = +4$ as explained in ref. [27], similar calculations

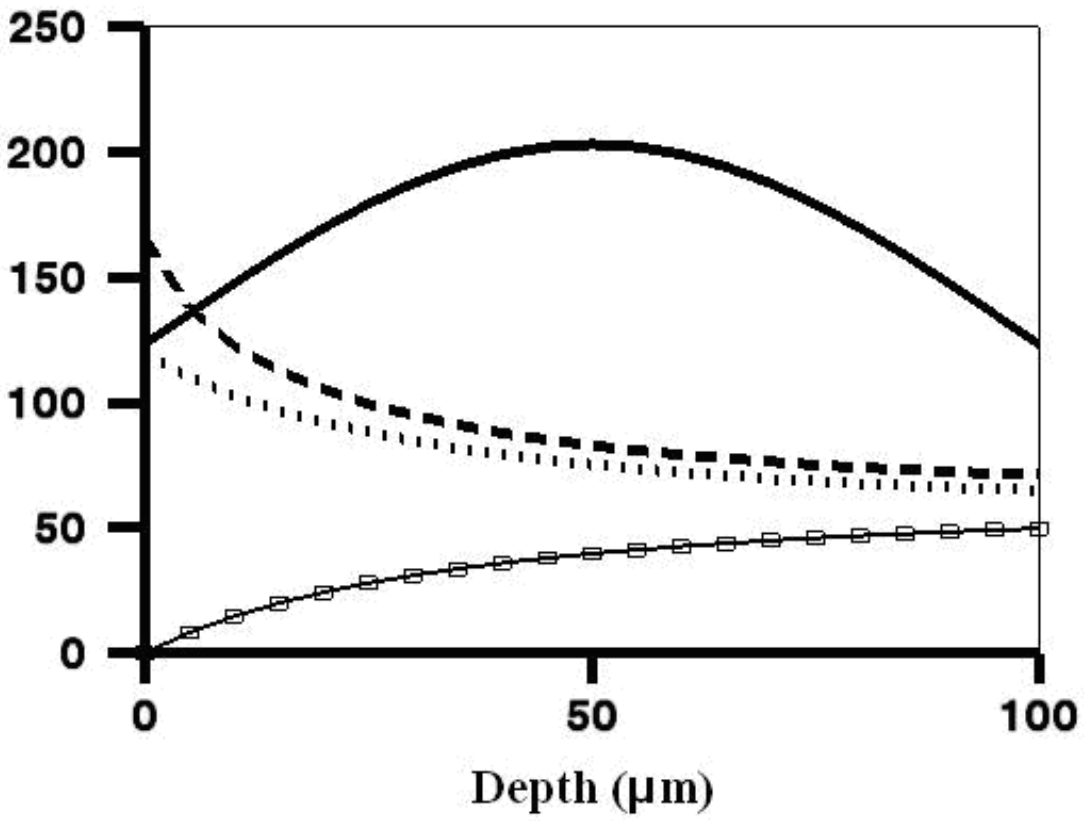

Figure 2.14: Heating model: solid line, density (x50) g/cm^3, line with squares, Ohmic potential (x5) keV, dashed line, temperature in eV. dotted line, temperature with no ohmic heating in eV.

were carried out with an analytical expression for electron stopping in hot plasmas.

We used the following expression from the work of Li and Petrasso [58, 59]:

$$\frac{dE}{ds} = -\frac{2\pi r_0^2 mc^2 n_i Z}{\beta^2} \times \left[\ln \left[\frac{(\gamma-1)\lambda_D}{2\sqrt{2\gamma} r_0} \right]^2 + 1 + \frac{1}{8} \left(\frac{\gamma-1}{\gamma} \right)^2 - \left(\frac{2\gamma-1}{\gamma} \right) \ln 2 \right] -$$

$$- \frac{2\pi r_0^2 mc^2 n_i Z}{\beta^2} \times \ln \left(\frac{1.123\beta}{\sqrt{2kT_h/mc^2}} \right)^2 \tag{2.22}$$

The use of expression (2.22) instead of expression (2.9) did not have any significant effects on the results. Both electron and electron flux distributions followed the same trend as before. The maximum temperature increased by 11 eV, from 155 eV to 166 eV, due to an increase in the fraction of energy deposited from 8% to 9%.

At the beginning of this chapter we mentioned that two instruments were used as diagnostics for the Cu K_α emission. In our modeling, only the absolute yield, obtained with the single hit CCD spectrometer, was used. The K_α imager was affected by the fact that the compressed core was pre-heated to temperatures where the shifting of line emission becomes an issue. This temperature-dependent behavior is addressed in details in the next chapter.

Chapter 3

Temperature sensitivity of Cu K_α imaging efficiency using a spherical Bragg reflecting crystal

The Vulcan laser facility at the Rutherford Appleton Laboratory was used to study the interaction of a 75 J 10 ps, high intensity laser beam with low-mass, solid Cu targets. Two instruments were fielded as diagnostics of the Cu K-shell emission from the targets: A single photon counting CCD spectrometer provided the absolute K_α yield and a spherically bent Bragg crystal recorded 2D monochromatic images with a spatial resolution of 10 μm. Due to the shifting and broadening of the K_α spectral lines with increasing temperature, there is a temperature dependence of the crystal collection efficiency. This provides a temperature diagnostic when cross calibrated against a

single hit CCD spectrometer, and it affects measurements of the spatial pattern of electron transport. The experimental data showing changing collection efficiency are presented. The results are discussed in light of modeling of the temperature-dependent spectrum of Cu K-shell emission.

3.1 Introduction

The advent of short-pulse laser technology has made it possible to create and explore isochorically heated high energy density matter. With this comes the need for diagnostics to unravel the fundamental physics of these transient plasmas. As plasma diagnostics, spherically bent Bragg crystals have been used in a back-lighter configuration to study the dynamics of laser imploded targets [60], wire-array Z-pinch implosions [61], and ablative Richtmyer-Meshkov instability [62]. They have been used also as diagnostics in the context of fast ignition [11] to get insight into short-pulse, high-energy laser generated electron transport and the associated isochoric heating of the targets [63]. For example, Stephens et al. [33] used a spherically bent Bragg crystal coupled with a CCD to obtain monochromatic spatially resolved 2D images of planar targets with buried Ti or Cu fluor layers. Due to the shifting and broadening of the K_α emission line with temperature [64], care must be taken in interpreting the results, especially when dealing with low mass targets and high laser energies which produce high temperatures.

In this chapter, we describe a temperature-dependent K_α diagnostic, present the

experimental evidence of changing collection efficiency, and discuss it in light of modeling of the temperature dependent Cu K-shell emission.

3.2 Experimental setup

The short-pulse, high intensity beam of Vulcan laser facility at the Rutherford Appleton Laboratory was used to irradiate planar solid Cu foils. This infrared (1.053 μm) laser pulse was generated using the Chirped Pulse Amplification (CPA) technique [65] and contained 75 J of energy delivered in 10 ps. A peak intensity of $\sim 5 \times 10^{18}\ W/cm^2$ was achieved by using an f/3 off-axis parabola to focus the beam to a 10 μm focal spot. About 50% of the laser energy on target was contained in the central spot, the remaining energy is distributed over the wings. The spontaneous stimulated emission (ASE) contrast ratio was 10^{-7} in intensity and 10^{-4} in energy.

The targets were planar solid Cu foils of 100 $\mu m \times 100\ \mu m$ and 500 $\mu m \times 500\ \mu m$ lateral dimensions and of varying thicknesses (1 μm to 30 μm). Fig. 3.1 shows a 68 eV XUV image of a 500 $\mu m \times 500\ \mu m$ 30 μm thick target. The big plasma plume is created at the front surface where the laser impinges on the target.

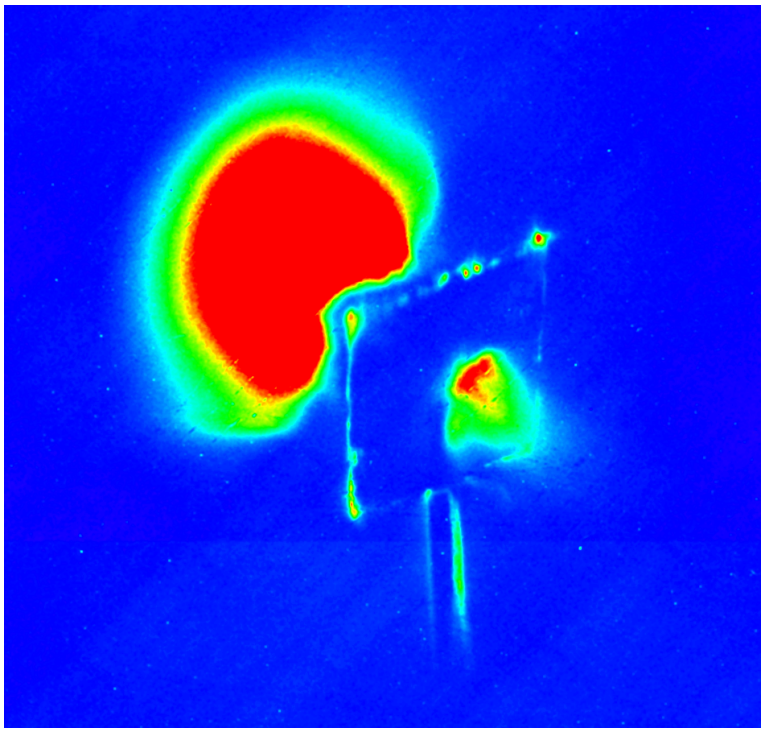

Figure 3.1: 68 eV XUV image of a typical target

The x-rays emitted from the target following K-shell ionization by hot electrons were collected using the following two instruments.

3.2.1 Spherically bent Bragg imager

The first instrument is a monochromatic K_α imager, which consists of a spherically bent Bragg crystal coupled to a charge-coupled device (CCD)(see Fig. 3.2). A Silicon dioxide crystal with a 38 cm radius of curvature, 3.082 $\mathring{A}$ 2d lattice spacing, and 2131 Miller indices was used. This required an incidence angle of 1.31° in order to satisfy the Bragg condition in second diffraction order for Cu K_α at 8.048 keV. The crystal

was located at an object distance of 21.4 cm resulting in a magnification of 7.92. The alignment procedure is straightforward and is discussed in details by Koch et al

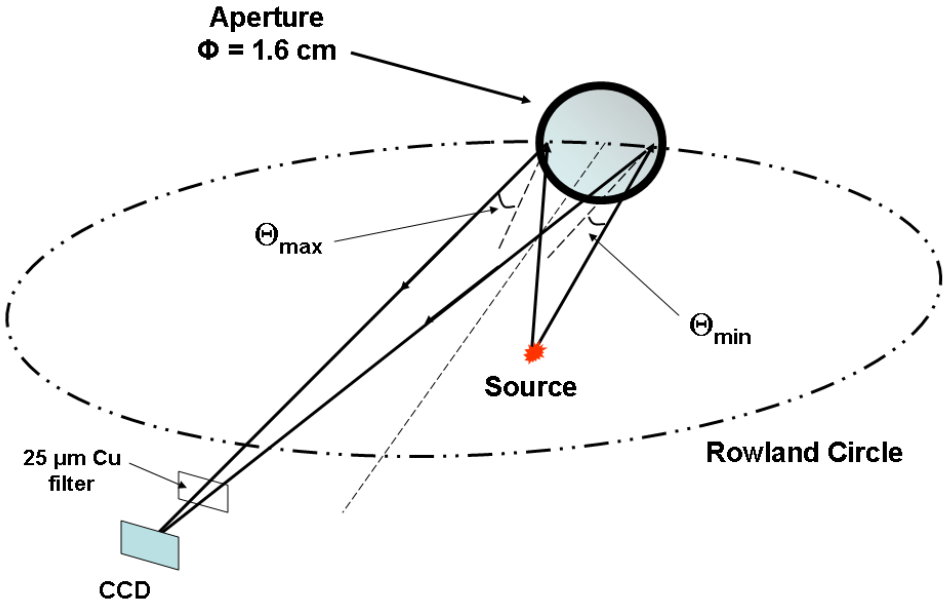

Figure 3.2: Cartoon showing spherically bent Bragg crystal imager .

[66]. Misalignments can happen especially when using a visible light (green laser for example) to align a non-calibrated or new crystals. The visible light reflects from the surface while x-rays are reflected at different planes deep into the crystal. As a result, the location on the image plane of the optical spot can be significantly different from the x-ray spot. If necessary, a detector with a large field of view (imaging plate for example), can be used to find the offset. The crystal should then be moved accordingly as to put the x-ray image in the center of the detector at the image plane. A 10 μm

astigmatism-limited spatial resolution [66] was obtained by putting a 1.6 cm diameter aperture in front of the crystal. The crystal viewed the rear side of the target at an angle of 37.8° with respect to the horizontal plane and 32° with respect to the target normal. The remainder of this section is devoted to determining the aperture-limited bandwidth of the crystal assuming a point source.

Let R_{cur} and R_{tcc} be the radius of curvature and the distance from the target chamber center to the center of the aperture of the crystal respectively (see Fig. 3.3). The arc length, l, from the center of the crystal to any point on the aperture is determined by,

$$l \ = R_{cur}\ \phi = R_{tcc}\ \beta \tag{3.1}$$

where ϕ and β are measured in units of radians (see Fig. 3.3).

Using the theorem stating that, in Euclidean space, the sum of the angles in a triangle is 180°,

$$\phi + \alpha + \theta = \pi \tag{3.2}$$

$$\beta + \alpha + \theta_0 = \pi \tag{3.3}$$

we can express the angle α as follows:

$$\alpha = \pi - \beta - \theta_0 \ = \ \pi - \frac{l}{R_{tcc}} - \theta_0 \ (rad) \tag{3.4}$$

Substituting expression (3.4) in equation (3.2) gives,

$$\phi = \underbrace{\theta_0 - \theta}_{\Delta\theta} + \frac{l}{R_{tcc}} \tag{3.5}$$

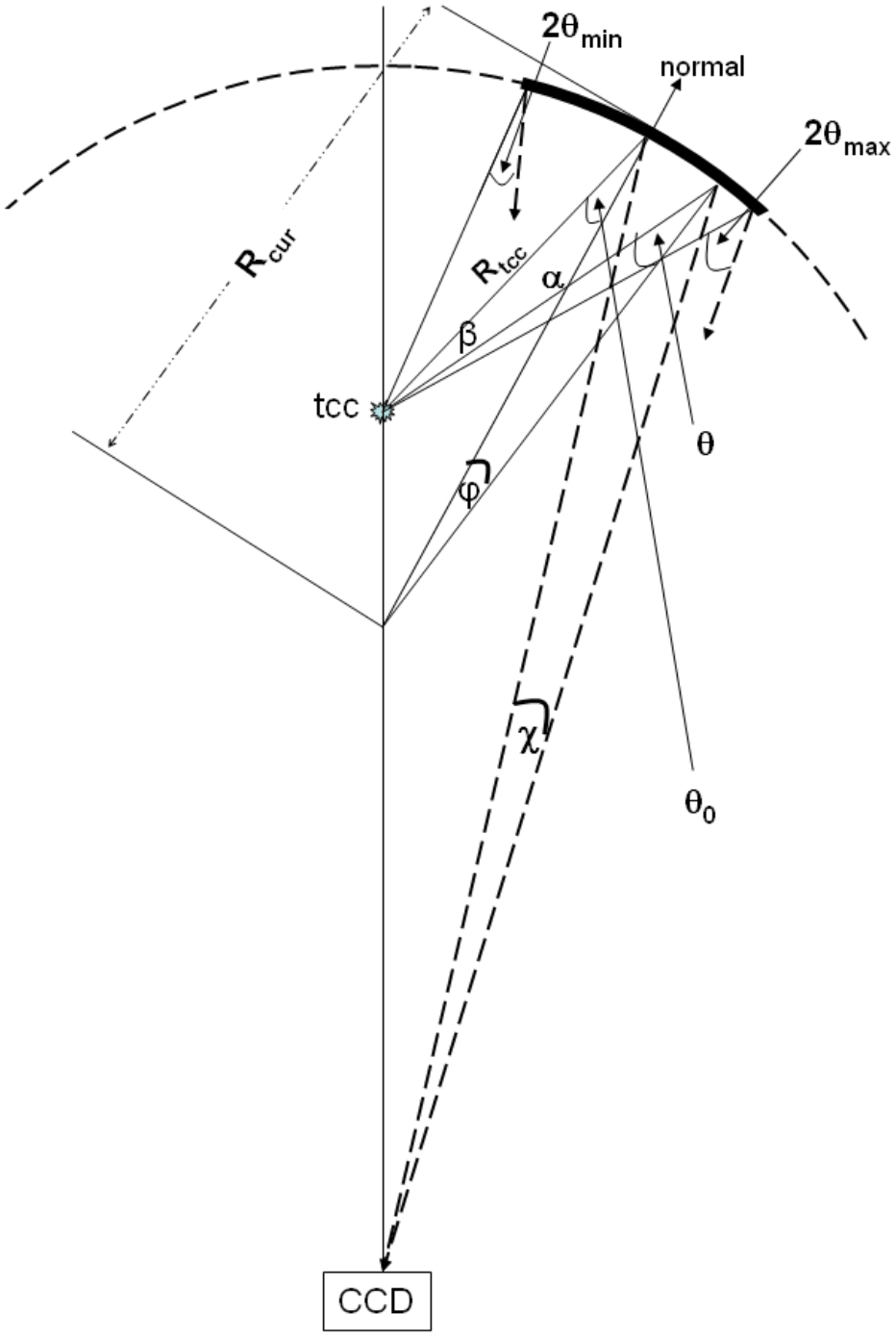

Figure 3.3: Bragg imager: R_{cur}, the radius of curvature. R_{tcc}, the distance from the target chamber center to the center of the aperture of the crystal .

When expression (3.5) for the angle ϕ is used in eq. (3.1), the following expression for the arc length is obtained,

$$l(\theta) = \left(\frac{R_{cur}}{1 - \frac{R_{cur}}{R_{tcc}}} \right) (\theta_0 - \theta) \tag{3.6}$$

To a first approximation, we can take the maximum arc subtended by the aperture to be equal to its diameter. Then the minimum and maximum angles subtended by the rays coming from the source and reflecting at locations adjacent to the aperture edges are given by,

$$\theta_{min} = \theta_0 - \frac{D_{ap}}{2} \left(\frac{R_{cur}}{1 - \frac{R_{cur}}{R_{tcc}}} \right)^{-1} = 0.364^\circ \tag{3.7}$$

$$\theta_{max} = \theta_0 + \frac{D_{ap}}{2} \left(\frac{R_{cur}}{1 - \frac{R_{cur}}{R_{tcc}}} \right)^{-1} = 2.236^\circ \tag{3.8}$$

The corresponding energies reflected at these angles are $E_{min} = 8.046\ keV$ and $E_{max} = 8.052\ keV$. As a result, the energy bandwidth defined as,

$$\Delta E_{ap} = E_{max} - E_{min} \tag{3.9}$$

is almost 6 eV wide. If we were to stop here and use this value for the energy bandwidth in subsequent calculations, we would be ignoring the fact that the area of the crystal reflecting at a constant angle of incidence decreases as we move away from the center (3.4). These areas, which we refer to as iso-areas, are arc bands of thickness δs.

For simplicity and without loss of generality we characterize these iso-areas by their length in the limit where their thickness is infinitesimally small, i.e. $\lim \delta s \to 0^+$,

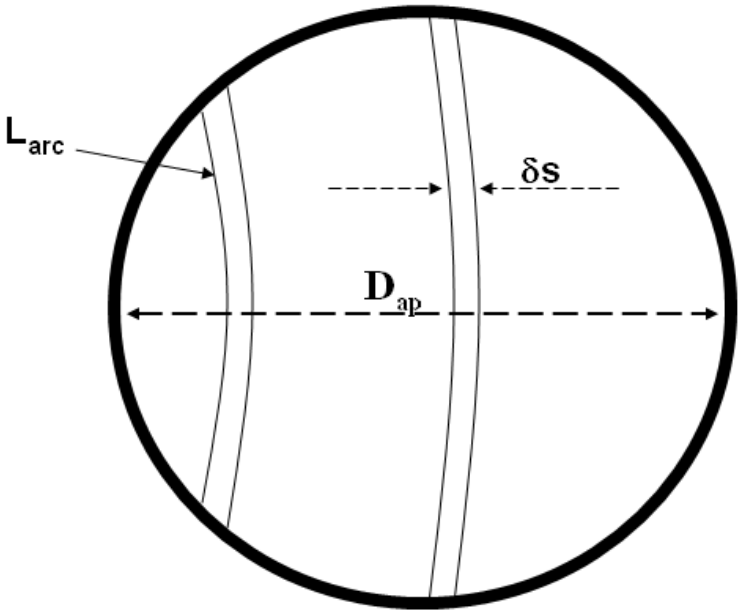

Figure 3.4: Iso-areas defined as the areas of the crystal reflecting at a constant angle of incidence.

$$L_{arc}(\theta) \approx 2\sqrt{\left[\frac{D_{ap}}{2}\right]^2 - l(\theta)^2} \tag{3.10}$$

The Bragg condition allows us to express θ as a function of energy,

$$\theta = \arccos\left[\frac{n\ hc}{2d\ E}\right] \tag{3.11}$$

with n=2 (second order), L_{arc} takes the form,

$$L_{arc}(E) \approx 2\sqrt{\left\{\frac{D_{ap}}{2}\right\}^2 - \left\{\left(\frac{R_{cur}}{1-\frac{R_{cur}}{R_{tcc}}}\right)\ \left(\arccos\left[\frac{1}{d}\frac{hc}{E_0}\right] - \arccos\left[\frac{1}{d}\frac{hc}{E}\right]\right)\right\}^2} \tag{3.12}$$

Using $L_{arc}(E)|_{max}$ as a normalization factor, we define the aperture-limited collection

efficiency of the crystal as the ratio,

$$\eta_{ap} = \frac{L_{arc}(E)}{L_{arc}(E)|_{max}} \times 100\% \tag{3.13}$$

As far as the aperture is concerned, the amount of photons collected by the crystal follows the same behavior as the iso-areas as shown by the plots of $L_{arc}(E)$ in Fig. 3.5-a and η_{ap} in Fig. 3.5-b.

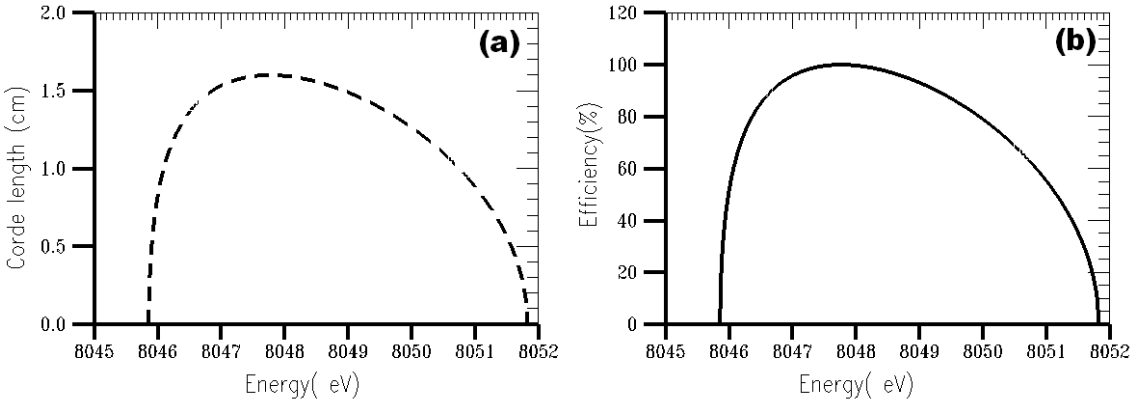

Figure 3.5: Aperture limited bandwidth of the crystal. (a) $L_{arc}(E)$, The length representing the iso-areas. (b) η_{ap}, The aperture-limited collection efficiency.

In the rest of this chapter, we characterize the aperture-limited bandwidth by the full width at half maximum of the function η_{ap}. This FWHM which we denote ΔE_{fwhm} is about 5.2 eV and we will refer to it throughout the text as the aperture energy bandwidth of the crystal.

The K_α photons were collected with a Princeton Instruments CCD camera, cooled to -20 ° Celsius. The model used was PI-SX1300, which is a high sensitivity back-illuminated digital system with 1340x1300 imaging array, 20 μm pixel size, and 16-bit

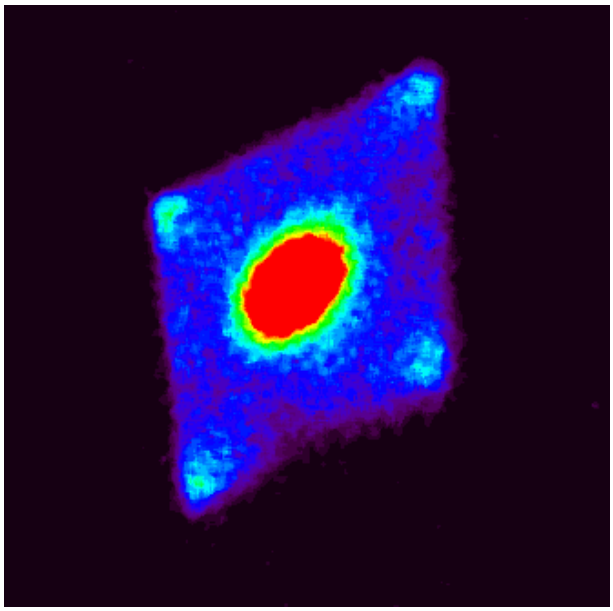

Figure 3.6: A typical monochromatic 2D spatially resolved Cu K_α image. The target is a 500 $\mu m \times 500$ μm 30 μm thick Cu foil

recording resolution. A 25 μm Cu filter was located in front of the CCD to narrow the bandwidth of the radiation reaching the detector by reducing the number of photons with energies above the Cu K-Shell photo-absorption edge. A typical monochromatic 2D spatially resolved image is shown in Fig.(**??**) (500 μm x 500 μm 30 μm thick Cu target).

3.2.2 Single hit CCD spectrometer

The second instrument used to collect the generated x-rays was a CCD camera operated in the single-photon counting regime. It directly detects photons without the use of any optical elements. For every 3.65 eV of photon energy absorbed in silicon a photoelectron is created. When the single photon counting condition is satisfied,

the number of photoelectrons created in a single pixel is a direct measurement of the energy of the absorbed photon. In Si the absorption of a Cu K_α photon (8.048 keV) will create around 2205 photoelectrons. The ability of CCD's to operate in this mode has been demonstrated for example by Schwartz et al [67], Yasuike at al [68], Stoeckl et al [43].

We used an SI 800-145 back-illuminated CCD camera manufactured by Spectral Instrument-Photonics. This camera has a 5% quantum efficiency at 8.048 keV for single hits with negligible spread of the absorbed x-rays energy over adjacent pixels [47]. It was located at a distance of 1.4 m from the target and surrounded with lead shielding to protect it from hard x-ray background and high-energy particles generated in the target chamber [43]. The photons were detected from the front side of the target at an angle of 16° with respect to the target normal [47].

3.3 Measurements of the K_α yield

3.3.1 Data processing

The data from the imager were processed and analyzed using the Interactive Data Language (IDL), a product of Research Systems, Inc. (RSI). Background images were taken in the same environment minutes before each shot with the CCD cooled to -20 C and the filter in front of the array. The background images are then subtracted from the data images pixel by pixel. The hard hits resulting from high energy photons

and particles interacting with the detector are removed from the images by applying a smoothing routine, whereby the value of a pixel is substituted by that of the median of its neighbors, if its value is higher by 10% or more than that of the median of the neighbors. The yield of K-shell emission from the target was then determined by integrating the images. The associated relative standard error was very small (0.2%-1.2%) due to the large number of photons detected .

The relative error bars for the single hit CCD data are estimated to be $\sim$ 40% based on the standard deviation of several measurements at the same experimental condition. The absolute uncertainty is estimated to be a factor of 2.4 based on an estimated uncertainty in the CCD quantum efficiency for single-pixel analysis [49] and the relative measurement error.

3.3.2 Experimental evidence of collected yield reduction

The Cu K_α yield obtained from both instruments is normalized to the total laser energy on target and plotted as a function of the target volume (Fig. 3.7).
The line with diamonds indicates the total amount of Cu K_α emission collected by the single hit CCD spectrometer in absolute units (ph/sr/J). The line with x's shows the amount collected by the crystal imager in arbitrary units (a.u). With decreasing target volume, it is clear that the yield obtained from the crystal imager decreases faster than the yield from the single hit CCD spectrometer. This effect, attributed to the temperature-induced line shifting and broadening, is more pronounced for

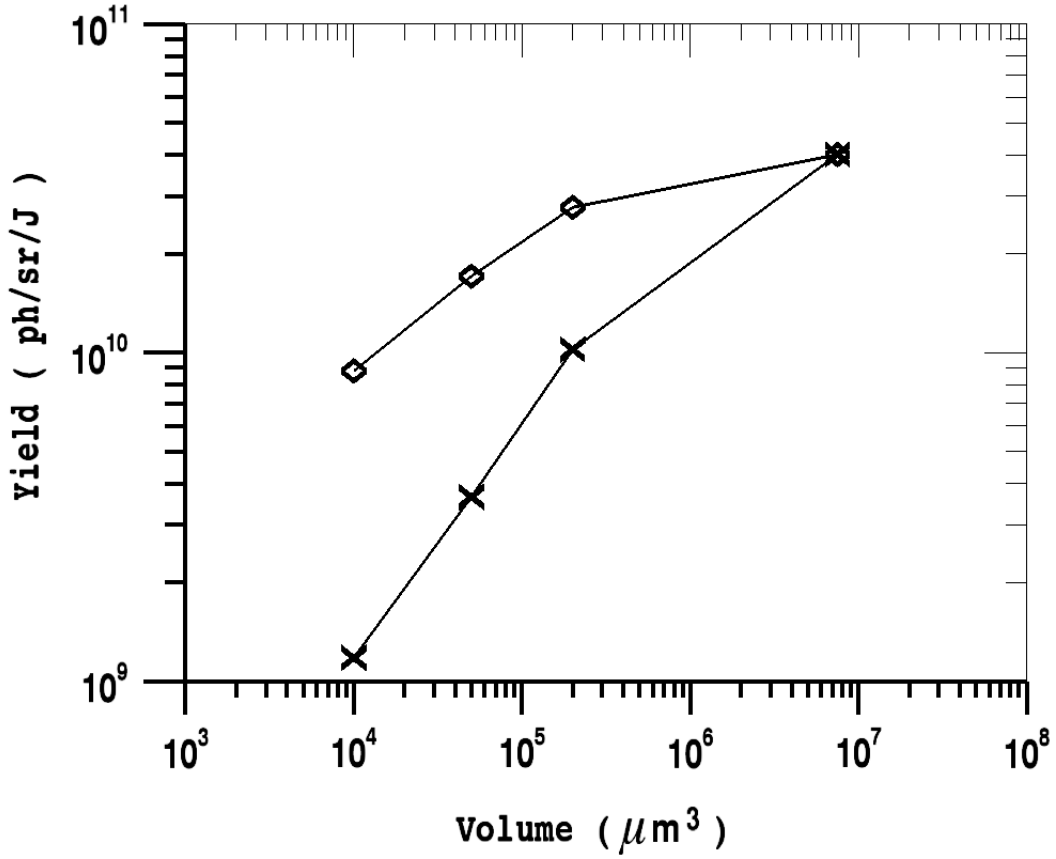

Figure 3.7: Cu K_α yield: diamonds, the absolute Cu K_α emission (ph/sr/J) measured by the single hit CCD spectrometrer. x's, the integral K_α emission from the crystal imager in arbitrary units (a.u)

small targets which attain high temperatures. In principle this reduction in the yield can be used as an independent temperature diagnostic when cross calibrated with the single-hit CCD spectrometer. The data point on the top right corner is from a 500 $\mu m \times 500$ μm 30 μm thick target. The remaining three data points are from 100 $\mu m \times 100$ μm targets with thicknesses of 1 μm, 5 μm, and 20 μm respectively.

3.4 The effect of line shifting on the collection efficiency

As a first attempt to explain the behavior of the K_α imager with increasing temperature, we consider a simplified approach which takes into account only the shifting of the line emission(the effect of both shifting and broadening is included in Subsec. 3.5.2). The energy shifts, $\Delta E_T = E_{shifted} - E_{cold}$, of Cu K_α line emission were generated using multiconfiguration Dirac-Fock (MCDF) calculations [18]. In order to interpret these energy shifts, I plotted the shifted energy, $E_{shifted} = E_{cold} + \Delta E_T$, as a function of the ionization state of the plasma $\overline{Z}$ (see Fig. 3.8). The area bounded by the two horizontal lines indicates the aperture bandwidth of the crystal. If the line falls within this area, then it will be reflected by the crystal otherwise it is out of range. It is clear from the figure that, as the temperature of the emitting plasma increases, the $K_{\alpha 1}$ line, indicated by the black solid line, start shifting. At first, the energy shift is negative since $E_{shifted} < E_{cold}$ implying a red-shifted $K_{\alpha 1}$ line. The minimum energy corresponding to $\Delta E_T^{min} = -5.5\ eV$ is reached at $\overline{Z} \sim 11$. Then ΔE_T becomes positive and the $K_{\alpha 1}$ is shifted toward higher energies, passes thorough its initial value at $\overline{Z} \sim 12$, and increases monotonically with $\overline{Z}$ after that. The $K_{\alpha 2}$ line (dashed line) which is 20 eV away from the $K_{\alpha 1}$ follows the same behavior with temperature. Since the aperture energy bandwidth of the crystal is narrower than

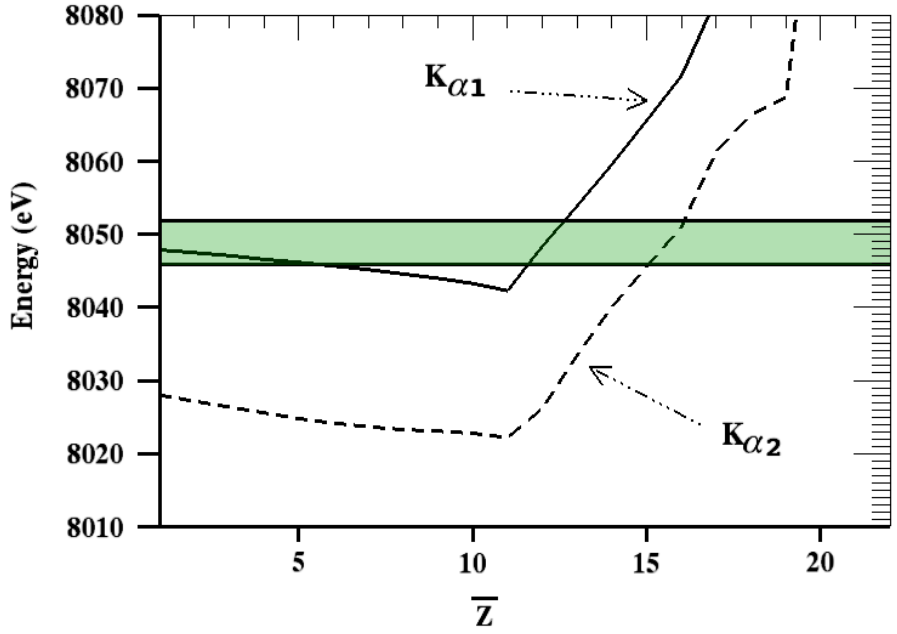

Figure 3.8: Energy vs, Z

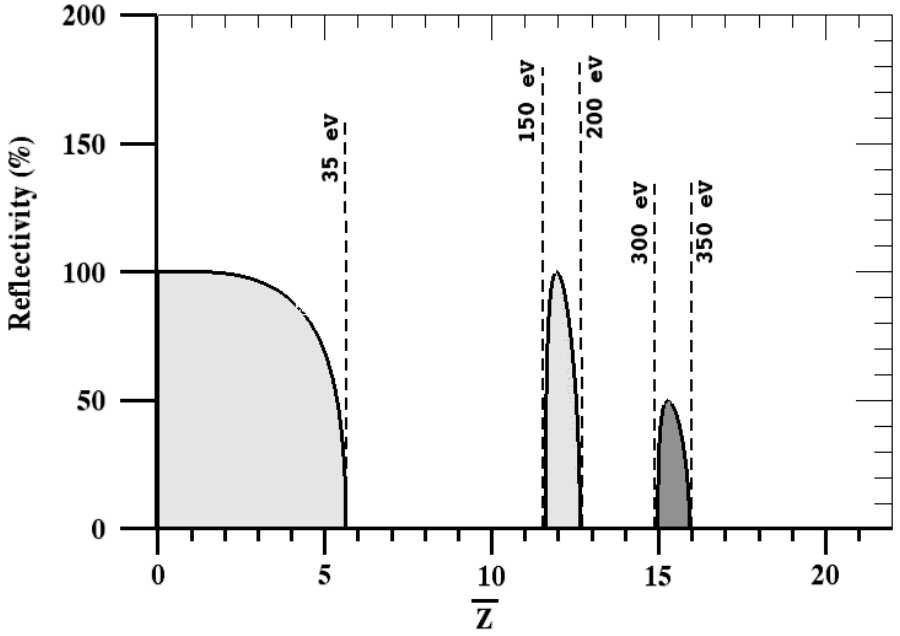

Figure 3.9: Reflectivity vs. Z

the maximum energy shift, i.e.

$$\Delta E_{ap} < |\Delta E_T^{max} - \Delta E_T^{min}| \tag{3.14}$$

then the collection efficiency of the crystal is nonzero only in certain charge state or temperature intervals for which,

$$|\Delta E_T| \leq \Delta E_{ap} \tag{3.15}$$

This illustrated in Fig. (3.9) by plotting the reflectivity [1] defined by eq.(3.13). The reflectivity decreases and has a nonzero value as long as the charge state $\overline{Z}$ is in the interval $[0, +6]$ which correspond to a temperature interval $[0\ eV, 35\ eV]$. Above $35\ eV$, both the solid and dashed lines are completely outside the bandwidth and the reflectivity vanishes. For plasma temperature between $150\ eV$ and $200\ eV$, the reflectivity is nonzero as the $K_{\alpha 1}$ line is within the aperture bandwidth. As far as the $K_{\alpha 1}$ line is concerned, no photons are collected above $200\ eV$ but it is possible to collect $K_{\alpha 2}$ photons at temperatures between $300\ eV$ and $350\ eV$. The brightness of $K_{\alpha 2}$ line is half that of $K_{\alpha 1}$, therefore, its reflectivity is two times lower. This is only a simplified picture illustrating the effects of the target temperature on the crystal collection efficiency. A more accurate study, which takes into account both shifting and broadening, is carried out in the next section.

[1] In this work, the reflectivity does not include the efficiency of reflection from Bragg planes. Since we are interested only in temperature effects on the diagnostic, we define the reflectivity or collection efficiency to be 100% when the target is cold and the shifting of the line emission is negligible.

3.5 Spectroscopic modeling of the K-shell emission

3.5.1 Comparison of spectra from detailed level (DL) and configuration-average (CA) models

Accurate and complete modeling of K-shell emission from multiply-ionized Cu ions immersed in hot, dense plasma is difficult due to the large number of states that must be included. The change in the ionic potential under valence-shell ionization by the bulk thermal electrons leads to a shifting and broadening of the K_α emission feature [70]. modeling of this line shifting and broadening as a function of the plasma temperature was carried out using two atomic codes: the flexible atomic code (FAC) [71] and the generalized population kinetics model FLYCHK [72]. FAC was first used to compare spectra from detailed level (DL) and configuration-average (CA) models in order to test the accuracy of the CA model used later in FLYCHK for spectral synthesis.

Fig.(3.10) shows comparisons of spectra calculated using local thermodynamic equilibrium populations (LTE) in detailed level (DL) and configuration-average (CA) models. The statistical assumption has been verified using the collisional-radiative model SCRAM [17]. The data for each model was calculated using FAC in either standard (detailed fine structure) or unresolved-transition-array (UTA) mode. The

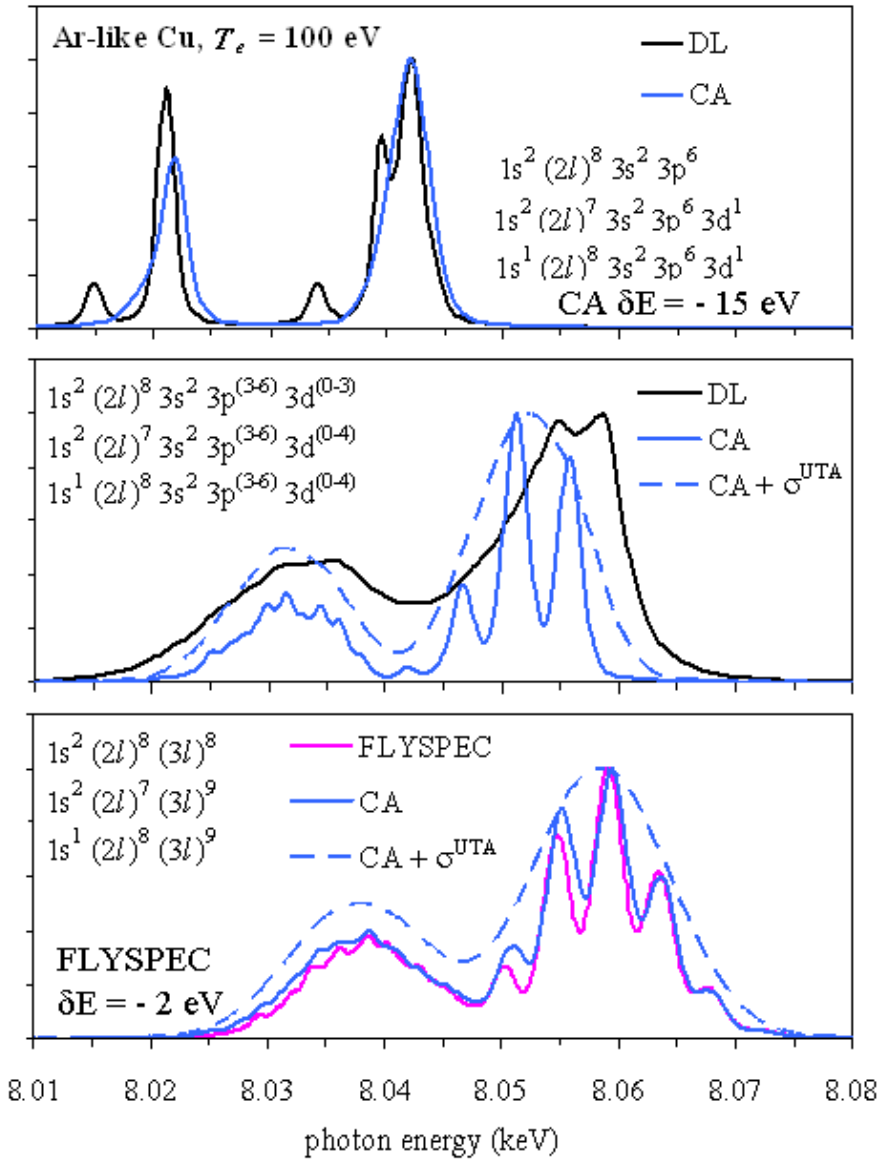

Figure 3.10: Comparison of model predictions for K-shell emission from Ar-like Cu. The spectra change significantly as the number of modeled configurations is increased (top to bottom). Configuration-averaged (CA) models show reasonable agreement with detailed-level (DL) models when transition energy shifts δE and UTA widths σ^{UTA} are included.

two plots show the comparison of DL and CA with varying degrees of completeness in level structure. While the energies of CA transition arrays within the dashed-lines envelopes are not perfectly coincident with corresponding features in the DL spectra, the centroids and overall widths of the CA features are in reasonable agreement. Therefore, for the purpose of this paper, it is adequate to use the CA model which reduces the model complexity.

3.5.2 FLYCHK Cu K-emission spectra

In order to compute the K_α line shifts and broadening at a given thermal electron temperature, FLYCHK first computes the level population in the super-configuration model and generates emission spectra in the configuration-average (CA) model kinetics, and then FLYSPEC calculates spectra based on CA atomic data from Mau Chen's DHS code [18, 19]. FLYSPEC predictions for Ar-like Cu are in good agreement with the FAC-based CA calculations (see Fig. 3.10). In our experiment the hot electron temperature was about 600 keV as estimated, from the laser intensity, using Beg's scaling law [75]. The hot electron density was in the range of 10^{-4} to 10^{-3} of the total electron density. This estimate is based on experimental laser-to-electron conversion efficiency [24] and Cu K_α spot size [33]. The total electron density is computed self-consistently by the solid ion density times the mean charge state. While the absolute K_α intensity is a function of hot electron temperature and density, the spectral shape is rather insensitive to them and depends on the thermal electron temperature as long

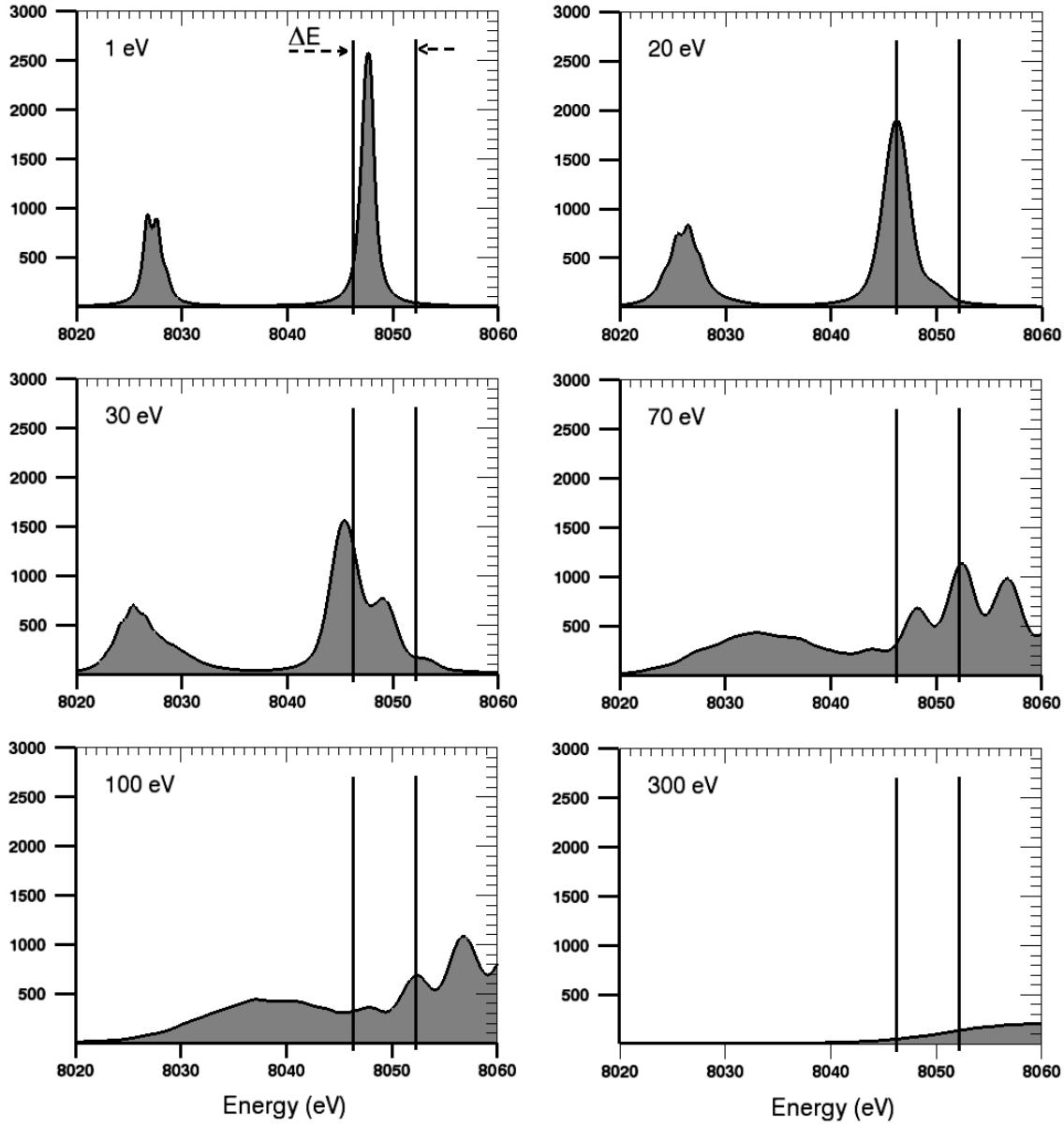

Figure 3.11: FLYCHK spectra for temperatures ranging from 1 eV to 300 eV. The two vertical black lines indicate the maximum and minimum energies reflected by the crystal

as the fraction of hot electrons is less than 10% of total electron density, which is the case in our experiment. The calculated spectra are plotted in Fig.(3.11) for thermal electron temperatures ranging from 1 eV to 300 eV along with the aperture energy bandwidth (black vertical lines).

3.6 Collection efficiency of the Bragg crystal imager

The Cu K_α emission line, in addition to broadening, exhibits a negative shift at first as shown by the peak moving to the left (Fig. 3.11). As the plasma temperature increases, the broadening increases and the energy shifts become positive. The ratio of the area under the curve bounded by the aperture energy bandwidth to the total area under the curve is proportional to the collection efficiency of the crystal. In the calculation of the collection efficiency $\epsilon(T)$ a normalization factor was applied. The chosen normalization made the collection efficiency 100% when the target is cold ($T = 0\ eV$) and the aperture energy bandwidth centered around the cold K_α. Fig. 3.12 (dashed line with triangles) shows that $\epsilon(T)$ is a decreasing function of temperature. Between 0 and 20 eV, $\epsilon(T)$ steeply decreases to about 25%. Due to the time-integrated nature of the diagnostic, the amount of radiation collected by the imager at a given time is proportional to the collection efficiency at that time and therefore the temperature. If $Y(T)$ is the K_α yield from a 1 μm solid density Cu

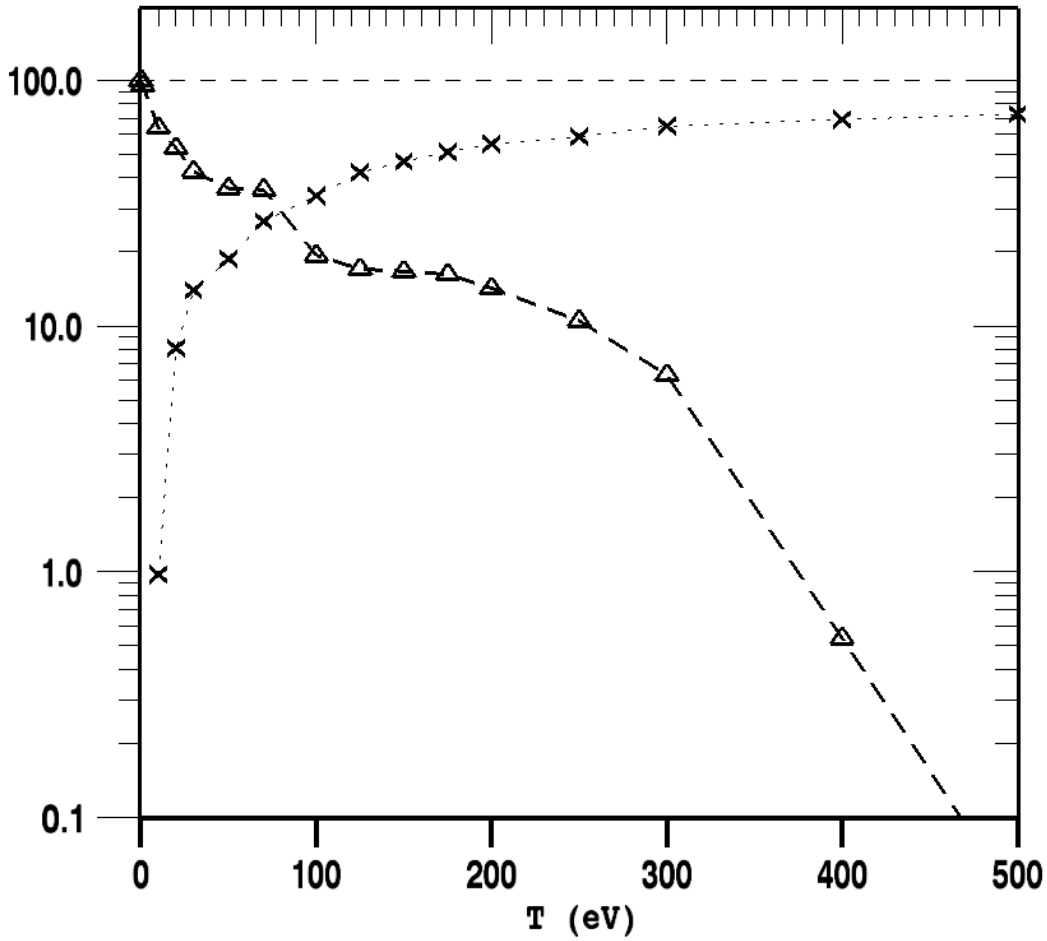

Figure 3.12: Dashed line with triangles, the crystal imager collection efficiency as a function of target temperature. Dotted line with x's, total K_α yield when the slab is heated to temperature T.

slab at temperature T, then the yield collected by the imager at this temperature is $Y(T)\epsilon(T)$. The total yield collected when the slab is heated from T_0 to T_{max} is, therefore, given by the following integral,

$$\int_{T_0}^{T_{max}} Y(T)\epsilon(T)\ dT \tag{3.16}$$

The above integral quantity is shown in Fig. 3.12 (Dotted line with x's). It increases rapidly with temperature and reaches a plateau at about 100 eV. One of the implications of this temperature-dependence of the collection efficiency is the saturation of the amount of photons collected. This effect will impose limitations on the use of spherically bent Brag crystals as diagnostics for very hot plasmas.

3.7 Numerical model

The temperature throughout the target is not constant but rather decreases with depth and radial distance from the laser focal spot. Furthermore, the interaction of the laser beam with the target is local and time varying. To account for these two effects in interpreting our data, I used a modified version of the numerical model described in chapter 2. This modified code can run in either "Thick target" or "Thin target" modes.

For thick targets, the transport of the suprathermal electron beam is governed by both the collisions and the potential induced by charge separation. The heating is a result of both collisions and return currents. Thus, the model in the previous

chapter is applicable and the temperature in each zone, $T(r, z, t)$, is determined from the specific energy deposited using LANL SESAME equation of state tables.

For thin targets the situation is different. The electrons traverse the target and set up an electrostatic sheath of thickness of the order of Debye length. The sheath was characterized by the electric field strength of order $T_h(r, t)/e\lambda_D$. The Debye length, λ_D, is a function of the electron density and temperature. These last two quantities are functions of time. Therefore the potential which is the product of electric field strength and Debye length is also a function of time. The first electrons created by the leading edge of the laser pulse at earlier time establish a sheath with a potential $\varphi(t_0)$. This potential is not strong enough to influence the electrons. The incoming electrons at later time increase the magnitude of the potential due to more charge separation. In the calculation, this potential is evaluated as a function of time. When the value of $\varphi(t)$ is equal to their mean energy, electrons coming at that time reflect from the rear surface. These electrons are also reflected from a similar Debye sheath at the front surface. The process is repeated for the lifetime of the electrons, hence the name "refluxing". The first electrons establishing the sheath are not circulated. The specific energy deposited in the target is due to collisions only, the electrons act as their own return current by virtue of refluxing.

For the laser pulse, we used the following double Gaussian profile, based on the experimentally measured focal spot:

$$I_{Laser}(r,t) = \exp\left[-\left(\frac{t-t_p}{\tau}\right)^2\right]\left\{ I_1 \exp\left[-\left(\frac{r}{R_1}\right)^2\right] + I_2 \exp\left[-\left(\frac{r}{R_2}\right)^2\right]\right\} \tag{3.17}$$

here $R_1 = 5\ \mu m, R_2 = 40\ \mu m$, $I_1 = 5 \times 10^{18}\ W/cm^2$, $I_2 = 1 \times 10^{17}\ W/cm^2$, $t_p = 5\ ps$, and $\tau = 2.5\ ps$.

The hot electrons generated by the interaction of this pulse with the target are described by a local Maxwellian distribution,

$$f_E(E,r,t) \propto \frac{\sqrt{E}}{T_h(r,t)^{3/2}} \times \exp\left[-\frac{E}{T_h(r,t)}\right] \tag{3.18}$$

where the local temperature, $T_h(r,t)$, is given by Beg's scaling law [75],

$$T_h(r,t) = 100\ \left[\frac{I_{Laser}(r,t)}{10^{18}\ W/cm^2}\right]^{1/3} \times keV \tag{3.19}$$

The distribution, $N_{ph}(r,z,t)$, of K_α photons induced by these electrons is then calculated according to,

$$N_{ph}(r,z,t) = \int n_{Cu}\ \Delta z\ \sigma(E)\ N_h(r,z,t,E)\ dE \tag{3.20}$$

where $N_h(r,z,t,E)\ dE$ is the number of hot electrons with energies between E and $E+dE$ in the zone, n_{Cu} is the copper number density, and $\sigma(E)$ is the electron impact ionization cross section in Cu. For $\sigma(E)$ we used the Deutsch-Mark expression,

$$\sigma(E) = 2\pi\ r_{1s}^2\ g_{1s}\ f\left(\frac{E}{E_{1s}}\right)\ F\left(\frac{E}{E_{1s}}\right) \tag{3.21}$$

where r_{1s} is the radius of maximum radial density of Cu 1s-shell from the tables of Desclaux [57], g_{1s} is a weighting factor, E_{1s} is the binding energy of 1s electrons, and the functions f, F are those in reference [56].

3.8 Discussion and Summary

3.8.1 Absolute yield and spatial pattern of intensity

Using the model described above both the local and total K_α yields were determined. The total number of photons per steradian from the target is given by the following integral,

$$N_T = \frac{1}{4\pi} \int \int \int N_{ph}(r, z, t) \exp -\{\mu(s - z)\} \; dt \; dz \; dr \tag{3.22}$$

here μ is the attenuation coefficient of K_α radiation in Cu. N_T is plotted as a function of the target volume in Fig. 3.13 (dashed line with triangles). It is in good agreement with the experimental data from the single hit CCD spectrometer (solid line with diamonds). The experimental yield from the 1 μm thick target is little lower than the modelled. The reason for this may be that the electrons lose their energy to channels other than electron impact ionization (pdV work accelerating protons for example). When the previously determined collection efficiency correction is applied, the total number of photons per steradian collected by the imager is reduced to:

$$N_{T_r} = \frac{1}{4\pi} \int \int \int N_{ph}(r, z, t) \exp -\{\mu(s - z)\} \; \epsilon(r, z, t) \; dt \; dz \; dr \tag{3.23}$$

where $\epsilon(r, z, t)$ is the local collection efficiency.

N_{T_r} is plotted in Fig. 3.13 (dashed line with open squares). Also plotted are the experimental data from the imager (solid line with x's). The value of N_{T_r} for the 30 μm thick target was used as a normalization point for the experimental data since these data were not measured in absolute units. The thickest target was chosen based on the fact that it is the least susceptible to temperature effects. The single hit CCD data were corrected for the reabsorption in the target material by comparing the yields obtained from the model with and without the attenuation on. The corrections were 25%, 21%, 6%, and 1% for the 30 μm, 20 μm, 5 μm, and 1 μm thick targets respectively. Both the modelled and experimental results are in a good agreement, showing the temperature-dependence of the collected K_α yield. The total yield was reduced by a factor of 3 for the thickest target and by a factor of 18 for the thinnest one.

As an example, the model is applied to the spatial pattern of K_α intensity for the 30 μm thick target. A useful approach in analyzing 2D spatially resolved images is a lineout through the image. Such a lineout is plotted in Fig. 3.14 (dashed line with triangles). It was taken in the horizontal direction through the middle of the K_α image of Fig. 3.6. The dashed line is the modelled lineout with the line shifting and broadening taken into account. The solid line is the true lineout that one should expect if the imager were not susceptible to temperature effects. the reduction was almost uniform ranging from 62% in the center to 56% at the edges. As consequence

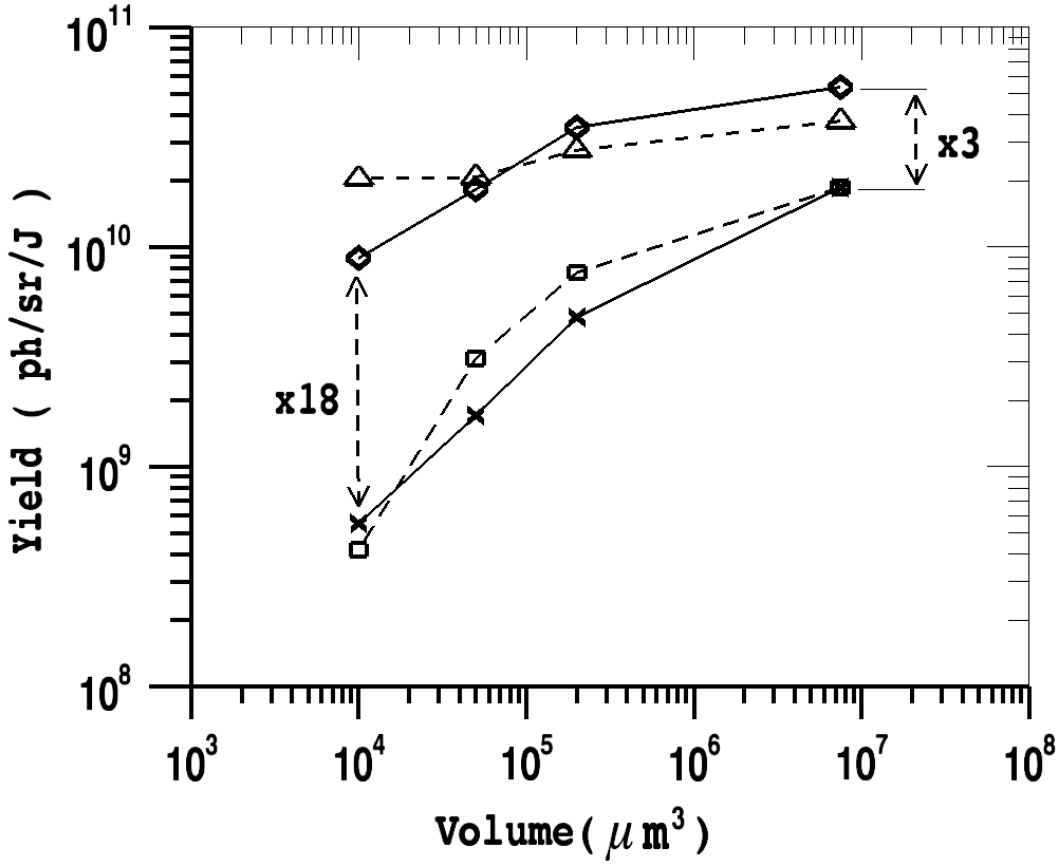

Figure 3.13: Comparison of the experimental and modeled absolute K_α yields. Experimental: solid line with diamonds from the single hit CCD, solid line with x's from the crystal imager normalized as discussed in the text. Modeled: dashed line with squares, the yield from the imager with temperature effects. dashed line with triangles, the absolute yield.

the full width at half maximum remained unchanged while the brightness of the image is reduced. For thinner targets, the reduction was more pronounced at the center than the edges. This resulted in an apparent increase in the FWHM. Neglecting these effects when interpreting data will lead to erroneous results for the FWHM more so in case of high temperatures.

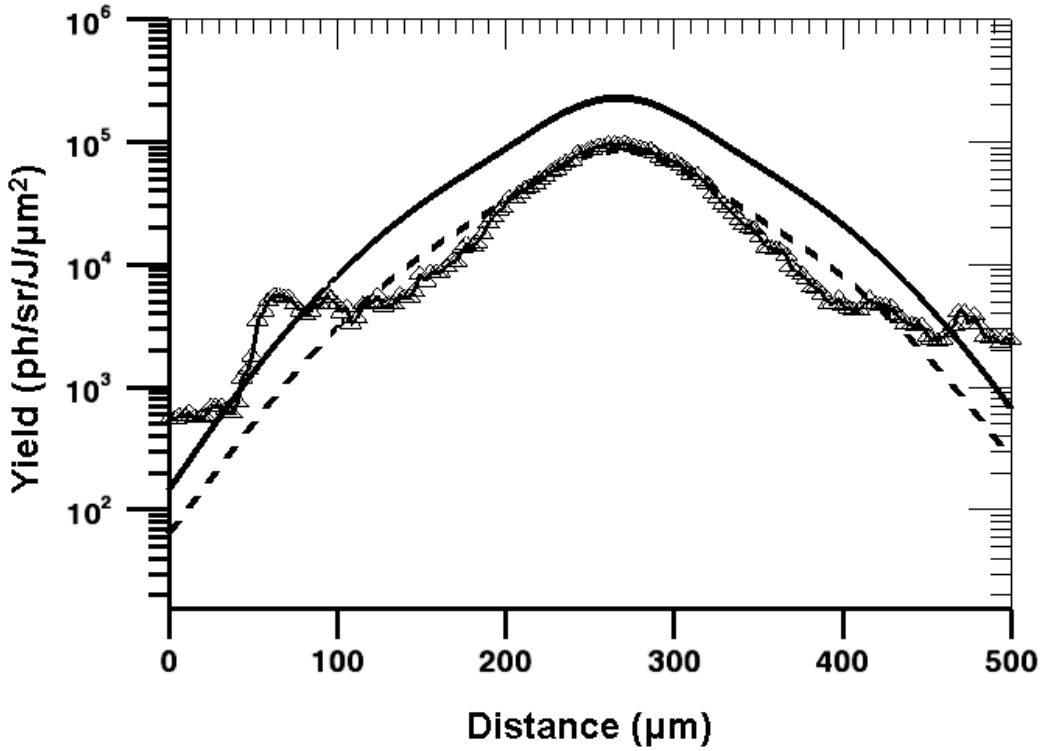

Figure 3.14: Cu K_α spatial pattern of intensity: solid line with triangles, a horizontal lineout of the image of the 500 μm x 500 μm 30 μm thick target in Fig. 2. Solid line, model lineout with no temperature effects. Dashed line, model lineout with temperature effects.

3.8.2 Isochoric heating

The reduction in collected K_α photons can be used as a temperature diagnostic. Since this diagnostic is time integrated, only an average temperature can be inferred. This is done by determining the yield reduction curve from that of the collection efficiency $\epsilon(T)$ of Fig. 3.12. The reduction in the K_α yield ,

$$R(T) = \frac{\int_0^T \epsilon(T')\ dT'}{\int_0^T \epsilon_{cold}(T')\ dT'} \tag{3.24}$$

defined as the ratio of the area under the $\epsilon(T)$ curve to the area under $\epsilon_{cold}(T)$ curve, is plotted in Fig. 3.15. The quantity $\epsilon_{cold}(T)$ is the collection efficiency in the absence of shifting and broadening. Using Fig. 3.13 to determine the ratios, the temperature of the targets is determined by finding the temperature that produces the same reduction in Fig. 3.15.

The experimental ratios were 0.32, 0.13, 0.09, and 0.06 corresponding to temperatures of 82 eV, 253 eV, 400 eV, and 610 eV for the 30 μm, 20 μm, 5 μm, and 1 μm thick targets respectively. These average temperatures are plotted in Fig. 3.16.

The errors due to the uncertainty in the 2d spacing of the crystal were estimated as follows. From previous experiments using the same crystal and the same laser system, we have imaged cold Cu K_α line [33]. Since the crystal was set to an angle of 1.31 degrees, a cold K_α line with 2.0 eV full width at half maximum linewidth would be imaged only if the 2d spacing is between $2d_{min} = 3.0816\ \mathring{A}$ and $2d_{max} = 3.0824\ \mathring{A}$

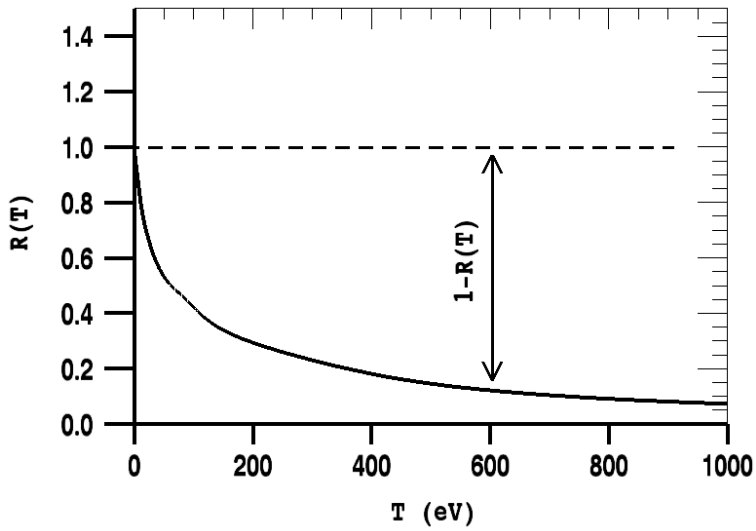

Figure 3.15: reduction curves: solid line, ratio in the presence of shifting and broadening. dashed horizontal line, ratio in the absence of shifting and broadening which is equal to unity.

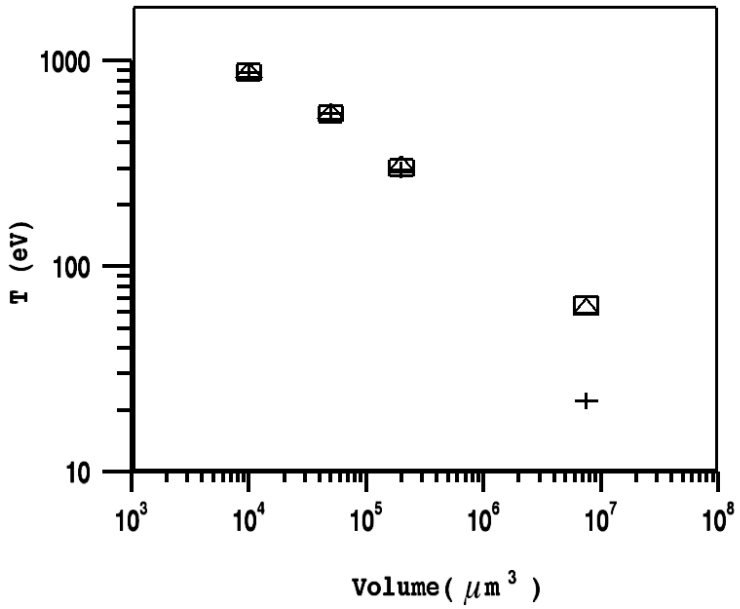

Figure 3.16: Average temperatures of the targets. Squares, the temperature in the case of $2d = 3.082$ $\mathring{A}$. Triangles, the temperature in the case of $2d_{max} = 3.0824$ $\mathring{A}$. Pluses, the temperature in the case of $2d_{min} = 3.0816$ $\mathring{A}$

angstroms as illustrated in Fig. 3.17. As long as the intersection of the 2d curves with the vertical axis $\Theta = 1.31°$ lies within the grey area an image will be recorded.

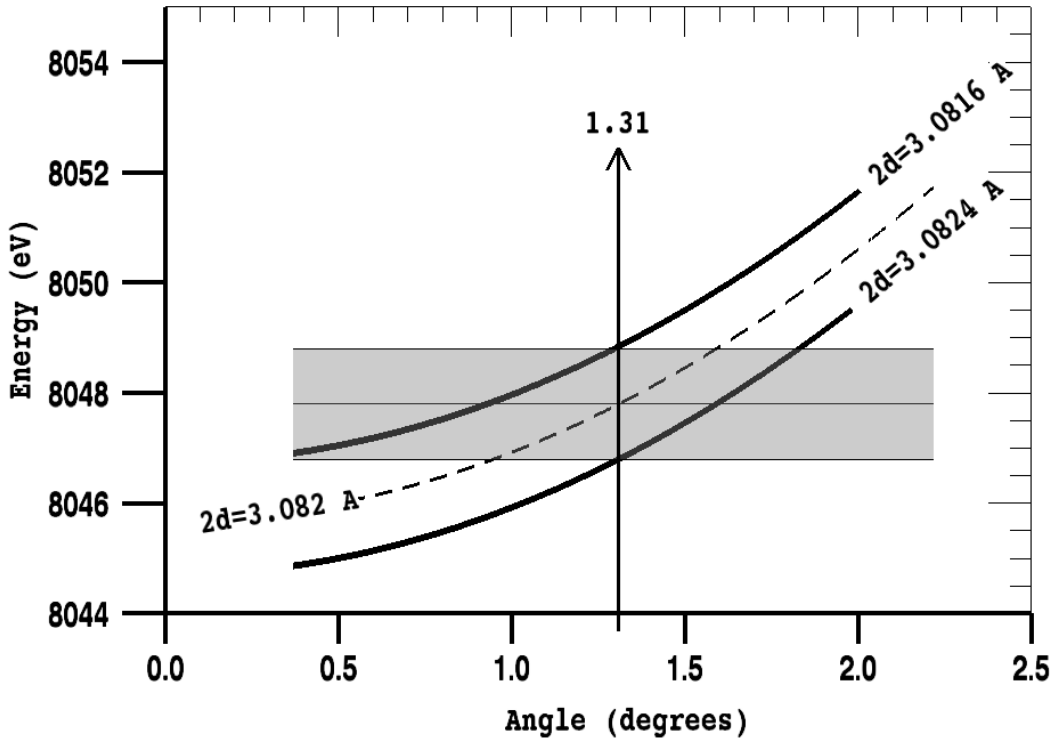

Figure 3.17: 2d ratio

Similar curves to the ones in Fig. 3.12 were obtained for $2d_{min}$ and $2d_{max}$. These efficiency curves were, then, used to determine the temperatures of the targets (Triangles and pluses in Fig. 3.16). At high temperatures, the error introduced is less than 1% for both $2d_{min}$ and $2d_{max}$. This small error is due to the broadening of the K_α line at high temperatures. At low temperatures, the error is 32% for $2d_{min}$ due to the fact that the K_α line is still narrow and starts, initially, to shift away from the

aperture energy bandwidth ($8.047 - 8.052\ keV$). For $2d_{max}$, the initial shift of K_α line is in the direction of lower energies which brings it toward the center of the aperture energy bandwidth ($8.045\ keV$ to $8.050\ keV$). As a result, the error is reduced (less than 1.2%).

In summary, experimental evidence of temperature sensitivity of Cu K_α imaging efficiency using a spherical Bragg reflecting crystal was presented. The experimental data were interpreted using two models. First, the temperature-dependent spectrum of Cu K-shell emission was modelled using FLYCHK in the configuration-average (CA) mode. Then, a numerical transport model which takes into account the electron refluxing was used to obtain both the absolute K_α yield and the spatial pattern of K_α intensity. It was found that both the brightness and the pattern of K_α intensity are affected by the rise of the target temperature. The reduction in the absolute K_α yield was used to determine the average temperature of the targets. The errors introduced by the uncertainty in the 2d spacing were found to be insignificant at high temperatures.

Acknowledgements

The spectroscopic modeling of the Cu K-line emission were carried out by Stephanie Hansen, H. -K. Chung in collaboration with Mau Chen. S. Hansen kindly provided Fig. 3.10 which we also used in our paper. H. Chung provided the raw spectra from FLYCHK which I processed to generate Fig. 3.12. W. Theobald processed the single hit CCD data.

Chapter 4

Studies of Energy Transport by Short-Pulse High-Intensity Laser Generated Electrons Using K- shell Spectroscopy of Layered Targets.

We conducted a systematic study of an ultrashort high-intensity laser-generated electron beam energy transport using the Vulcan laser facility in the United Kingdom. These experiments were performed with a 0.7 ps 500 J laser beam. The targets were 5 μm thick Mo/Ni/V sandwiches. The Vanadium layer was 1 μm thick and located at the rear of the target. The Nickel layer was 0.5 μm thick and located at various depths into the target. Highly Ordered Pyrolytic Graphite (HOPG) Crystals were

used to obtain x-ray spectra generated by the interaction of this 5×10^{20} W/cm^2 *laser pulse with the solid targets. Experimental evidence of temperature gradients and the formation of hot, thin surface layer at the front of the target (*$\sim$ 1 μm*) were obtained. A 2D spatially resolved* Ly_α *image of the target showed a* 25 μm *hot spot. 2D particle-in-cell (PIC) simulations confirm beam filamentation and surface heating. This chapter has three main parts: experimental data, spectroscopic modeling, and Particle-In-Cell simulations.*

4.1 Experimental setup

4.1.1 RAL Petawatt laser and interaction chamber

These experiments were carried out in the recently upgraded target area of the vulcan laser facility. The interaction target chamber has a rectangular shape with dimensions of 4m x 2m x 2m (Fig. 4.1). It has 2 doors which allow easy access to the diagnostics inside. The laser pulse, obtained using OPCPA, has a diameter of 60 cm when entering the chamber. A turning mirror reflects the beam toward an f/3 off-axis parabola where it is focused on the target. The targets are mounted on a rotating wheel. This allowed us to take more than one shot without breaking vacuum. The diagnostics were numerous and diverse and include 68 eV XUV imager, 256 eV XUV imager, Cu K_α imager, pinhole cameras, front and rear Highly Ordered Pyrolytic Graphite Crystal spectrometers, etc.

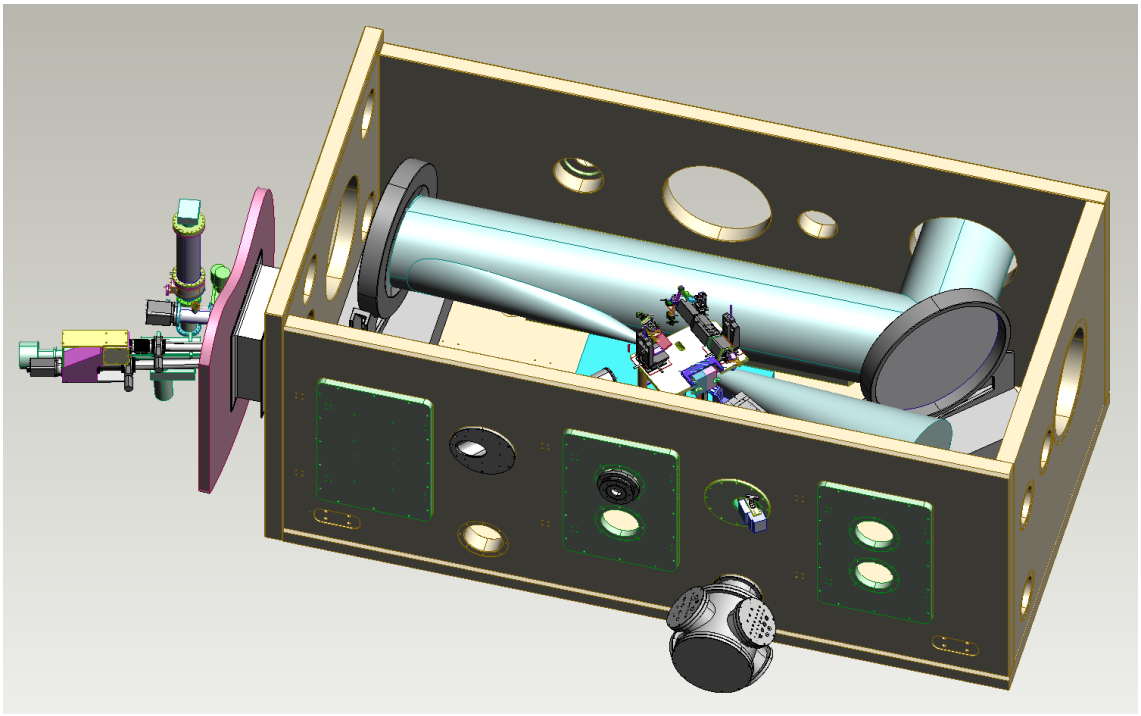

Figure 4.1: RAL Petawatt laser and interaction chamber

During the preparation week, scans of the laser focal spot along the direction of its propagation were taken. Fig. 4.2 shows a set of three 16-bit images taken at lower energies. Image (a) was taken at a location of -200 μm between the parabola and target chamber center. Image (b) is the best attainable focus. Image (c) was taken at +200 μm from best focus in the direction of laser propagation. It is clear from these images that the focal spot is far from being a nice symmetric spot. Moreover, the propagating laser beam exhibit completely different spatial distributions at two symmetric locations as shown by Figure 4.2-(a) and Figure 4.2-(c). Any lineout through the image of the best focus will result in an asymmetric profile which is sometimes

difficult to implement in plasma simulation codes. Any computer simulation using an ideal gaussian profile is attempting to solve a problem with different conditions than the experimental ones. Therefore, it is the task of the experimenter to bridge

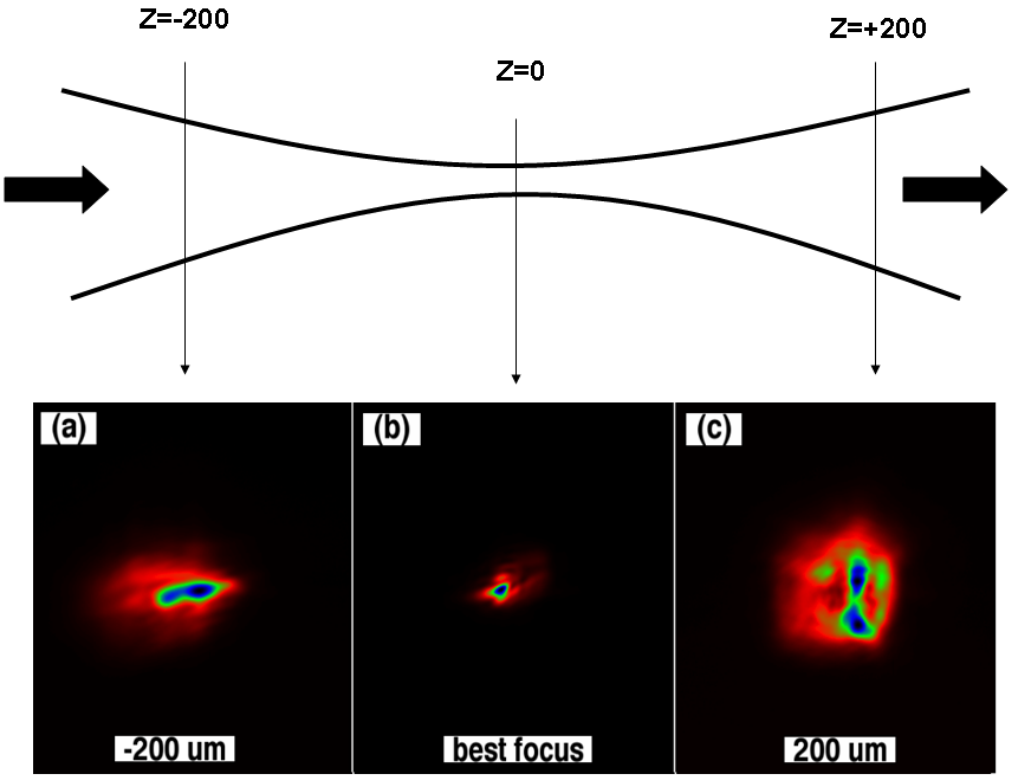

Figure 4.2: Vulcan Petawatt focal spot: (a) focal spot at -200 μm, (b) best focus, (c) focal spot at +200 μm.

this gap and provide the modeler with a suitable laser profile. This profile should be symmetric and easy to use and at the same time it should be as close as possible to the experimental values. Based on our experimental observations, the Vulcan laser tends to have a profile which is best fitted by a double gaussian in space.

4.1.2 Highly Ordered Pyrolytic Graphite Crystal (HOPG)

We used 5 μm thick Molybdenum targets with two different layers. The Vanadium layer was 1 μm thick and located at the back of the target. The Nickel layer was 0.5 μm thick and located at various depths into the target. The main diagnostics were two Highly Ordered Pyrolytic Graphite Crystals (HOPG) spectrometers. The first one, referred to in this chapter as "front HOPG", was located at the front of the target with a viewing angle of 5° and 30° with respect to the laser axis in the horizontal and vertical planes respectively (Fig. 4.3-a). The second one, referred to as "rear HOP", is located behind the target in the same vertical plane as the laser, at an angle of 30° with respect to the horizontal plane (Fig. 4.3-b). Both HOPG's have two channels set in such a way that the top channel spectrally resolves the vanadium spectra, while the lower channel resolves the nickel spectra (Fig. 4.3-c). The spectra were recorded on an imaging plate detector of 80×90 mm^2 effective area and 17.5 μm pixel size. We used a total of eight highly oriented pyrolytic graphite (HOPG) crystals (four for front HOPG and four for rear HOPG). For each channel two crystals, 48 mm long, were glued together to act as a single crystal of 96 mm length. This was necessary in order to cover both Ni and Cu spectra without the need to realign when switching between different targets [1]. Highly oriented pyrolytic graphite (HOPG) crystals are characterized by their degree of mosaic spread which is a measure of how highly ordered is the crystal. The lower the mosaic spread the more highly ordered is the

[1] These Ni targets were a small fraction of different targets used in this run

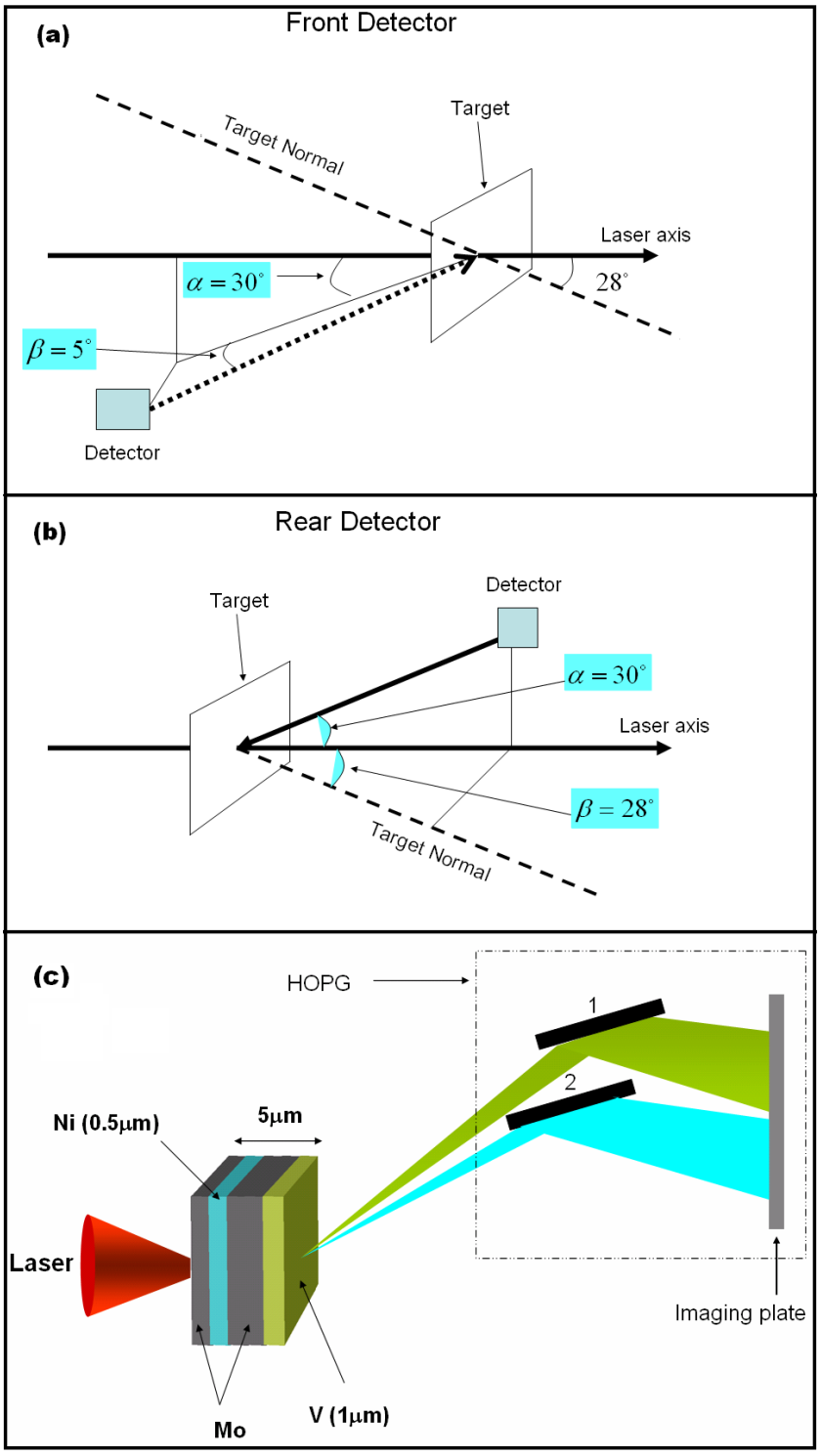

Figure 4.3: Front and Rear HOPG spectrometers. (a) Front HOPG viewing angles. (b) Rear HOPG viewing angles.(C) Vanadium emission (channel-1). Nickel emission (channel-2)

crystal. Our HOPG crystals were manufactured by GE Advanced Ceramics and have a low mosaic spread $\gamma = 0.4°$; they are known as ZYA [76].

4.1.3 Data processing

The Ni spectra recorded on the imaging plates give the x-ray intensity as a function of the pixel number. In order to obtain a plot of the x-ray intensity as a function of the x-ray energy we need to determine the dispersion function. In other words, we need a transformation that will allow us to express the x-ray energies as a function of the pixel number. This is done in two steps:

- First step: transformation of pixel number to coordinate on the y-axis.

Let us represent each pixel on the image plate by its cartesian coordinates (x_{pix}, y_{pix}) as illustrated in Fig. 4.4. To a good degree of accuracy, the image plate is set in such a way that all photons with the same energy have the same x_{pixel}. Therefore, It is sufficient to find a function which maps the coordinate y_{pixel} into the real axis. Since the pixel size is 17.5 μm and the effective length is 9 cm, then y_{pixel} axis spans the values from 1 to 5143.

The function Λ_1, defined by

$$\begin{aligned} \Lambda_1 : \mathbb{N}^\star &\longrightarrow \mathbb{R} \\ n_{pix} &\longmapsto \Lambda_1(n_{pix}) = n_{pix}[pixel] \times \frac{9 \cdot 10^4}{5143} \, [\mu m/pixel] \end{aligned}$$

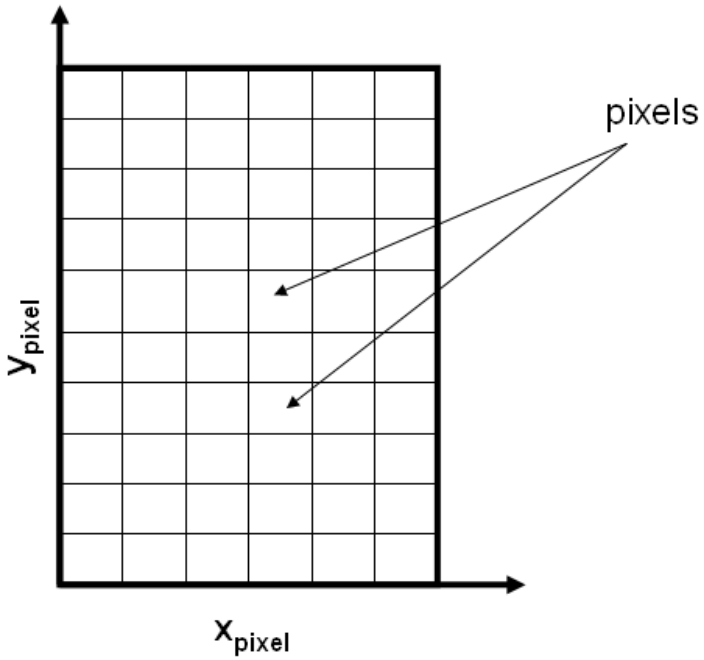

Figure 4.4: Image plate

maps the the y-axis in pixel space, $\mathbb{N}^\star$, into the y-axis in the coordinate space $\mathbb{R}$. where $\mathbb{N}^\star$ is the set of non-zero natural numbers and $\mathbb{R}$ is the set of all real numbers. $\Lambda_1(n_{pix})$ gives the coordinates in units of microns.

- Second step: transformation of coordinate into x-ray energy.

A translation of the image plate in x-direction allowed us to record up to three spectra from consecutive shots. The image plate is, then, taken out for scanning and readout. Putting a new image plate in the detector does not conserve the original position. In other words, since the exchange is not automated but done by the experimenter, there is a fluctuation from shot to shot in the position of spectra. To

correct for this fluctuations we proceeded as follows: Whenever we have spectra from other targets (Cu, Au for example) on the same image plate, we used their cold K_α line to obtain the absolute dispersion function.

The dispersion function was determined to have the following form (based on the geometry of the diagnostic):

$$\begin{aligned} \Lambda_2 : \mathbb{R} &\longrightarrow \mathbb{E} \\ y &\longmapsto \Lambda_2(y) = C_1 + C_2 \cdot y + C_3 \cdot y^2 + C_4 \cdot y^3 + C_5 \cdot y^4 + C_6 \cdot y^5 \end{aligned}$$

The constants in this expression are determined from the geometry of the HOPG and the Bragg condition, $n\lambda = 2d \cdot cos(\theta)$. All the dispersion functions for the four targets are equal to within additive constants. The correction for the fluctuation described above is embedded in the constant C_1.

As an example, the constants for the target with no Molybdenum at the front are

$$\begin{pmatrix} C_1 \\ C_2 \\ C_3 \\ C_4 \\ C_5 \\ C_6 \end{pmatrix} = \begin{pmatrix} 6.988 \\ 0.47927925 \\ 0.035731040 \\ 0.0035718845 \\ -4.7790054 \cdot 10^{-5} \\ 4.9506685 \cdot 10^{-5} \end{pmatrix}$$

The next step in the data processing is the application of corrections to the x-ray intensities. One correction is due the attenuation in the Al-Mylar filter, the other due to the photo-absorption in the material of the target (Mo and V). Both "front" and "rear" HOPG's had the same amount of filtering: 12 μm of Al just before the image plate and 12 μm of Mylar between the source and crystals, acting as a debris shielding. Tables of Transmission for photon energies of interest were imported from the center of x-ray optics website (http://www-cxro.lbl.gov/) and fitted with analytical functions which we denote by F_{Al} and F_{Mylar}. These two functions are global and can be applied to all the targets. They are given by,

$$F_{Al}(\hbar\omega) = -1.473 + 0.689 \cdot (\hbar\omega) - 0.069 \cdot (\hbar\omega)^2 + 0.0024 \cdot (\hbar\omega)^3. \tag{4.1}$$

$$F_{Mylar}(\hbar\omega) = 0.661 + 0.106 \cdot (\hbar\omega) - 0.011 \cdot (\hbar\omega)^2 + 0.0004 \cdot (\hbar\omega)^3. \tag{4.2}$$

$$F_{V}(\hbar\omega) = -0.644 + 0.419 \cdot (\hbar\omega) - 0.039 \cdot (\hbar\omega)^2 + 0.0013 \cdot (\hbar\omega)^3. \tag{4.3}$$

The correction due to the attenuation in Mo is different for different targets since the amount of Mo at the front and rear is variable. Therefore the transmission functions are thickness-dependent. If we denote these functions by $F_{Mo}(x, \hbar\omega)$, where x is the Mo thickness, then the attenuation-corrected intensity is,

$$I(x,\hbar\omega)|_{Front} = \frac{I_0}{F_{Al}(\hbar\omega)\cdot F_{Mylar}(\hbar\omega)\cdot F_{Mo}(x,\hbar\omega)} \tag{4.4}$$

$$I(x,\hbar\omega)|_{Rear} = \frac{I_0}{F_{Al}(\hbar\omega)\cdot F_{Mylar}(\hbar\omega)\cdot F_{V}(\hbar\omega)\cdot F_{Mo}(3.5-x,\hbar\omega)} \tag{4.5}$$

where I_0 is the raw intensity.

For example, the functions $F_{Mo}(x,\hbar\omega)$ for the target with $1\mu m$ at the front are given by the expressions,

$$F_{Mo}(1\mu m,\hbar\omega) = -1.199 + 0.602\cdot(\hbar\omega) - 0.0595\cdot(\hbar\omega)^2 + 0.003\cdot(\hbar\omega)^3. \tag{4.6}$$

$$F_{Mo}(2.5\mu m,\hbar\omega) = -1.434 + 0.491\cdot(\hbar\omega) - 0.035\cdot(\hbar\omega)^2 + 0.0009\cdot(\hbar\omega)^3. \tag{4.7}$$

for front and rear HOPG's respectively.

Flattening of the spectra by removing the background contributions is the next step. This is done by finding a function $F_{background}(x,\hbar\omega)$ reproducing the same background and subtracting it from the data. For the the rear HOPG and 1 μm Mo at the front of the target, the background function is,

$$F_{background}(1\mu m,\hbar\omega) = \begin{pmatrix} \hbar\omega^3 & \hbar\omega^2 & \hbar\omega \end{pmatrix} \times \begin{pmatrix} -6.256 \\ 134.545 \\ -437.196 \end{pmatrix} \tag{4.8}$$

The background corrected intensity is given by,

$$\widetilde{I}(x,\hbar\omega) = |I(x,\hbar\omega) - F_{background}(x,\hbar\omega)| \tag{4.9}$$

Note: The vanadium spectra were processed in the same way.

4.2 Experimental results

4.2.1 HOPG spectra

Vanadium spectra were seen only with the rear HOPG. These spectra showed the presence of cold K_α and K_β but no ionic lines. The absence of Vanadium thermal lines suggests that the rear side of the target is cold.

The rear HOPG showed that, for all targets, Ni K_α at 7478 eV and Ni K_β at 8265 eV are induced (Fig. 4.5). When the laser is incident directly on Ni (target with zero Mo at the front), in addition to Ni K_α and Ni K_β, the ionic lines Ni He_α at 7765 eV and Ni Ly_α at 8073 eV are induced (Fig. 4.5-a and -b). Putting a half a micron of Molybdenum at the front of the target decreases the intensity of He_α and Ly_α ionic line emission as shown in Fig. (4.5-b). When the front Mo thickness is increased to more than $1\mu m$, both He_α and Ly_α are suppressed (Fig. 4.5-(c-d)). This is an experimental evidence of hot, thin surface layer formation with a thickness of the order of a micron. If the laser energy is carried by the hots, then according to these spectra their range is much smaller than their classical range.

In order to compare the spectra obtained with front HOPG to those obtained with rear HOPG, we need to normalize all the spectra with respect to the cold K_α line. Since this line is optically thin, then its intensity from front and rear should be the same. Intensities of K_α line recorded by the rear HOPG are higher than those recorded by front HOPG by a factors of 1.1, 1.3, 1.5, and 4 for (a),(b),(c), and (d)

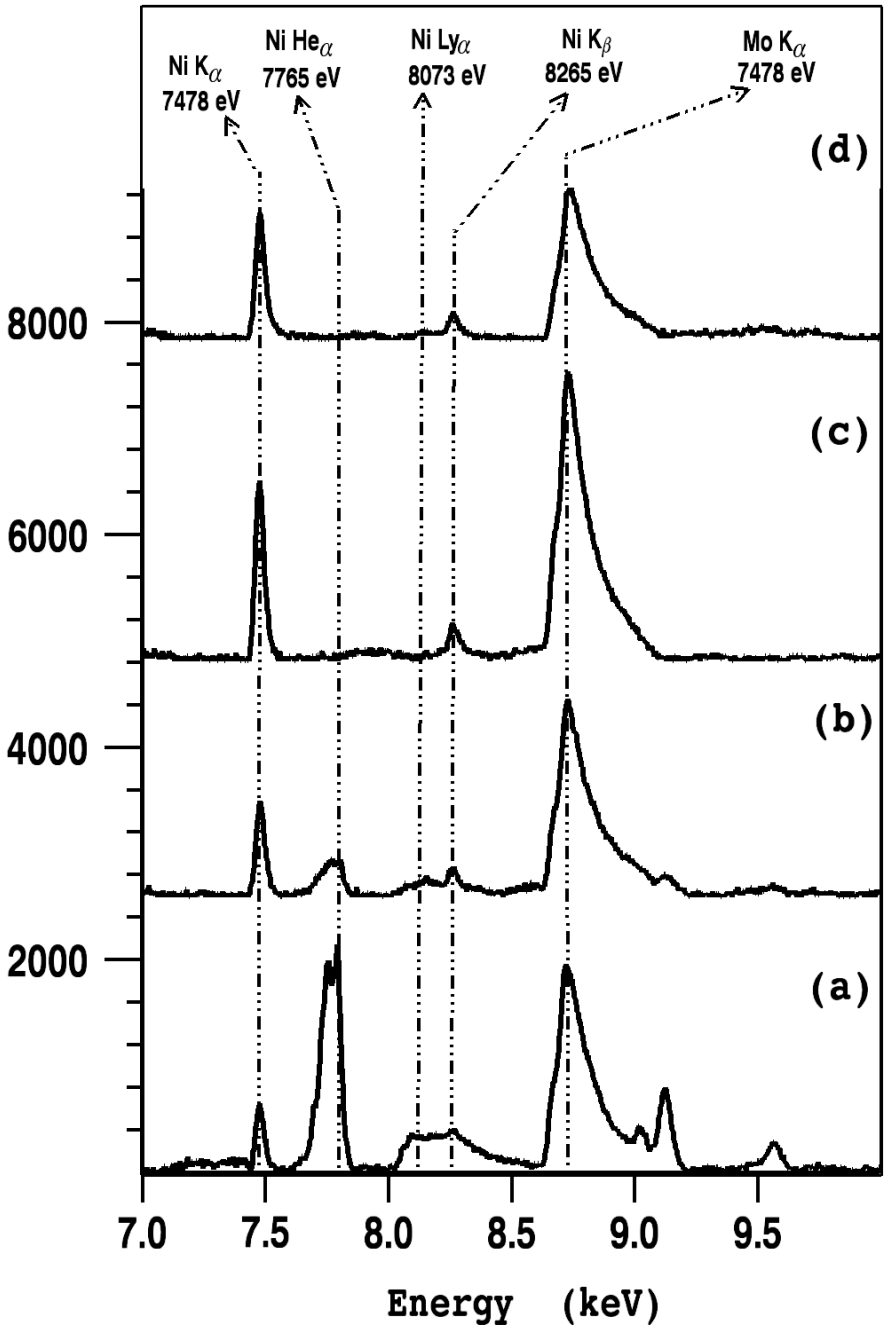

Figure 4.5: Rear HOPG spectra: (a) Ni at the front of the target. (b) Ni at depth of 0.5 μm. (b) Ni at depth of 1.0 μm. (b) Ni at depth of 2.5 μm

respectively. A plot of the logarithm of these ratios as a function of the Molybdenum difference between the front and rear exhibits a linear behavior (Fig. 4.6). This suggests the existence of an additional absorption mechanism.

We looked at inverse bremsstrahlung as a potential absorption mechanism using Johnson's and Dawson's expression, which take into account the collective effects:

$$\kappa_{ib} = 1.33 \cdot 10^{-4} \frac{\overline{Z}\left(\frac{n_e}{10^{21} cm^{-3}}\right)^2 \ln \Lambda}{\left(\frac{\hbar\omega}{keV}\right)^2 \left(\frac{T_e}{100eV}\right)^{3/2} \left(1 - \frac{\omega_p^2}{\omega^2}\right)} \cdot s^{-1} \tag{4.10}$$

The absorption was too small to explain the discrepancy. This issue is still under investigation.

4.2.2 2D spatially resolved Lymann Alpha image

We took advantage of the proximity of the cold Cu K_α line to the Ni Ly_α to obtain spatially resolved two-dimensional images of the targets. This was done using the Bragg imager described in Chapter 3. A typical image is shown in Fig. 4.7. It has a full width at half maximum of about 25 μm which is small compared to the K_α spot from Cu targets for example.

4.3 Spectroscopic modeling

The Spectroscopic Collisional-Radiative Atomic Model (SCRAM) was used to model the x-ray emission from these low mass, solid targets. By integrating a set of coupled rates equations using input data from FAC for collisional and radiative

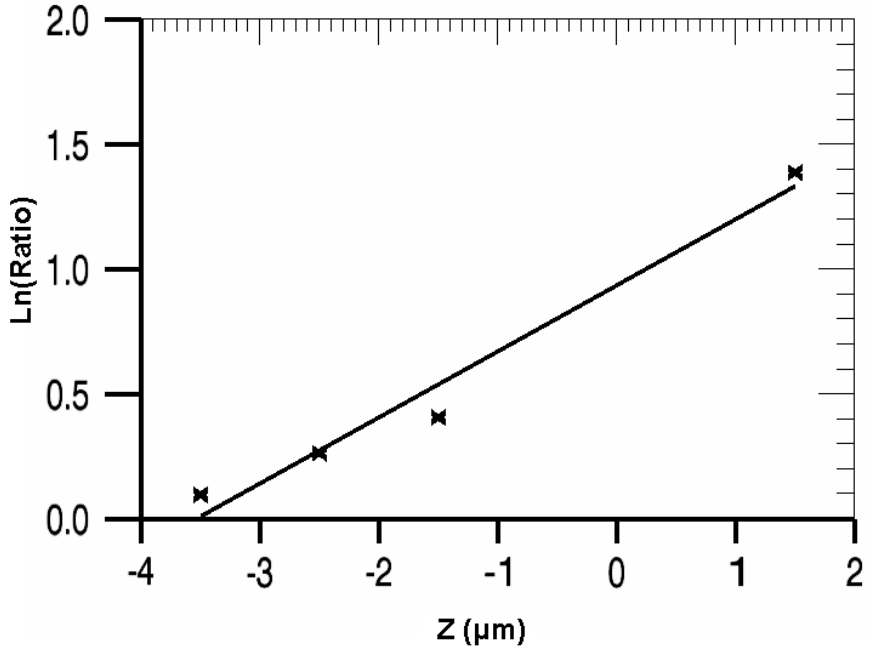

Figure 4.6: Logarithm of rear to front ratio of Ni K_α line intensity as a function of the Molybdenum difference between the front and rear of the target.

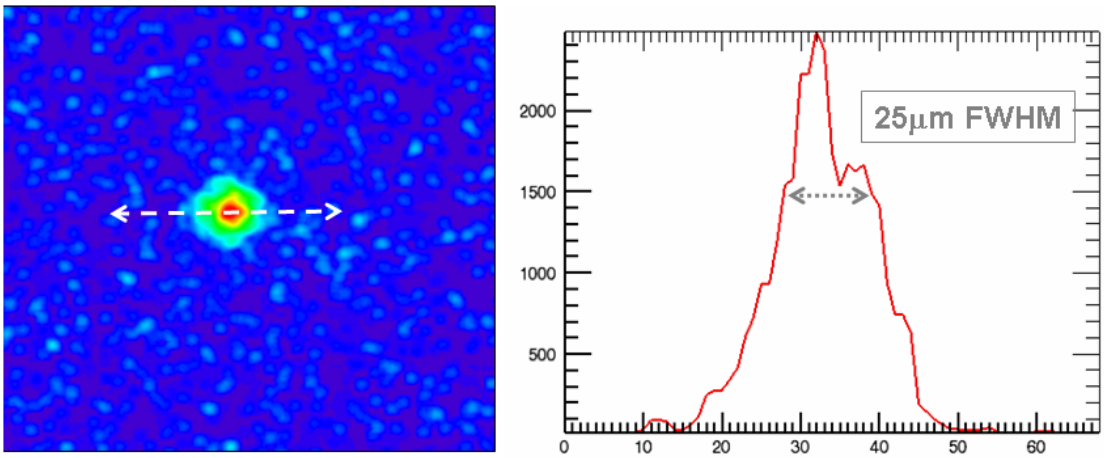

Figure 4.7: Ni Ly_α image at 8.073 Kev Of Nickel-vanadium sandwich using a Cu Crystal.

rates, SCRAM generates synthetic spectra [17]. One of the inputs specified, at the beginning of the calculation, is the hot electron density. For a laser intensity of $5 \times 10^{20}\ W/cm^2$, the conversion efficiency is close to 50% (Key et.al 1998, Wharton et al. 1998) which gives about 180 J of energy into the hots. Taking the hot electron injection area to be of the order of the K_α spot size, the hot electron density was found to be $\sim 10^{20}\ cm^{-3}$. These electrons were then given a Maxwellian distribution in energies with a temperature $T_{hot} = 1\ MeV$. The Ni target was specified with a density of $n_{ion} = 9.14 \times 10^{22}\ cm^{-3}$ and we assumed the existence of two emission regions: a heated region with a diameter φ_{hot} surrounded by a cold region with a diameter φ_{cold}. We also assumed steady state populations, optically thin Ni, and no expansion at the front of the target. The generated spectra were then post-processed to account for instrument broadening by taking $E/\Delta E = 220$.

Fig. 4.8 - 4.11 show the modelled spectra for the targets where the Ni is located at a depth of 0.0 μm, 0.5 μm, 1.0 μm, and 2.5 μm respectively. These spectra are in a good agreement with the experimental data confirming the existence of axial temperature gradients. For the first target, Ly_α to He_α intensity ratio gives a maximum temperature of $T_{max} \sim 6\ keV$ at the front surface of the target, while He_α to K_α intensity ratio puts $\varphi_{cold}/\varphi_{hot}$ at 10 (consistent with the Ly_α image). The temperature decay slope was determined from the He_α to K_α intensity ratio of the second target (when the Ni was at a depth of a 0.5 μm) and found to be $10^{-0.1}$ per 0.1 μm of depth (Fig. 4.12).

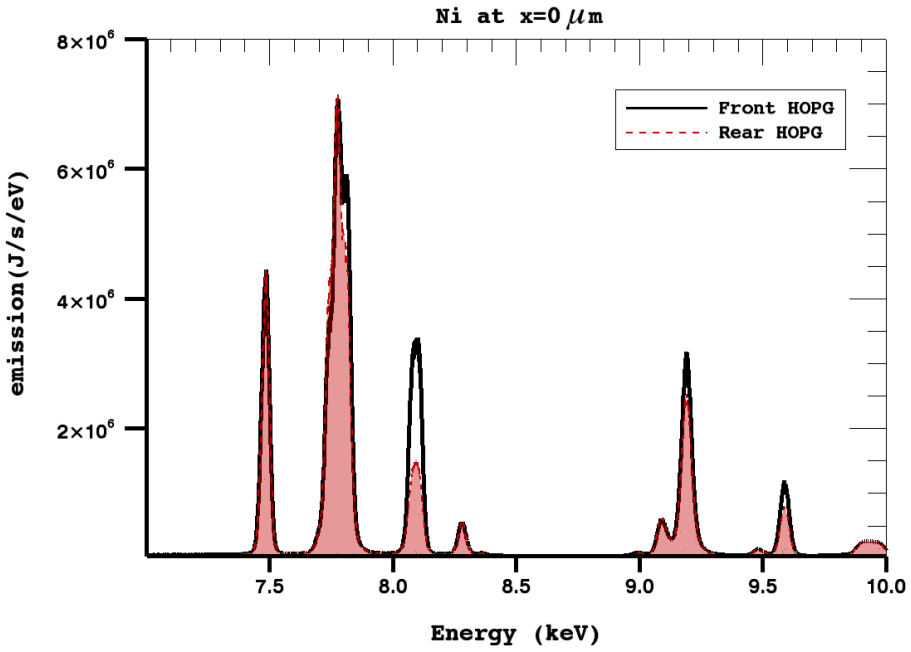

Figure 4.8: SCRAM generated synthetic spectra for Ni at depth of 0.0 μm. Black, the front HOPG, Red, the rear HOPG

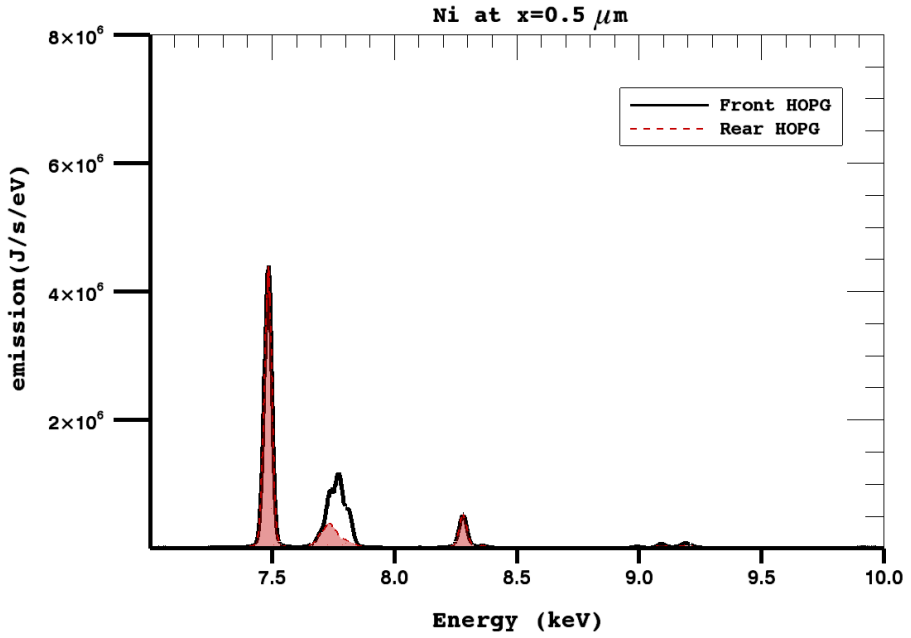

Figure 4.9: SCRAM generated synthetic spectra for Ni at depth of 0.5 μm. Black, the front HOPG, Red, the rear HOPG

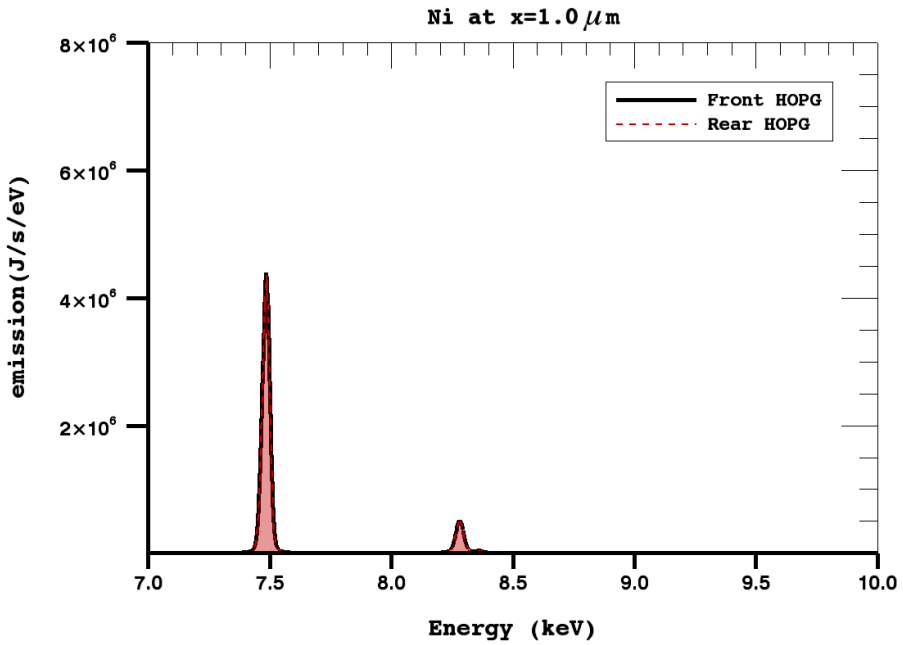

Figure 4.10: SCRAM generated synthetic spectra for Ni at depth of 1.0 μm. Black, the front HOPG, Red, the rear HOPG

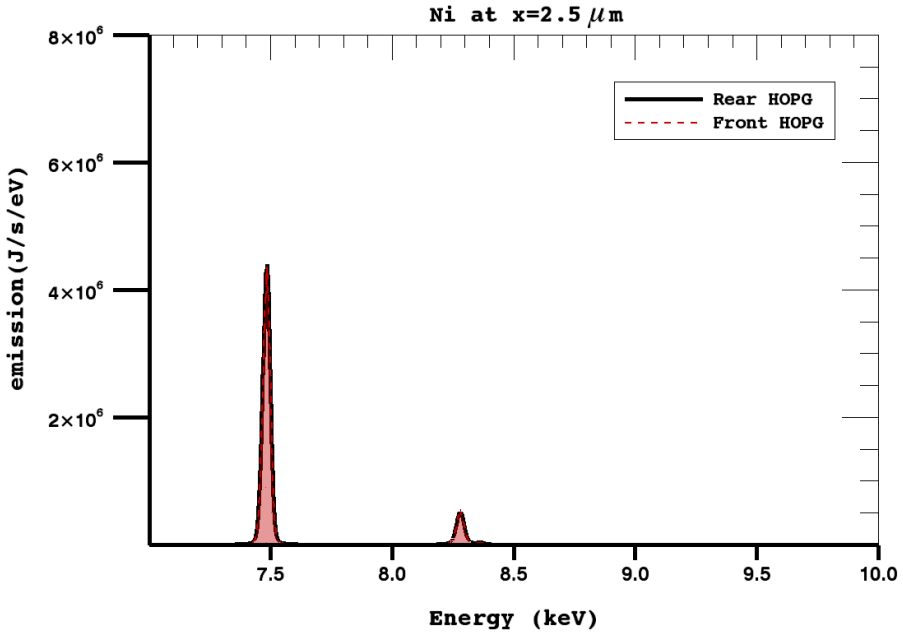

Figure 4.11: SCRAM generated synthetic spectra for Ni at depth of 2.5 μm. Black, the front HOPG, Red, the rear HOPG

Using the same temperature profile and the same cold to hot region ratio, the opacity effects were tested. The opacity did not have a significant effect on K_α and K_β emission intensities but the effect was significant for the He_α and Ly_α lines. Moreover, The emission is more attenuated for rear HOPG than for front HOPG. This is due to the attenuation of the emission, generated at the front of the target, in the cold material of the rear where ground state populations are larger.

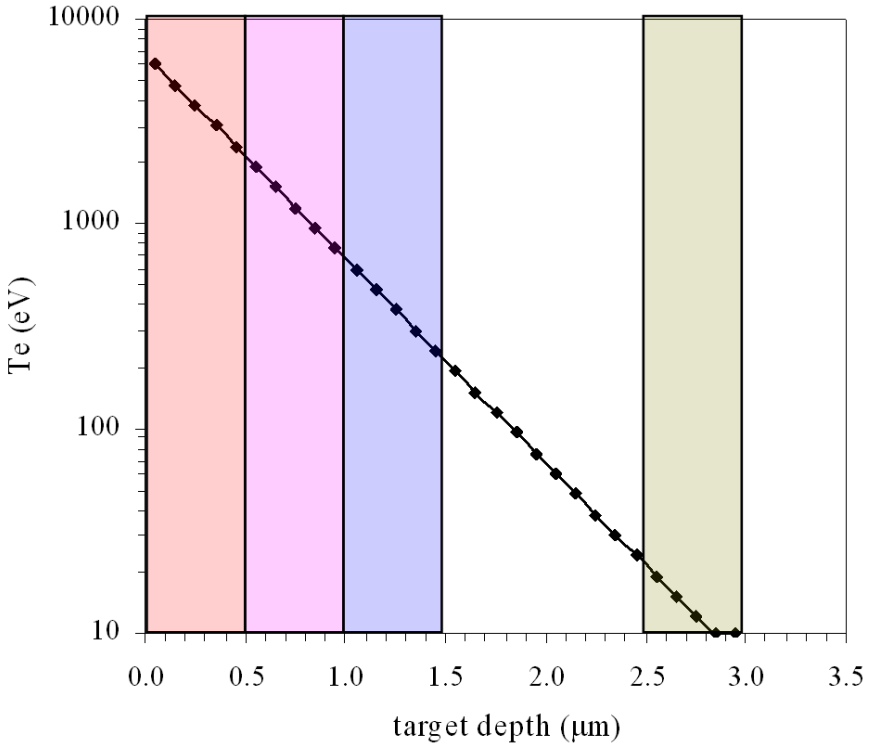

Figure 4.12: Temperature profile of the target. $T_{max} \sim 6\ keV$ at the front surface. $10^{-0.1}$ per 0.1 μm slope.

4.4 PIC modeling

Two-dimensional particle-in-cell (PIC) simulations were carried out by Andreas Kemp (LLNL) in collaboration with Hartmut Ruhl. The code has the capability to run in a kinetic mode (no collisions) or collisional mode (collisions included). The laser pulse impinging on the target was p-polarized, had a wavelength of $\lambda = 1\ \ \mu m$, and a focal spot size of the order of 5λ. Its intensity was $\sim 5 \times 10^{20}\ W/cm^2$ which corresponds to a normalized vector potential $a = eA/mc^2$ of 20. The geometry of the problem was specified in cartesian coordinates with the z-direction as the longitudinal direction (direction of laser propagation) and the y-direction as the transverse direction. The target was modelled as a uniform slab of 60 μm lateral dimension and a thickness of 5 μm. It extends from $z = 7.5\ \mu m$ to $z = 12.5\ \mu m$, and it is surrounded by a vacuum as shown in Fig. 4.13. The uniform plasma consists of ions with a density of $n_{ion} = 4 \times 10^{22}\ cm^{-3}$ which corresponds to $\sim 40\ n_{cr}$ and electrons with a density $\sim 200\ n_{cr}$.

The effect of collisions on the electron energy transport were studied by running the code with and without collisions. In the absence of collisions, electron beam filaments are observed. These filaments start at the front surface, extend in the longitudinal direction, and reach the back surface of the target (see the plot of azimuthal magnetic field in Fig. 4.13-top). This is consistent with Ruhl's results at much lower laser intensities of $\sim\ 10^{19}\ W/cm^2$ (IFSA 2005). In the presence of collisions, these filaments are suppressed as shown in Fig. 4.13 (bottom). The plotted quantity in

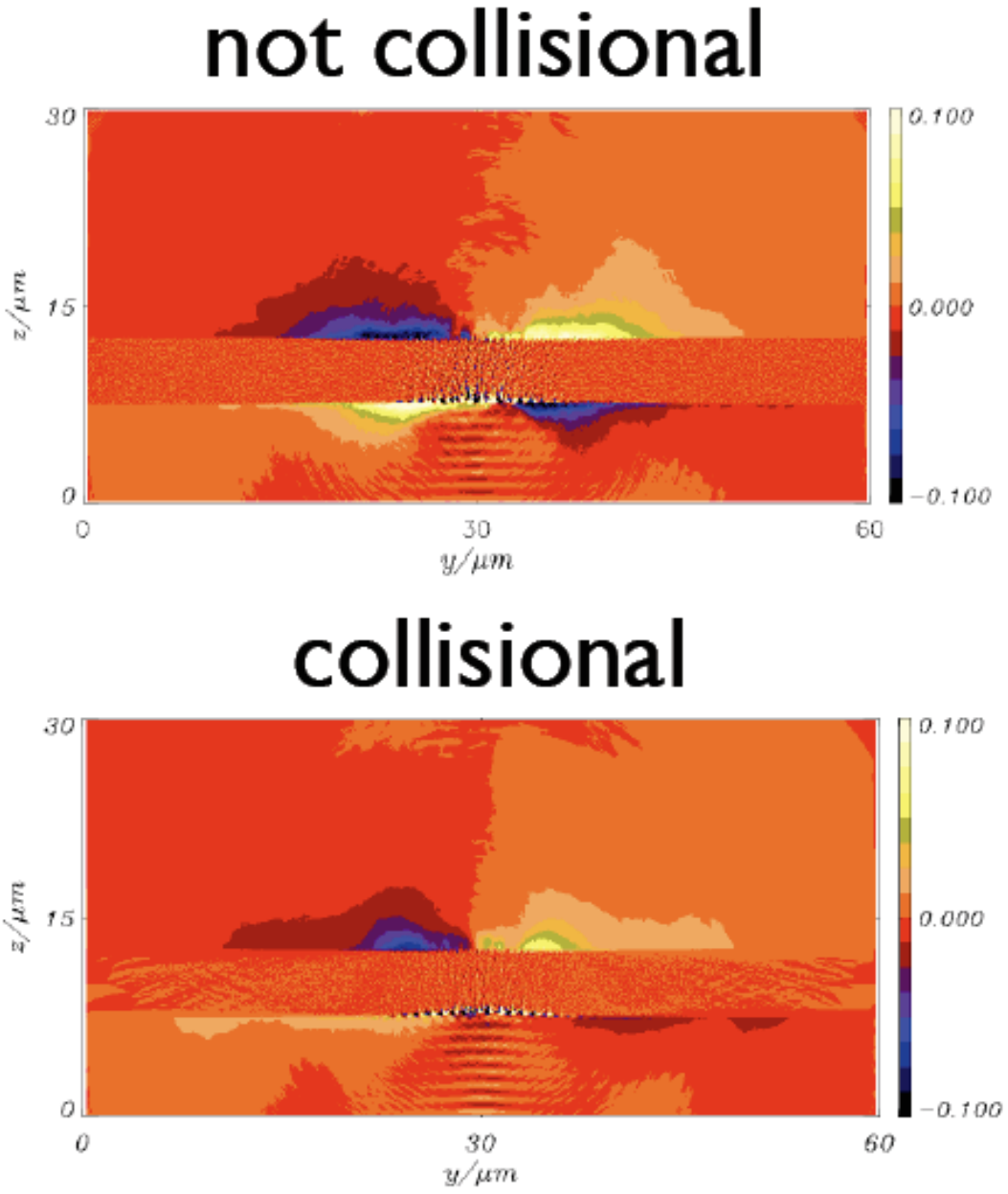

Figure 4.13: Magnetic field

Fig. 4.13 is the azimuthal magnetic field time-averaged over 2 laser cycles.

The energy density in the target is shown in Fig. 4.14 (Top). The energy density is higher at the vicinity of the target surface and in the neighborhood of the laser focal spot. It is also evident from Fig. 4.14 (bottom) that the energy is confined to a surface layer with a thickness of the order of 1 micron.

In summary, We have presented the first experimental evidence of temperature gradients and hot surface layer formation at laser intensities of $\sim 5 \times 10^{20}\ W/cm^2$. The spectroscopic modeling of Ni x-ray spectra shows that the experimental data can be reproduced with a decaying temperature profile. With opacities taken into account, the maximum temperature at the front surface of the target was determined to be $\sim\ 5\ keV$. Then, it decreased with depth at a rate of $10^{-0.1}$ per 0.1 μm. Two-dimensional particle-in-cell (PIC) simulations confirm the formation of this hot surface layer. The (PIC) simulations are in the early stage and more work needs to be done to answer the following questions: how much energy is confined near the surface? how hot does this surface layer gets? what is the mechanism responsible of energy trapping near the surface? The results of further investigations will be submitted for publication in a scientific journal (Physical Review Letters for example).

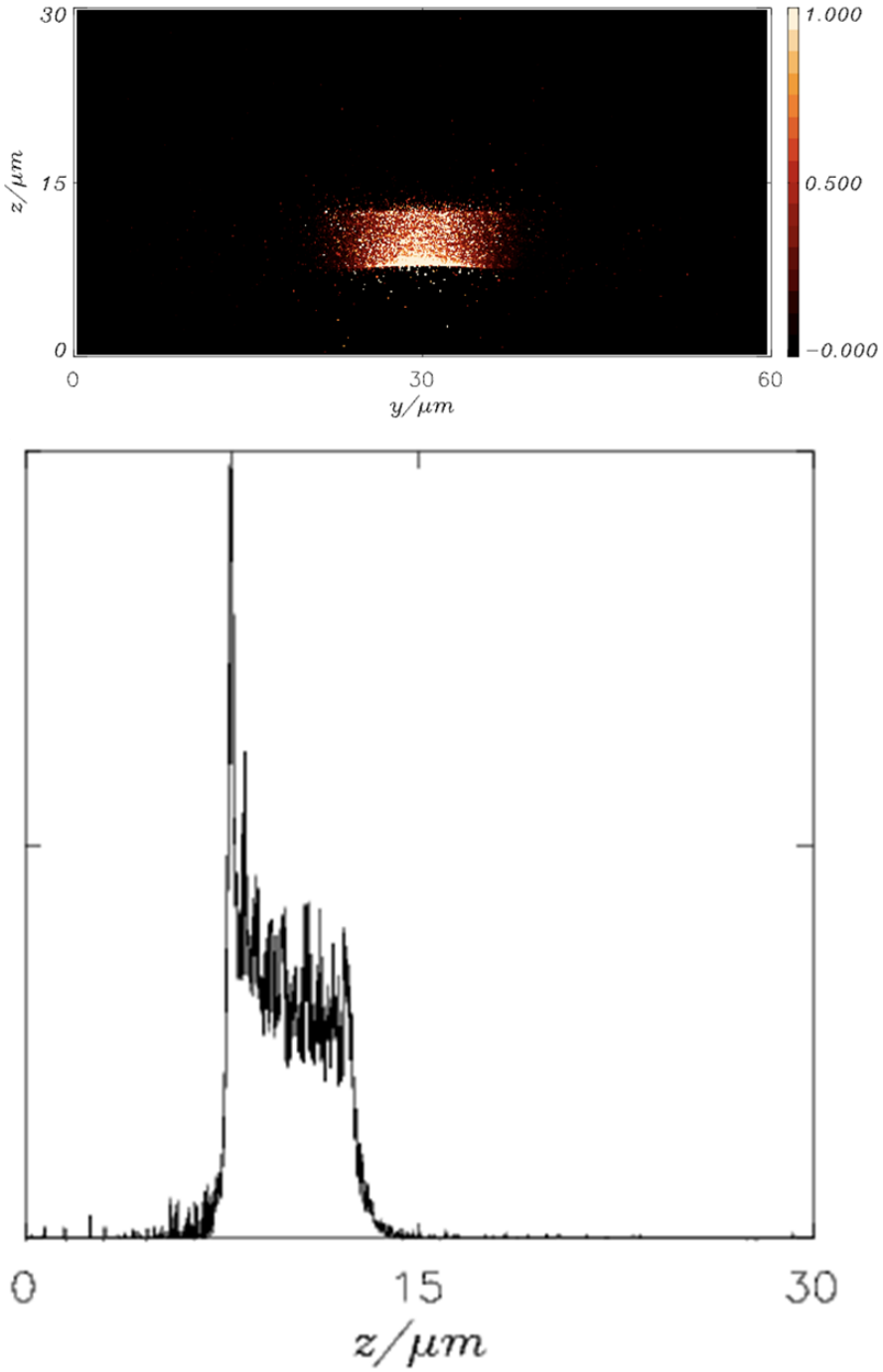

Figure 4.14: Energy density

Acknowledgements *I would like to thank Stephanie Hansen for the spectroscopic modeling of these targets and Andreas Kemp for carrying out the PIC simulations.*

Bibliography

[1] Energy Information Administration http://www.eia.doe.gov.

[2] Francis William Aston. *Engineering*, 96:423, 1913.

[3] G. McCracken and P. Stott. *Fusion The energy of the universe.* 2005.

[4] C. F. Von Weizscker. *Z. Physik volume = 96, number = 431,*, 1935.

[5] K. Mukhin. *Experimental nuclear physics.* 1983.

[6] V. Lukyanov and N. Kovalskii. *Hot plasma and controlled nuclear fusion.* 1997.

[7] G. Velarde, Y. Ronen, and J. Martinez-Val. *Nuclear fusion by Inertial Confinement: A comprehensive treatise.*

[8] S. Glastone and R. Lovberg. *Controlled thermonuclear fusion.* 1960.

[9] J. D. Lawson. Some criteria for a useful thermonuclear reactor. *Proc. Phys. Soc. London*, B70:6, 1957.

[10] Mordecai D. Rosen. The physics issues that determine inertial confinement fusion target gain and driver requirements: A tutorial. volume 6, pages 1690–1699, 1999.

[11] Max Tabak et al. *Physics of Plasmas*, 1(5):1626–1634, 1994.

[12] M. H. Key. Fast ignition: Physics progress in the us fusion energy program and prospects for achieving ignition. *UCRL-JC-147370*, 2002.

[13] Hannes Alfven. On the motion of cosmic rays in interstellar space. *Physical Review*, 55(5):425–429, 1939.

[14] E. S. Weibel. Spontaneously Growing Transverse Waves in a Plasma Due to an Anisotropic Velocity Distribution. *Physical Review Letters*, 2:83–84, February 1959.

[15] Jeremy Martin Hill, Michael H. Key, Stephen P. Hatchett, and Richard R. Freeman. Beam-weibel filamentation instability in near-term and fast-ignition experiments. *Physics of Plasmas*, 12(8):082304, 2005.

[16] C. Deutsch, A. Bret, M.-C. Firpo, and P. Fromy. Interplay of collisions with quasilinear growth rates of relativistic electron-beam-driven instabilities in a superdense plasma. *pre*, 72(2), August 2005.

[17] M. Honda, J. Meyer-Ter-Vehn, and A. Pukhov. Two-dimensional particle-in-cell

simulation for magnetized transport of ultra-high relativistic currents in plasma. *Physics of Plasmas*, 7:1302–1308, April 2000.

[18] A. Pukhov and J. Meyer ter Vehn. Laser hole boring into overdense plasma and relativistic electron currents for fast ignition of icf targets. *Physical Review Letters*, 79(14):2686–2689, 1997.

[19] Y. Sentoku, K. Mima, P. Kaw, and K. Nishikawa. Anomalous Resistivity Resulting from MeV-Electron Transport in Overdense Plasma. *Physical Review Letters*, 90(15), April 2003.

[20] J. A. Koch, M. H. Key, R. R. Freeman, S. P. Hatchett, R. W. Lee, D. Pennington, R. B. Stephens, and M. Tabak. Experimental measurements of deep directional columnar heating by laser-generated relativistic electrons at near-solid density. *Physical Review E (Statistical, Nonlinear, and Soft Matter Physics)*, 65(1):016410, 2001.

[21] H. M. Milchberg, R. R. Freeman, S. C. Davey, and R. M. More. Resistivity of a simple metal from room temperature to 10 to the 6th K. *Physical Review Letters*, 61:2364–2367, November 1988.

[22] Stefano Atzeni et al. *Physics of Plasmas*, 6(8):3316–3326, 1999.

[23] M. Tabak, D. S. Clark, S. P. Hatchett, M. H. Key, B. F. Lasinski, R. A. Snavely, S. C. Wilks, R. P. J. Town, R. Stephens, E. M. Campbell, R. Kodama, K. Mima,

K. A. Tanaka, S. Atzeni, and R. Freeman. Review of progress in fast ignition. *Physics of Plasmas*, 12(5):057305, 2005.

[24] M. H. Key, M. D. Cable, T. E. Cowan, K. G. Estabrook, B. A. Hammel, S. P. Hatchett, E. A. Henry, D. E. Hinkel, J. D. Kilkenny, J. A. Koch, W. L. Kruer, A. B. Langdon, B. F. Lasinski, R. W. Lee, B. J. MacGowan, A. MacKinnon, J. D. Moody, M. J. Moran, A. A. Offenberger, D. M. Pennington, M. D. Perry, T. J. Phillips, T. C. Sangster, M. S. Singh, M. A. Stoyer, M. Tabak, G. L. Tietbohl, M. Tsukamoto, K. Wharton, and S. C. Wilks. Hot electron production and heating by hot electrons in fast ignitor research. *Physics of Plasmas*, 5(5):1966–1972, 1998.

[25] K. Yasuike, M. H. Key, S. P. Hatchett, R. A. Snavely, and K. B. Wharton. volume 72, pages 1236–1240, 2001.

[26] C. K. Li and R. D. Petrasso. Energy deposition of mev electrons in compressed targets of fast-ignition inertial confinement fusion. *Physics of Plasmas*, 13(5):056314, 2006.

[27] Michael H. Key. Fast ignition relevant study of the flux of high intensity laser generated electrons via a hollow cone into a laser-imploded plasma. *Phys. Rev. Lett.*

[28] C. Deutsch and P. Fromy. Correlated stopping of relativistic electrons in superdense plasmas. *Physics of Plasmas*, 6(9):3597–3606, 1999.

[29] K. B. Wharton, S. P. Hatchett, S. C. Wilks, M. H. Key, J. D. Moody, V. Yanovsky, A. A. Offenberger, B. A. Hammel, M. D. Perry, and C. Joshi. Experimental measurements of hot electrons generated by ultraintense ([greater-than] 10[sup 19] w/cm[sup 2]) laser-plasma interactions on solid-density targets. *Physical Review Letters*, 81(4):822–825, 1998.

[30] J. J. Santos, F. Amiranoff, S. D. Baton, L. Gremillet, M. Koenig, E. Martinolli, M. Rabec Le Gloahec, C. Rousseaux, D. Batani, A. Bernardinello, G. Greison, and T. Hall. Fast electron transport in ultraintense laser pulse interaction with solid targets by rear-side self-radiation diagnostics. *Physical Review Letters*, 89(2):025001, 2002.

[31] Laurent Gremillet, Guy Bonnaud, and Francois Amiranoff. Filamented transport of laser-generated relativistic electrons penetrating a solid target. *Physics of Plasmas*, 9(3):941–948, 2002.

[32] S. D. Baton, J. J. Santos, F. Amiranoff, H. Popescu, L. Gremillet, M. Koenig, E. Martinolli, O. Guilbaud, C. Rousseaux, M. Rabec Le Gloahec, T. Hall, D. Batani, E. Perelli, F. Scianitti, and T. E. Cowan. Evidence of ultrashort electron bunches in laser-plasma interactions at relativistic intensities. *Physical Review Letters*, 91(10):105001, 2003.

[33] R. B. Stephens, R. A. Snavely, Y. Aglitskiy, F. Amiranoff, C. Andersen, D. Batani, S. D. Baton, T. Cowan, R. R. Freeman, T. Hall, S. P. Hatchett,

J. M. Hill, M. H. Key, J. A. King, J. A. Koch, M. Koenig, A. J. MacKinnon, K. L. Lancaster, E. Martinolli, P. Norreys, E. Perelli-Cippo, M. Rabec Le Gloahec, C. Rousseaux, J. J. Santos, and F. Scianitti. *Physical Review E (Statistical, Nonlinear, and Soft Matter Physics)*, 69(6):066414, 2004.

[34] E. Martinolli, M. Koenig, F. Amiranoff, S. D. Baton, L. Gremillet, J. J. Santos, T. A. Hall, M. Rabec-Le-Gloahec, C. Rousseaux, and D. Batani. Fast electron heating of a solid target in ultrahigh-intensity laser pulse interaction. *Physical Review E (Statistical, Nonlinear, and Soft Matter Physics)*, 70(5):055402, 2004.

[35] D. Batani, S. D. Baton, M. Manclossi, J. J. Santos, F. Amiranoff, M. Koenig, E. Martinolli, A. Antonicci, C. Rousseaux, M. Rabec Le Gloahec, T. Hall, V. Malka, T. E. Cowan, J. King, R. R. Freeman, M. Key, and R. Stephens. Ultraintense laser-produced fast-electron propagation in gas jets. *Physical Review Letters*, 94(5):055004, 2005.

[36] R. R. Freeman. Transport of Huge Currents of Charged Particles for Fast Ignition Applications. *APS Meeting Abstracts*, pages 1004–+, October 2005.

[37] R. Kodama and et al. Nuclear fusion:fast heating scalable to laser fusion ignition. *Nature*, 418:933–934, 2002.

[38] K. A. Tanaka, R. Kodama, K. Mima, Y. Kitagawa, H. Fujita, N. Miyanaga, K. Nagai, T. Norimatsu, T. Sato, Y. Sentoku, K. Shigemori, A. Sunahara, T. Shozaki, M. Tanpo, S. Tohyama, T. Yabuuchi, J. Zheng, T. Yamanaka, P. A.

Norreys, R. Evanse, M. Zepf, K. Krushelnic, A. Dangor, R. Stephens, S. Hatchett, M. Tabak, and R. Turner. Basic and integrated studies for fast ignition. *Physics of Plasmas*, 10(5):1925–1930, 2003.

[39] P. A. Norreys, K. L. Lancaster, C. D. Murphy, H. Habara, S. Karsch, R. J. Clarke, J. Collier, R. Heathcote, C. Hemandez-Gomez, S. Hawkes, D. Neely, M. H. R. Hutchinson, R. G. Evans, M. Borghesi, L. Romagnani, M. Zepf, K. Akli, J. A. King, B. Zhang, R. R. Freeman, A. J. MacKinnon, S. P. Hatchett, P. Patel, R. Snavely, M. H. Key, A. Nikroo, R. Stephens, C. Stoeckl, K. A. Tanaka, T. Norimatsu, Y. Toyama, and R. Kodama. Integrated implosion/heating studies for advanced fast ignition. *Physics of Plasmas*, 11(5):2746–2753, 2004.

[40] S. Hatchett, M. Herrmann, M. Tabak, R. Turner, and R. Stephens. New Developments in Cone-Focussed Fast Ignition. *APS Meeting Abstracts*, pages 1086P–+, October 2001.

[41] P. A. Norreys, R. Allott, R. J. Clarke, J. Collier, D. Neely, S. J. Rose, M. Zepf, M. Santala, A. R. Bell, K. Krushelnick, A. E. Dangor, N. C. Woolsey, R. G. Evans, H. Habara, T. Norimatsu, and R. Kodama. Experimental studies of the advanced fast ignitor scheme. *Physics of Plasmas*, 7(9):3721–3726, 2000.

[42] R. Kodama and et al. Fast heating of ultrahigh-density plasma as a step towards laser fusion ignition. *Nature*, 412:798–802, 2001.

[43] C. Stoeckl. *Rev. Sci. Instrum*, 75:3705, 2004.

[44] J. A. King, K. Akli, B. Zhang, R. R. Freeman, M. H. Key, C. D. Chen, S. P. Hatchett, J. A. Koch, A. J. MacKinnon, P. K. Patel, R. Snavely, R. P. J. Town, M. Borghesi, L. Romagnani, M. Zepf, T. Cowan, H. Habara, R. Kodama, Y. Toyama, S. Karsch, K. Lancaster, C. Murphy, P. Norreys, R. Stephens, and C. Stoeckl. Ti k alpha radiography of cu-doped plastic microshell implosions via spherically bent crystal imaging. *Applied Physics Letters*, 86(19):191501, 2005.

[45] A. J. Mackinnon, P. K. Patel, M. Borghesi, R. C. Clarke, R. R. Freeman, H. Habara, S. P. Hatchett, D. Hey, D. G. Hicks, S. Kar, M. H. Key, J. A. King, K. Lancaster, D. Neely, A. Nikkro, P. A. Norreys, M. M. Notley, T. W. Phillips, L. Romagnani, R. A. Snavely, R. B. Stephens, and R. P. J. Town. Proton radiography of a laser-driven implosion. *Physical Review Letters*, 97(4):045001, 2006.

[46] C. N. Danson, S. Angood, L. J. Barzanti, N. Bradwell, J. Collier, A. R. Damerell, C. B. Edwards, C. Johnson, M. H. Key, D. Neely, M. Nightingale, P. A. Norreys, D. A. Pepler, D. A. Rodkiss, I. N. Ross, P. Ryves, N. Thompson, M. Trentelman, F. N. Walsh, E. Wolfrum, and R. W. Wyatt. Design and characterization of the VULCAN Nd:glass laser to give focused intensities of 1019 Wcm-2. In M. L. Andre, editor, *Proc. SPIE Vol. 3047, p. 505-515, Solid State Lasers for Application to Inertial Confinement Fusion: Second Annual International Conference, Michel L. Andre; Ed.*, pages 505–515, December 1997.

[47] W. Theobald, K. Akli, R. Clarke, J. A. Delettrez, R. R. Freeman, S. Glenzer, J. Green, G. Gregori, R. Heathcote, N. Izumi, J. A. King, J. A. Koch, J. Kuba, K. Lancaster, A. J. MacKinnon, M. Key, C. Mileham, J. Myatt, D. Neely, P. A. Norreys, H.-S. Park, J. Pasley, P. Patel, S. P. Regan, H. Sawada, R. Shepherd, R. Snavely, R. B. Stephens, C. Stoeckl, M. Storm, B. Zhang, and T. C. Sangster. *Physics of Plasmas*, 13(4):043102, 2006.

[48] J. A. King. *Titanium K-alpha xray imaging radiography of imploding microshells using a spherically bent crystal*. PhD thesis, University of California Davis, 2006.

[49] H.-S. Park, D. M. Chambers, H.-K. Chung, R. J. Clarke, R. Eagleton, E. Giraldez, T. Goldsack, R. Heathcote, N. Izumi, M. H. Key, J. A. King, J. A. Koch, O. L. Landen, A. Nikroo, P. K. Patel, D. F. Price, B. A. Remington, H. F. Robey, R. A. Snavely, D. A. Steinman, R. B. Stephens, C. Stoeckl, M. Storm, M. Tabak, W. Theobald, R. P. J. Town, J. E. Wickersham, and B. B. Zhang. High-energy k alpha radiography using high-intensity, short-pulse lasers. *Physics of Plasmas*, 13(5):056309, 2006.

[50] E. G. Gamaly and et. al. Ablation of solids by femtosecond lasers: Ablation mechanism and ablation thresholds for metals and dielectrics. *Physics of Plasmas*, 9(3):949–957, 2002.

[51] A. R. Bell. *Plasma Phys. Controlled Fusion*, 39:653, 1997.

[52] D. J. Bond. *Phys. Rev. Lett*, 42:252, 1980.

[53] S. C. Wilks, W. L. Kruer, M. Tabak, and A. B. Langdon. *Physical Review Letters*, 69:1383–1386, August 1992.

[54] evans. *The atomic nucleus*.

[55] Francis F. Chen. *Plasma physics and controlled fusion*.

[56] H. Deutsch, K. Becker, B. Gstir, and T. D. Mrk. Calculated electron impact cross sections for the k-shell ionization of fe, co, mn, ti, zn, nb, and mo atoms using the dm formalism. *International Journal of Mass Spectrometry*, 213:5, 2002.

[57] J. P. Desclaux. *Atom. Data Nucl. Data Tables*, 12:325, 1973.

[58] C. K. Li and R. D. Petrasso. Stopping of directed energetic electrons in high-temperature hydrogenic plasmas. *Physical Review E (Statistical, Nonlinear, and Soft Matter Physics)*, 70(6):067401, 2004.

[59] C. K. Li and R. D. Petrasso. Stopping, straggling, and blooming of directed energetic electrons in hydrogenic and arbitrary-z plasmas. *Physical Review E (Statistical, Nonlinear, and Soft Matter Physics)*, 73(1):016402, 2006.

[60] J. A. King et al. *Rev. Sci. Instrum*, 76(7):076102, 2005.

[61] Sinars et al. *Rev. Sci. Instrum*, 74:2202, 2003.

[62] J. A. Aglitsky. *Phys. Rev. Lett*, 87:265001, 2001.

[63] M. H. Key. *Inertial Fusion Sciences and Applications (IFSA)*, 2003.

[64] G. Gregori and S. B. Hansen. *Contrib. Plasma Phys*, 45:284, 2005.

[65] D. Strickland and J. Mourou. *Opt. Commun*, 56:219, 1985.

[66] J. A. Koch, Y. Aglitskiy, C. Brown, T. Cowan, R. Freeman, S. Hatchett, G. Holland, M. Key, A. MacKinnon, J. Seely, R. Snavely, and R. Stephens. *Rev. Sci. Instrum*, 74(3):2130–2135, 2003.

[67] D. A. Schwartz. *Proc. SPIE*, 184:247, 1979.

[68] K. Yasuike. *Rev. Sci. Instrum*, 72:1236, 2001.

[69] M. H. Chen. *Phys. Rev. A*, 31:556, 1985.

[70] S. B. Hansen. *Private communication*, 2006.

[71] M. F. Gu. *AIP Conference Proceedings*, 730:127, 2004.

[72] H. K. Chung. *High Energy Density Physics (HEDP)*, 1:3, 2005.

[73] S. B. Hansen. PhD thesis, University of Nevada, Reno, 2003.

[74] K. N. Huang. *At. Data and Nucl. Data Table*, 18:243, 1976.

[75] F. N. Beg, A. R. Bell, A. E. Dangor, C. N. Danson, A. P. Fews, M. E. Glinsky, B. A. Hammel, P. Lee, P. A. Norreys, and M. Tatarakis. A study of picosecond laser–solid interactions up to 10[sup 19] w cm[sup - 2]. *Physics of Plasmas*, 4(2):447–457, 1997.

[76] GE Advanced Ceramics http://www.advceramics.com.

Appendix A

Manuscript submitted to Physics of Plasmas.

Temperature sensitivity of Cu K_α imaging efficiency using a spherical Bragg reflecting crystal

K. U. Akli[1,2], M. H. Key[1], H. K. Chung[1], S. B. Hansen[1],
R. R. Freeman[2,3], M. H. Chen[1], G. Gregori[4], S. Hatchett[1], D. Hey[1,2], N. Izumi[1],
J. King[1,2], J. Kuba[7], P. Norreys[4], A. J. Mackinnon[1], C. D. Murphy[4], R. Snavely[1],
R. B. Stephens[6], C. Stoeckel[5], W. Theobald[5], B. Zhang[2].

[1]Lawrence Livermore National Laboratory, Livermore, USA
[2]Department of Applied Sciences, University of CA, Davis, Davis, USA
[3]The Ohio State University, Columbus, Ohio, USA
[4]Central Laser Facility, CCLRC Rutherford Appleton Laboratory, UK
[5]University of Rochester, Laboratory for Laser Energetics, Rochester, USA
[6]General Atomics, San Diego, USA
[7]Czech Technical University, Prague, Czech Republic

abstract

The Vulcan laser facility at the Rutherford Appleton Laboratory was used to study the interaction of a 75 J 10 ps, high intensity laser beam with low-mass, solid Cu targets. Two instruments were fielded as diagnostics of the Cu K-shell emission from the targets: A single photon counting CCD spectrometer provided the absolute K_α yield and a spherically bent Bragg crystal recorded 2D monochromatic images

with a spatial resolution of 10 μm. Due to the shifting and broadening of the K_α spectral lines with increasing temperature, there is a temperature dependence of the crystal collection efficiency. This provides a temperature diagnostic when cross calibrated against a single hit CCD spectrometer, and it affects measurements of the spatial pattern of electron transport. The experimental data showing changing collection efficiency are presented. The results are discussed in light of modeling of the temperature-dependent spectrum of Cu K-shell emission.

PACS numbers: 52.38.-r, 52.38.Ph, 52.50.Jm, 52.25.Jm

A.1 Introduction

The advent of short-pulse laser technology has made it possible to create and explore isochorically heated high energy density matter. With this comes the need for diagnostics to unravel the fundamental physics of these transient plasmas. As plasma diagnostics, spherically bent Bragg crystals have been used in a back-lighter configuration to study the dynamics of laser imploded targets [1], wire-array Z-pinch implosions [2], and ablative Richtmyer-Meshkov instability [3]. They have been used also as diagnostics in the context of fast ignition [4] to get insight into short-pulse, high-intensity laser generated electron transport and the associated isochoric heating of the targets [5]. For example, Stephens et al. [6] used a spherically bent Bragg crystal coupled with a CCD to obtain monochromatic spatially resolved 2D images of planar targets with buried Ti or Cu fluor layers. Due to the shifting and broadening

of the K_α emission line with temperature [7], care must be taken in interpreting the results, especially when dealing with low mass targets and high laser energies which produce high temperatures. In this paper, we describe a temperature-dependent K_α diagnostic, present the experimental evidence of changing collection efficiency, and discuss it in light of modeling of the temperature dependent Cu K-shell emission.

A.2 Experimental setup

The short-pulse, high intensity beam of Vulcan laser facility at the Rutherford Appleton Laboratory was used to irradiate planar solid Cu foils. This infrared (1.053 μm) laser pulse was generated using the Chirped Pulse Amplification (CPA) technique [8] and contained 75 J of energy delivered in 10 ps. A peak intensity of $\sim 5 \times 10^{18}\ W/cm^2$ was achieved by using an f/3 off-axis parabola to focus the beam to a 10 μm focal spot. About 50% of the laser energy on target was contained in the central spot, the remaining energy is distributed over the wings. The spontaneous stimulated emission (ASE) contrast ratio was 10^{-7} in intensity and 10^{-4} in energy. The targets were planar solid Cu foils of 100 μm x 100 μm and 500 μm x 500 μm lateral dimensions and of varying thicknesses (1 μm to 30 μm). X-rays emitted following K-shell ionization by hot electrons were collected using the following two instruments.

A.2.1 Spherically bent Bragg imager

The first instrument is a monochromatic K_α imager, which consists of a spherically bent Bragg crystal coupled to a charge-coupled device (CCD). A Silicon dioxide crystal with a 38 cm radius of curvature, 3.082 $\mathring{A}$ 2d lattice spacing, and 2131 Miller indices was used. This required an incidence angle of 1.31° in order to satisfy the Bragg condition in second diffraction order for Cu K_α at 8.048 keV. The crystal was located at an object distance (target-to-crystal distance) of 21.4 cm resulting in a magnification of 7.92. The alignment procedure is straightforward and is discussed in details by Koch et al [9]. A 10 μm astigmatism-limited spatial resolution [9] was obtained by putting a 1.6 cm diameter aperture in front of the crystal. The geometrical size of the aperture and the source size determine the bandwidth of the crystal. Assuming a point source the minimum and maximum angles subtended by the rays coming from the source and reflecting at locations adjacent to the aperture edges are 0.36° and 2.24° respectively (Fig. A.1). The corresponding energies reflected at these angles are 8.046 keV and 8.052 keV, which gives an energy bandwidth ΔE of 6 eV. If we were to use this energy bandwidth in subsequent calculations, we would be ignoring the fact that the collection efficiency decreases as we move away from the center of the crystal. Since the aperture is circular, the area of the crystal reflecting at a constant angle of incidence is very small at $\theta_{min} = 0.36°$, increases as we move toward the center, reaches a maximum, then decreases as we move toward $\theta_{max} = 2.24°$. A plot of the collection efficiency, which is proportional to these areas, is a curve with a

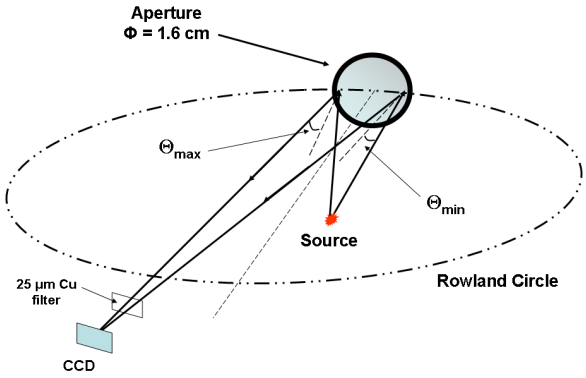

Figure A.1: Cartoon showing spherically bent Bragg crystal. The minimum and maximum angles θ_{min} and θ_{max} satisfying the Bragg condition in second order are 0.36° and 2.24° respectively. The energies reflected at these angles are 8.046 keV and 8.052 keV.

full width at half maximum $\Delta E_{fwhm} = 5.2\ eV$. It is this quantity that we use in our calculations and we refer to as the aperture energy bandwidth . The crystal viewed the rear side of the target at an angle of 37.8° with respect to the horizontal plane and 32° with respect to the target normal.

The K_α photons were collected with a Princeton Instruments CCD camera, cooled to -20 ° Celsius. The model used was PI-SX1300, which is a high sensitivity back-illuminated digital system with 1340x1300 imaging array, 20 μm pixel size, and 16-bit recording resolution. A 25 μm Cu filter was located in front of the CCD to narrow the bandwidth of the radiation reaching the detector by reducing the number of photons with energies above the Cu K-Shell photo-absorption edge. A typical monochromatic 2D spatially resolved image is shown in Fig. A.2 (500 μm x 500 μm 30 μm thick Cu target).

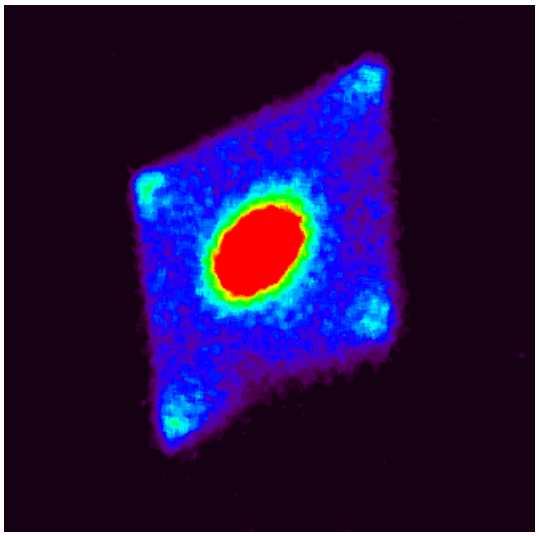

Figure A.2: A typical monochromatic 2D spatially resolved Cu K_α image. The target is a 500 μm x 500 μm 30 μm thick Cu foil.

A.2.2 Single hit CCD spectrometer

The second instrument used to collect the generated x-rays was a CCD camera operated in the single-photon counting regime. It directly detects photons without the use of any optical elements. For every 3.65 eV of photon energy absorbed in silicon a photoelectron is created. When the single photon counting condition is satisfied, the number of photoelectrons created in a single pixel is a direct measurement of the energy of the absorbed photon. In Si the absorption of a Cu K_α photon (8.048 keV) will create around 2205 photoelectrons. The ability of CCD's to operate in this mode has been demonstrated for example by Schwartz et al [10], Yasuike at al [11], Stoeckl et al [12]. We used an SI 800-145 back-illuminated CCD camera manufactured by Spectral Instrument-Photonics. This camera has a 5% quantum efficiency at 8 keV

for single hits with negligible spread of the absorbed x-rays energy over adjacent pixels [13]. It was located at a distance of 1.4 m from the target and surrounded with lead shielding to protect it from hard x-ray background and high-energy particles generated in the target chamber [12]. The photons were detected from the front side of the target at an angle of 16° with respect to the target normal [13].

A.3 Measurements of the K_α yield

The data from the imager were processed and analyzed using the Interactive Data Language (IDL), a product of Research Systems, Inc. (RSI). Background images were taken in the same environment minutes before each shot with the CCD cooled to -20 C and the filter in front of the array. The background images are then subtracted from the data images pixel by pixel. The hard hits resulting from high energy photons and particles interacting with the detector are removed from the images by applying a smoothing routine, whereby the value of a pixel is substituted by that of the median of its neighbors, if its value is higher by 10% or more than that of the median of the neighbors. The yield of K-shell emission from the target was then determined by integrating the images. The associated relative standard error was very small (0.2%-1.2%) due to the large number of photons detected .

A histogram or pulse-height-distribution of the pixel values of the single-hit CCD spectrometer allows extracting the x-ray spectrum. The absolute number of K_α yield was then determined by summing the number of hits contained in the K_α-line shape

and by taking the solid angle, filter transmission, and quantum efficiency of the CCD in single-pixel analysis mode into account [14]. An isotropic emission into a 4π steradians solid angle is assumed.

The FWHM spectral line width was determined to be 220 eV at ~ 8 keV leading to a spectral resolution of $E/\Delta E = 37$. The integral fractional number of exposed CCD pixels with Cu K-shell energy is $\sim 0.3\%$, but a significant number of pixels ($< 40\%$) are exposed to low energy events below 5 keV, which might be generated by a fractional deposition from high energy x-rays and fluorescence radiation from the inside of the CCD chamber walls. The total amount of CCD image exposure influences the calculation of the line yield and has been taken into account by the method described in Ref. [13]. Within the low level of Cu K-shell emission pixel exposure, the CCD is operating in a single-photon-counting mode. The relative error bars are estimated to be $\sim 40\%$ based on the standard deviation of several measurements at the same experimental condition. The absolute uncertainty is estimated to be a factor of 2.4 based on an estimated uncertainty in the CCD quantum efficiency for single-pixel analysis [14] and the relative measurement error.

The Cu K_α yield obtained from both instruments is normalized to the total laser energy on target and plotted as a function of the target volume (Fig. A.3). The line with diamonds indicates the total amount of Cu K_α emission collected by the single hit CCD spectrometer in absolute units (ph/sr/J). The line with x's shows the amount collected by the crystal imager in arbitrary units (a.u). With decreasing

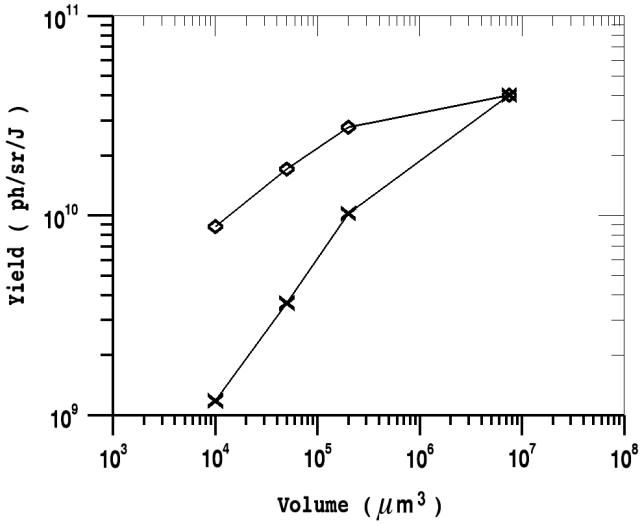

Figure A.3: Cu K_α yield: diamonds, the absolute Cu K_α emission (ph/sr/J) measured by the single hit CCD spectrometrer. x's, the integral K_α emission from the crystal imager in arbitrary units (a.u).

target volume, it is clear that the yield obtained from the crystal imager decreases faster than the yield from the single hit CCD spectrometer. This effect, attributed to the temperature-induced line shifting and broadening, is more pronounced for small targets which attain high temperatures. In principle this reduction in the yield can be used as an independent temperature diagnostic when cross calibrated with the single-hit CCD spectrometer. The data point on the top right corner is from a 500 μm x 500 μm 30 μm thick target. The remaining three data points are from 100 μm x100 μm targets with thicknesses of 1 μm, 5 μm, and 20 μm respectively.

A.4 Spectroscopic modelling of the K-shell emission

Accurate and complete modelling of K-shell emission from multiply-ionized Cu ions immersed in hot, dense plasma is difficult due to the large number of states that must be included. Apart from the complexity of the level structure, the collisional radiative kinetics cannot be treated in the standard single temperature way, since the thermal electrons that control the distribution of charge states in the M-shell have insufficient energy to participate in the inner-shell processes which produce K-alpha emission. Thus collisional rates must be calculated using non-thermal electron energy distributions. The change in the ionic potential under valence-shell ionization by the bulk thermal electrons leads to a shifting and broadening of the K_α emission feature. Modelling of this line shifting and broadening as a function of the plasma temperature was carried out using two atomic codes: the flexible atomic code (FAC) [15] and the generalized population kinetics model FLYCHK [16]. We first used FAC to compare spectra from detailed level (DL) and configuration-average (CA) models in order to test the accuracy of the CA model used later in FLYCHK for spectral synthesis. Fig. A.4 shows comparisons of spectra calculated using local thermodynamic equilibrium populations (LTE) in detailed level (DL) and configuration-average (CA) models. We have verified the statistical assumption using the collisional-radiative model SCRAM [17]. The data for each model was calculated using FAC in either

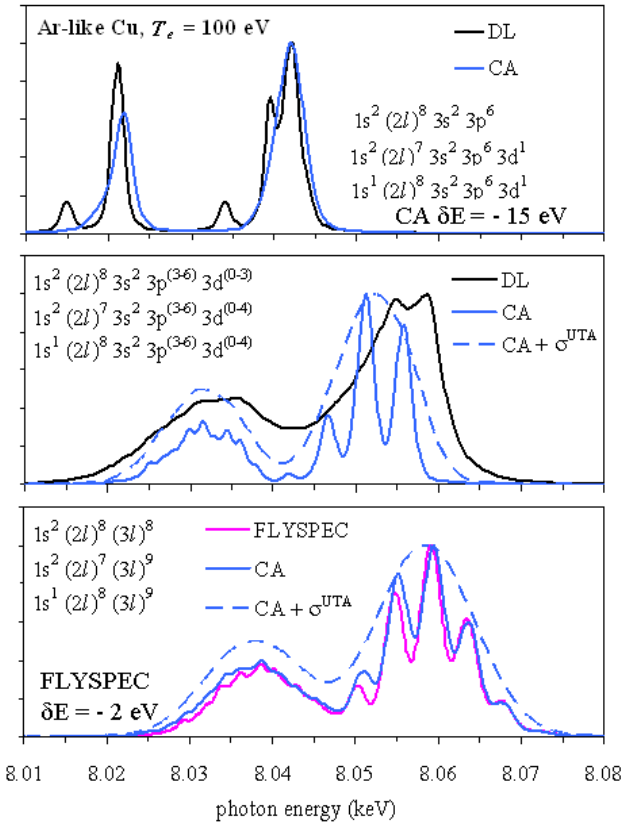

Figure A.4: Comparison of model predictions for K-shell emission from Ar-like Cu. The spectra change significantly as the number of modeled configurations is increased (top to bottom). Configuration-averaged (CA) models show reasonable agreement with detailed-level (DL) models when transition energy shifts δE and UTA widths σ^{UTA} are included.

standard (detailed fine structure) or unresolved-transition-array (UTA) mode. The two plots show the comparison of DL and CA with varying degrees of completeness in level structure. The plot on the top includes about 21 fine structure levels in the DL model of Ar-like Cu. The central plot includes about 9000 levels. The CA models for the two cases have 9 and 160 relativistic averaged levels respectively. The CA spectra are plotted with an imposed transition energy shift of -15 eV to match the predictions of the simplest DL model and are given both with and without including the UTA transition widths. While the energies of CA transition arrays within the dashed-lines envelopes are not perfectly coincident with corresponding features in the DL spectra, the centroids and overall widths of the CA features are in reasonable agreement. Therefore, for the purpose of this paper, it is adequate to use the CA model which reduces the model complexity.

In order to compute the K_α line shifts and broadening at a given thermal electron temperature, FLYCHK first computes the level population in the super-configuration model and generates emission spectra in the configuration-average (CA) model kinetics, and then FLYSPEC calculates spectra based on CA atomic data from Mau Chen's DHS code [18, 19]. FLYSPEC predictions for Ar-like Cu are in good agreement with the FAC-based CA calculations (Fig. A.4). In our experiment the hot electron temperature was about 600 keV as estimated, from the laser intensity, using Beg's scaling law [20]. The hot electron density was in the range of 10^{-4} to 10^{-3} of the total electron density. This estimate is based on experimental laser-to-electron

conversion efficiency [21] and Cu K_α spot size [6]. The total electron density is computed self-consistently by the solid ion density times the mean charge state. While the absolute K_α intensity is a function of hot electron temperature and density, the spectral shape is rather insensitive to them and depends on the thermal electron temperature as long as the fraction of hot electrons is less than 10% of total electron density, which is the case in our experiment. The calculated spectra are plotted in Fig. A.5 for thermal electron temperatures ranging from 1 eV to 300 eV along with the aperture energy bandwidth (black vertical lines).

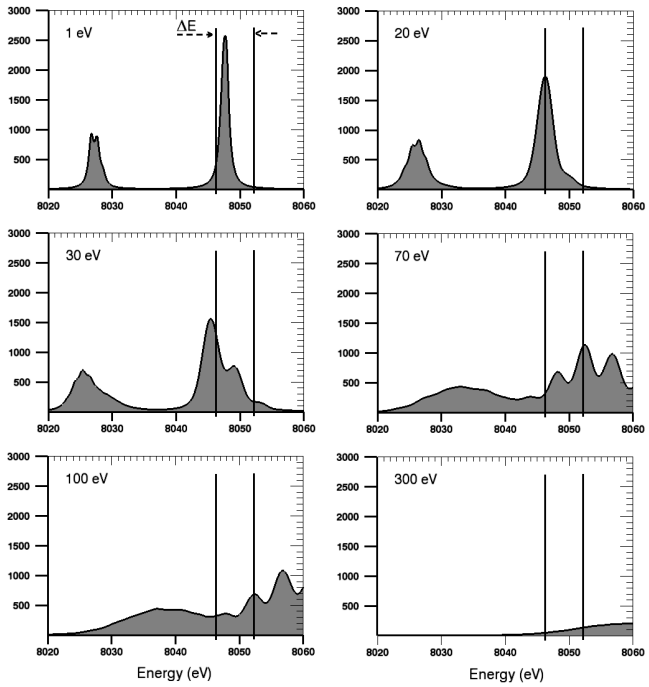

Figure A.5: FLYCHK spectra for temperatures ranging from 1 eV to 300 eV. The two vertical lines indicate the maximum and minimum energies reflected by the crystal.

A.5 Collection efficiency of the Bragg crystal imager

The Cu K_α emission line, in addition to broadening, exhibits a negative shift at first as shown by the peak moving to the left (Fig. A.5). As the plasma temperature increases, the broadening increases and the energy shifts become positive. The ratio of the area under the curve bounded by the aperture energy bandwidth to the total area under the curve is proportional to the collection efficiency of the crystal. In the calculation of the collection efficiency $\epsilon(T)$ a normalization factor was applied. The chosen normalization made the collection efficiency 100% when the target is cold ($T = 0\ eV$) and the aperture energy bandwidth centered around the cold K_α. Fig. A.6 (dashed line with triangles) shows that $\epsilon(T)$ is a decreasing function of temperature. Between 0 and 20 eV, $\epsilon(T)$ steeply decreases to about 25%.

Due to the time-integrated nature of the diagnostic, the amount of radiation collected by the imager at a given time is proportional to the collection efficiency at that time and therefore the temperature. If $Y(T)$ is the K_α yield from a $1\mu m$ solid density Cu slab at temperature T, then the yield collected by the imager at this temperature is $Y(T)\epsilon(T)$. The total yield collected when the slab is heated from T_0 to T_{max} is, therefore, given by the following integral,

$$\int_{T_0}^{T_{max}} Y(T)\epsilon(T)\ dT \tag{A.1}$$

The above integral quantity is shown in Fig. A.6 (Dotted line with x's). It in-

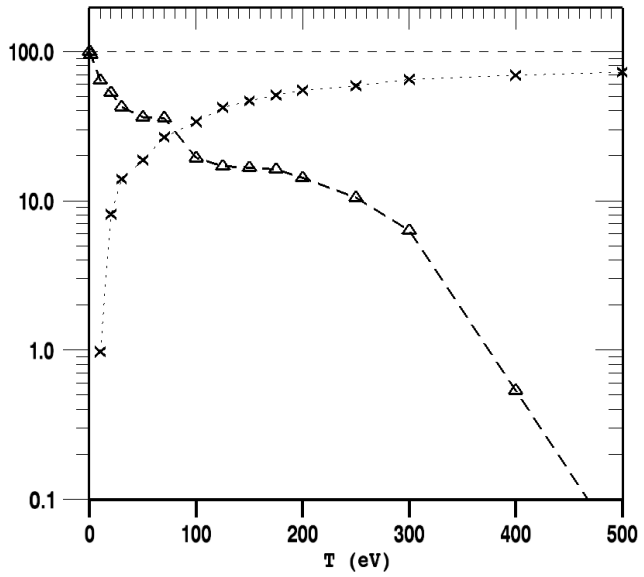

Figure A.6: Dashed line with triangles, the crystal imager collection efficiency as a function of target temperature. Dotted line with x's, total K_α yield when the slab is heated to temperature T.

creases rapidly with temperature and reaches a plateau at about 100 eV. One of the implications of this temperature-dependence of the collection efficiency is the saturation of the amount of photons collected. This effect will impose limitations on the use of spherically bent Brag crystals as diagnostics for very hot plasmas.

A.6 Numerical model

The temperature throughout the target is not constant but rather decreases with depth and radial distance from the laser focal spot. Furthermore, the interaction of the laser beam with the target is local and time varying. To account for these two effects in interpreting our data, a numerical model was developed.

The calculations are carried out in cylindrical geometry. We start with modelling the laser pulse using the following double Gaussian profile, based on the experimentally measured focal spot,

$$I_{Laser}(r,t) = \exp\left[-\left(\frac{t-t_p}{\tau}\right)^2\right]\left\{ I_1 \exp\left[-\left(\frac{r}{R_1}\right)^2\right] + I_2 \exp\left[-\left(\frac{r}{R_2}\right)^2\right]\right\} \tag{A.2}$$

here $R_1 = 5\ \mu m, R_2 = 40\ \mu m$, $I_1 = 5 \times 10^{18}\ W/cm^2$, $I_2 = 1 \times 10^{17}\ W/cm^2$, $t_p = 5\ ps$, and $\tau = 2.5\ ps$.

The hot electrons generated by the interaction of this pulse with the target are described by a local Maxwellian distribution,

$$f_E(E,r,t) \propto \frac{\sqrt{E}}{T_h(r,t)^{3/2}} \times \exp\left[-\frac{E}{T_h(r,t)}\right] \tag{A.3}$$

where the local temperature, $T_h(r,t)$, is given by Beg's scaling law [20].

The number of hot electrons in each zone of radius r is calculated from their local total energy and their mean energy. Their mean energy is simply $\frac{3}{2} \times T_h(r,t)$. Their local total energy is $\eta_L \times E_{Laser}(r,t)$, where η_L is an intensity dependent laser-to-electrons conversion efficiency taken from Key et al. [21]. The calculations are carried out in concentric cylindrical zones of radii r and length Δz. Although this approach ignores electron scattering, it accounts for electron resistive inhibition [22, 23] for thick targets and refluxing [24, 13] for thinner ones.

For thick targets, the temperature in each zone, $T(r,z,t)$, is determined from the specific energy deposited using LANL SESAME equation of state tables. The energy

deposited has two components: collisional and Ohmic. The contribution of collisions is determined using the stopping power of electrons in hot plasmas from reference [25, 26],

$$\frac{dE}{ds} = -\frac{2\pi r_0^2 mc^2 n_i Z}{\beta^2} \times \left[\ln \left[\frac{(\gamma-1)\lambda_D}{2\sqrt{2\gamma} r_0} \right]^2 + 1 + \frac{1}{8} \left(\frac{\gamma-1}{\gamma} \right)^2 - \left(\frac{2\gamma-1}{\gamma} \right) \ln 2 \right] -$$

$$- \frac{2\pi r_0^2 mc^2 n_i Z}{\beta^2} \times \ln \left(\frac{1.123\beta}{\sqrt{2kT_h/mc^2}} \right)^2 \tag{A.4}$$

The Ohmic component is proportional to the square of the neutralizing return current density. For $T(r,z,t) < 100$ eV the resistivity is approximated by its maximum value of 10^{-6} $(\Omega \cdot m)$ at the plateau [27] and above 100 eV the Spitzer resistivity is used. In each step the influence of the potential on the energy of the electrons is accounted for. The return current density is given by the following expression:

$$\overrightarrow{j}_{return}(r,z,t) \approx -\overrightarrow{j}_{fast}(r,z,t) = e \int c\ \beta(E)\ n_h(r,z,t,E)\ dE\ \frac{\overrightarrow{z}}{\|\overrightarrow{z}\|} \tag{A.5}$$

where $n_h(r,z,t,E)\ dE$ is the number of hot electrons per unit volume with energies between E and $E + dE$ in a zone with given (r,z) at time t.

For thin targets the situation is different. The electrons traverse the target and set up an electrostatic sheath of thickness of the order of Debye length. The sheath was characterized by the electric field strength of order $T_h(r,t)/e\lambda_D$. The Debye length,

λ_D, is a function of the electron density and temperature. These last two quantities are functions of time. Therefore the potential which is the product of electric field strength and Debye length is also a function of time. The first electrons created by the leading edge of the laser pulse at earlier time establish a sheath with a potential $\varphi(t_0)$. This potential is not strong enough to influence the electrons. The incoming electrons at later time increase the magnitude of the potential due to more charge separation. In the calculation, this potential is evaluated as a function of time. When the value of $\varphi(t)$ is equal to their mean energy, electrons coming at that time reflect from the rear surface. These electrons are also reflected from a similar Debye sheath at the front surface. The process is repeated for the lifetime of the electrons, hence the name "refluxing". The first electrons establishing the sheath are not circulated. The specific energy deposited in the target is due to collisions only, the electrons act as their own return current by virtue of refluxing.

The distribution, $N_{ph}(r, z, t)$, of K_α photons induced by these electrons is then calculated according to,

$$N_{ph}(r, z, t) = \int n_{Cu}\ \Delta z\ \sigma(E)\ N_h(r, z, t, E)\ dE \tag{A.6}$$

where $N_h(r, z, t, E)\ dE$ is the number of hot electrons with energies between E and $E+dE$ in the zone, n_{Cu} is the copper number density, and $\sigma(E)$ is the electron impact ionization cross section in Cu. For $\sigma(E)$ we used the Deutsch-Mark expression,

$$\sigma(E) = 2\pi\ r_{1s}^2\ g_{1s}\ f\left(\frac{E}{E_{1s}}\right)\ F\left(\frac{E}{E_{1s}}\right) \tag{A.7}$$

where r_{1s} is the radius of maximum radial density of Cu 1s-shell from the tables of Desclaux [28], g_{1s} is a weighting factor, E_{1s} is the binding energy of 1s electrons, and the functions f, F are those in reference [29].

A.7 Discussion and Summary

A.7.1 Absolute yield and spatial pattern of intensity

The numerical model described above can run in either "refluxing" or "non-refluxing" modes. When refluxing is included, the model reproduces the experimental results only for targets with thicknesses less than or equal to 20 microns. The "non-refluxing" mode reproduces the experimental result for the 30 microns thick target but overestimates the yield for targets less than or equal to 20 microns. In between, a transition region exists where a combination of the two modes is needed. We consider a target to be thin if electron refluxing is dominant and thick if the refluxing can be neglected. Therefore, based on this definition, the targets with thicknesses less than or equal to 20 microns are thin. The total number of photons per steradian from the target is given by the following integral,

$$N_T = \frac{1}{4\pi} \int \int \int N_{ph}(r, z, t) \exp -\{\mu(s - z)\} \; dt \; dz \; dr \tag{A.8}$$

here μ is the attenuation coefficient of K_α radiation in Cu. N_T is plotted as a function of the target volume in Fig. 7 (dashed line with triangles). It is in good agreement with the experimental data from the single hit CCD spectrometer (solid line with

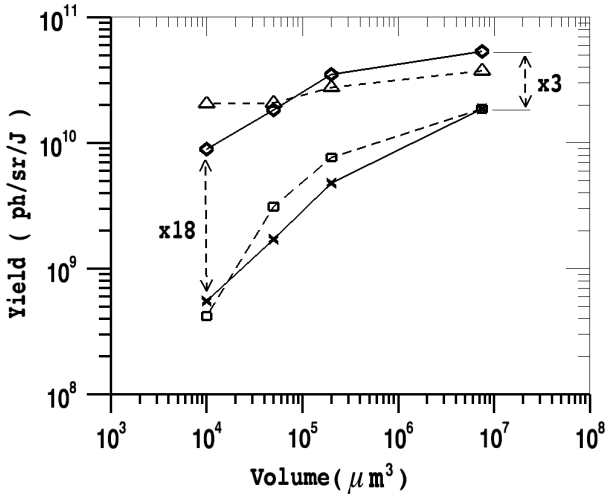

Figure A.7: Comparison of the experimental and modeled absolute K_α yields. Experimental: solid line with diamonds from the single hit CCD, solid line with x's from the crystal imager normalized as discussed in the text. Modeled: dashed line with squares, the yield from the imager with temperature effects. dashed line with triangles, the absolute yield.

diamonds). The experimental yield from the 1 μm thick target is little lower than the modelled. The reason for this may be that the electrons lose their energy to channels other than electron impact ionization (pdV work accelerating protons for example). When the previously determined collection efficiency correction is applied, the total number of photons per steradian collected by the imager is reduced to:

$$N_{T_r} = \frac{1}{4\pi} \int \int \int N_{ph}(r,z,t) \exp -\{\mu(s-z)\} \; \epsilon(r,z,t) \; dt \; dz \; dr \qquad \text{(A.9)}$$

where $\epsilon(r,z,t)$ is the local collection efficiency.

N_{T_r} is plotted in Fig. A.7 (dashed line with open squares). Also plotted are the experimental data from the imager (solid line with x's). The value of N_{T_r} for the 30 μm thick target was used as a normalization point for the experimental data since

these data were not measured in absolute units. The thickest target was chosen based on the fact that it is the least susceptible to temperature effects. The single hit CCD data were corrected for the reabsorption in the target material by comparing the yields obtained from the model with and without the attenuation on. The corrections were 25%, 21%, 6%, and 1% for the 30 μm, 20 μm, 5 μm, and 1 μm thick targets respectively. Both the modelled and experimental results are in a good agreement, showing the temperature-dependence of the collected K_α yield. The total yield was reduced by a factor of 3 for the thickest target and by a factor of 18 for the thinnest one.

As an example, the model is applied to the spatial pattern of K_α intensity for the 30 μm thick target. A useful approach in analyzing 2D spatially resolved images is a lineout through the image. Such a lineout is plotted in Fig. 8 (dashed line with triangles). It was taken in the horizontal direction through the middle of the K_α image of Fig. 2. The dashed line is the modelled lineout with the line shifting and broadening taken into account. The solid line is the true lineout that one should expect if the imager were not susceptible to temperature effects. the reduction was almost uniform ranging from 62% in the center to 56% at the edges. As consequence the full width at half maximum remained unchanged while the brightness of the image is reduced. For thinner targets, the reduction was more pronounced at the center than the edges. This resulted in an apparent increase in the FWHM. Neglecting these effects when interpreting data will lead to erroneous results for the FWHM more so in case of high

temperatures.

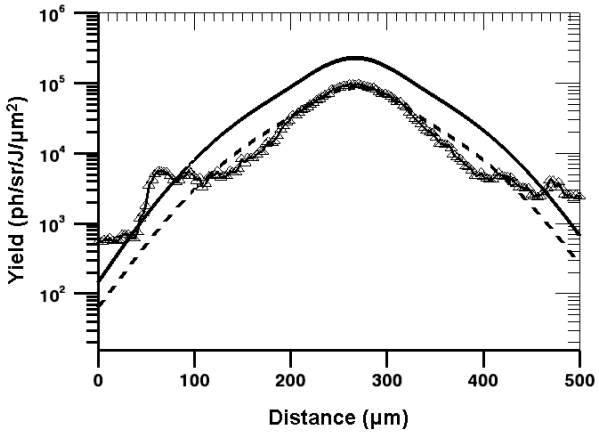

Figure A.8: Cu K_α spatial pattern of intensity: solid line with triangles, a horizontal lineout of the image of the 500 μm x 500 μm 30 μm thick target in Fig. 2. Solid line, model lineout with no temperature effects. Dashed line, model lineout with temperature effects.

A.7.2 Isochoric heating

The reduction in collected K_α photons can be used as a temperature diagnostic. Since this diagnostic is time integrated, only an average temperature can be inferred. This is done by determining the yield reduction curve from that of the collection efficiency $\epsilon(T)$ of Fig. A.6. The reduction in the K_α yield ,

$$R(T) = \frac{\int_0^T \epsilon(T')\ dT'}{\int_0^T \epsilon_{cold}(T')\ dT'} \tag{A.10}$$

defined as the ratio of the area under the $\epsilon(T)$ curve to the area under $\epsilon_{cold}(T)$ curve, is plotted in Fig. A.9-a. The quantity $\epsilon_{cold}(T)$ is the collection efficiency in

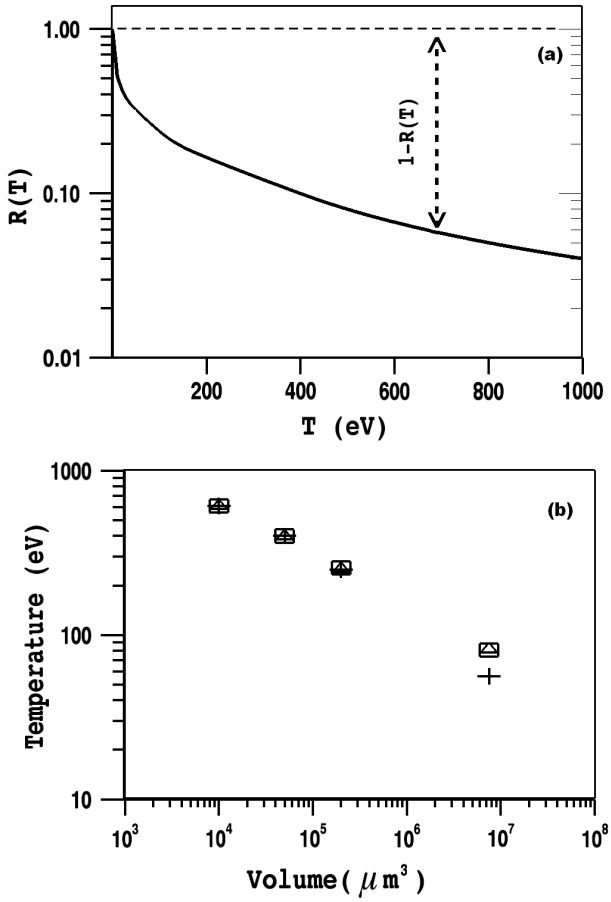

Figure A.9: reduction curve

the absence of shifting and broadening. Using Fig.(A.7) to determine the ratios, the temperature of the targets is determined by finding the temperature that produces the same reduction in Fig. A.9-a. The experimental ratios were 0.32, 0.13, 0.09, and 0.06 corresponding to temperatures of 82 eV, 253 eV, 400 eV, and 610 eV for the 30 μm, 20 μm, 5 μm, and 1 μm thick targets respectively. These average temperatures are plotted in Fig. A.9-b. The errors due to the uncertainty in the 2d spacing of the

crystal were estimated as follows. From previous experiments using the same crystal and the same laser system, we have imaged cold Cu K_α line [6]. Since the crystal was set to an angle of 1.31 degrees, a cold K_α line with 2.0 eV full width at half maximum linewidth would be imaged only if the 2d spacing is between $2d_{min} = 3.0816\ \mathring{A}$ and $2d_{max} = 3.0824\ \mathring{A}$ angstroms as illustrated in Fig. A.10. As long as the intersection of the 2d curves with the vertical axis $\Theta = 1.31^\circ$ lies within the grey area an image will be recorded.

Similar curves to the ones in Fig. A.6 were obtained for $2d_{min}$ and $2d_{max}$. These efficiency curves were, then, used to determine the temperatures of the targets (Triangles and pluses in Fig. A.9-b). At high temperatures, the error introduced is less than 1% for both $2d_{min}$ and $2d_{max}$. This small error is due to the broadening of the K_α line at high temperatures. At low temperatures, the error is 32% for $2d_{min}$ due to the fact that the K_α line is still narrow and starts, initially, to shift away from the aperture energy bandwidth ($8.047 - 8.052\ keV$). The aperture energy bandwidth for $2d_{max}$ extends from 8.045 keV to 8.050 keV. The initial shift of K_α line is in the direction of lower energies which brings it toward the center of the bandwidth. As a result, the error is less than 1.2%.

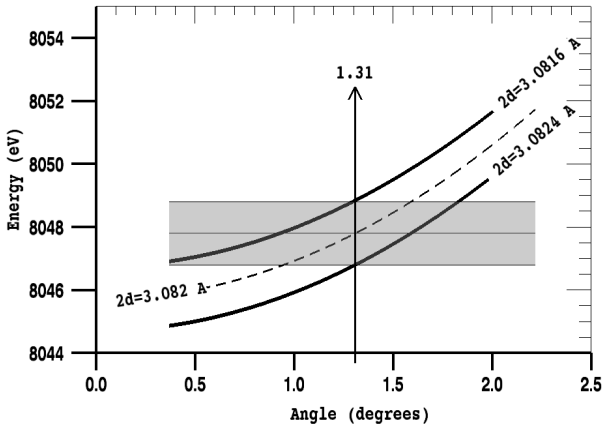

Figure A.10: 2d ratio

In summary, experimental evidence of temperature sensitivity of Cu K_α imaging efficiency using a spherical Bragg reflecting crystal was presented. The experimental data were interpreted using two models. First, the temperature-dependent spectrum of Cu K-shell emission was modelled using FLYCHK in the configuration-average (CA) mode. Then, a numerical transport model which takes into account the electron refluxing was used to obtain both the absolute K_α yield and the spatial pattern of K_α intensity. It was found that both the brightness and the pattern of K_α intensity are affected by the rise of the target temperature. The reduction in the absolute K_α yield was used to determine the average temperature of the targets. The errors introduced by the uncertainty in the 2d spacing were found to be insignificant at high temperatures. At low temperatures, the error can be small or big depending on the location of the aperture energy bandwidth and the initial shift of the K_α line (away or toward the bandwidth).

Bibliography

[1] J. A. King, Rev. Sci. Instrum **76**, 076102 (2005).

[2] D. B. Sinars, Rev. Sci. Instrum **74**, 2202 (2003).

[3] J. A. Aglitsky, Phys. Rev. Lett **87**, 265001 (2001).

[4] M. Tabak, Phys. Plasmas **1**, 1626 (1994).

[5] M. H. Key, Inertial Fusion Sciences and Applications (IFSA) (2003).

[6] R. B. Stephens, Phys. Rev. E **69**, 066414 (2004).

[7] G. Gregori and S. B. Hansen, Contrib. Plasma Phys **45**, 284 (2005).

[8] D. Strickland and J. Mourou, Opt. Commun **56**, 219 (1985).

[9] J. A. Koch, Rev. Sci. Instrum **74**, 2130 (2003).

[10] D. A. Schwartz, Proc. SPIE **184**, 247 (1979).

[11] K. Yasuike, Rev. Sci. Instrum **72**, 1236 (2001).

[12] C. Stoeckl, Rev. Sci. Instrum **75**, 3705 (2004).

[13] W. Theobald, Phys. Plasmas **13**, 043102 (2006).

[14] H. S. Park, Phys. Plasmas **13**, 056309 (2006).

[15] M. F. Gu, AIP Conference Proceedings **730**, 127 (2004).

[16] H. K. Chung, High Energy Density Physics (HEDP) **1**, 3 (2005).

[17] S. B. Hansen, Ph.D. thesis, University of Nevada, Reno (2003).

[18] M. H. Chen, Phys. Rev. A **31**, 556 (1985).

[19] K. N. Huang, At. Data and Nucl. Data Table **18**, 243 (1976).

[20] F. N. Beg, Phys. Plasmas **4**, 447 (1997).

[21] M. H. Key, Phys. Plasmas **5**, 1966 (1998).

[22] A. R. Bell, Plasma Phys. Controlled Fusion **39**, 653 (1997).

[23] D. J. Bond, Phys. Rev. Lett **42**, 252 (1980).

[24] A. J. Mackinnon, Phys. Rev. Lett **88**, 215006 (2002).

[25] C. K. Li, Phys. Rev. E **70**, 067401 (2004).

[26] C. K. Li, Phys. Rev. E **73**, 016402 (2006).

[27] H. M. Miltchberg, Phys. Rev. Lett **62**, 2364 (1988).

[28] J. P. Desclaux, Atom. Data Nucl. Data Tables **12**, 325 (1973).

[29] H. Deutsch, International Journal of Mass Spectrometry **213**, 5 (2002).

Appendix B

Manuscript submitted to Physical Review Letters.

Fast ignition relevant study of the flux of high intensity laser generated electrons via a hollow cone into a laser-imploded plasma

M.H. Key [1], J C Adam [9], K.U. Akli [1,3], M. Borghesi [7], M. H. Chen [1], R.G. Evans [6], R.R. Freeman [3,5], H. Habara [10], S. P. Hatchett [1], J. M. Hill [5], A. Heron [9], J.A. King [1], R. Kodama [10], K. L. Lancaster [2], A.J. MacKinnon [1], P. Patel [1], T. Phillips [1], L. Romagnani [7], R. A Snavely [1], R. Stephens [4], C. Stoeckl [8], R. Town[1], Y. Toyama [10], B. Zhang [3],M. Zepf [7], P.A. Norreys [2]

[1] University of California, Lawrence Livermore National Laboratory,USA

[2] Rutherford Appleton Laboratory, United Kingdom

[3] Department of Applied Science,University of California, USA

[4] General Atomics, San Diego, CA, USA 92186, USA

[5] College of Mathematical and Physical Sciences, The Ohio State University, USA

[6] Blackett Laboratory, Imperial College of Science Technology and Medicine, UK

[7] Depent of Pure and Applied Physics, Queens University of Belfast,UK

[8] Laboratory for Laser Energetics, University of Rochester, USA

[9] Centre de Physique Thorique, Ecole Polytechnique, France

[10] Institute of Laser Engineering, Osaka University, Japan

abstract

An integrated experiment relevant to fast ignition is described. A Cu doped CD spherical shell target is imploded around an inserted hollow Au cone by a six beam 600 J, 1ns laser. A 10 ps, 20 TW laser pulse is focused into the cone at the time of peak compression. The flux of high-energy electrons through the imploded material is determined from the yield of Cu K fluorescence by comparison with a Monte Carlo model and is estimated to carry 15% of the laser energy. Collisional and Ohmic heating are modeled. An electron spectrometer shows significantly greater reduction of the transmitted electron flux than is due to binary collisions and Ohmic potential. Enhanced scattering by instability-induced magnetic fields is suggested.

PACS numbers: 52.50.Jm, 52.38.Ph, 52.70.Kz

Fast ignition (FI) of inertial confined fusion [1] may lead to higher gain, reduced ignition threshold, less stringent driver uniformity and target smoothness requirements and thus better prospects for inertial fusion energy [2]. The first integrated experiments demonstrated more than 20% efficient coupling of 1 ps pulse laser energy to a long pulse laser imploded plasma using first 60J [3, 4] , and then 350J [5] pulses. Modeling [6] shows that at least 14kJ of particle energy is required to ignite compressed DT plasma at a density of 300gcm-3. The experimental 20% coupling efficiency implies that at approximately 70kJ of laser energy would be needed. In order to generate the required 1 to 2 MeV electron energy in less than the 33 μm

ignition hot spot diameter, the laser pulse must have an appropriate intensity. Constraining the intensity leads to pulse duration close to the inertial confinement time limit of 10 to 20 ps and significantly longer than used to date [3, 5]. We report the first integrated experiment using 10ps pulses.

The electron flux through the implosion was measured from Cu K fluorescence induced from Cu atoms doping the deuterated polyethylene (CD) shell. This method gives the greatest yield of K where the density is highest [7].

Six orthogonal beams from the Vulcan laser [8] drove the implosion. They had jitter free synchronization with a chirped pulse amplification (CPA) short pulse, both long and short pulses being derived from the same seed pulse. The implosion drive was 0.9kJ in 1ns at 1.05 μm wavelength, with an approximately Gaussian pulse shape. The beams were focused with f/2.5 lenses with the marginal rays tangential on the micro-balloon targets. These were unfilled spherical CD shells doped at 0.7 atomic % with Cu and typically 486 μm in diameter and 6 m thick. An Au hollow cone inserted in the shell was 10 μm thick at its tip, which had a 30 μm flat end, located 40 μm from the center of the shell. The tapered Au thickness increased to 40 μm at the wall of the shell. The cone length was 1mm with an exterior full angle of 44° and an interior full angle of 26°.

Diagnostics included a single hit CCD spectrometer recording Cu K , a monochromatic spherical crystal imager of Cu K_α and an electron spectrometer. The experimental configuration is described more fully elsewhere together with detailed char-

acterization of the implosion trajectory and density by ps pulse Ti K radiography [9] and multi-MeV proton radiography [10], hydrodynamic modeling with the Hydra code and estimation of the implosion temperature.

X-ray pinhole camera images showed good drive irradiation symmetry. The absence of detectable imploded core x-ray emission or D-D fusion neutron emission indicated a cool implosion. The key measured implosion parameters were; time of peak compression 3.2 ns after the peak of the drive pulse, compressed plasma diameter 100 m, peak density, 4 g/cm^3 and density x radius product, $20mg/cm^2$. These conditions are particularly relevant for FI being close in density and temperature to the cone tip conditions in full scale FI designs and therefore providing a test bed for possible unstable transport at the cone tip.

The average short pulse energy on target was 70 J with a peak intensity of 3×10^{18} W/cm^2. From focal spot images, half the power was delivered at a vacuum intensity less than 0.1x the peak intensity. The temperature of the source of electrons at critical density is expected to be similar to the 400 keV ponderomotive potential at the peak intensity There was an amplified spontaneous emission (ASE) pre-pulse with 10^{-4} of the main pulse energy and 3×10^{-7} of the intensity for a few ns prior to the main pulse. This created sub-critical density plasma with a scale length at critical density of about 3 μm inferred from 2 dimensional hydrodynamic modeling. Self-focusing in the preformed plasma can enhance the laser intensity and sub- critical density electron acceleration processes generate electrons with temperatures higher

than the ponderomotive energy, producing a higher temperature tail on the energy spectrum. The cone can also guide and concentrate both laser energy and electrons at its tip . These factors together determine the characteristics of the electron source.

Electron energy spectra along the axis of the CPA beam were obtained with a magnetic deflection spectrometer using image plate detection [9]. Spectra are shown in figure 1. The temperature of the spectrum is about 1.3 MeV in the 2 to 6 MeV range for a free standing cone. The energy spectrum of electrons escaping into vacuum is only indirectly related to that of the generated electrons. A few percent of the electrons escape, the rest being trapped by formation of a Debye sheath at the target surface. Escaping electrons lose energy to the sheath potential. The sheath potential also varies in time. For a fixed sheath potential and a Boltzmann energy spectrum, the escaping electrons have the same temperature as the source electrons. For a two-temperature distribution the sheath potential traps the lower energy electrons so that escaping electrons have a higher temperature. As discussed earlier, we expect a multi- temperature distribution with the higher energies having higher temperature; consequently the 1.2 MeV slope temperature of the energy spectrum in figure 2 is not inconsistent with $3 \times 10^{18}\ W/cm^2$ peak intensity of the irradiation.

The yield of Cu K fluorescence was measured with a single hit CCD spectrometer, (Spectral Instruments x-ray CCD camera with a 2048x2048 pixel back-thinned CCD chip with a pixel size of 13 μm recorded with 16-bit resolution) from the rear of the target at an angle of 27° relative to the CPA beam. The absolute yield was determined

from knowledge of the quantum efficiency, the subtended solid angle and the filter transmission [14].

The data in figure 2 show the spectrum from a 20-μm thick Cu foil irradiated at low energy (20J) exhibiting the expected ratio of K_α and K_β for cold Cu K shell fluorescence. The spectrum from a full energy coned target implosion with the short pulse timed to coincide with peak compression is also shown in figure 2. The absence of K_β is attributed to thermal ionization of M shell electrons in Cu. Multi-configuration Dirac Fock (MCDF) calculations [15] were used to compute how K_β is reduced in intensity relative to K_α, shifted to higher energy and broadened with increasing ionization. The 9×10^6 cm/s peak velocity of the implosion implies temperature at stagnation of 75 eV and this causes ionization to Cu^{9+}. The MCDF calculations indicate that for Cu^{9+}, the K_β line is suppressed by an order of magnitude. Relevant also is that ionization effects shift and strongly broaden the K_α line relative to the 2 eV Cu K spherical Bragg crystal imager bandwidth as discussed later. The maximum measured yield from an implosion was 1.1×10^{11} K_α photons per steradian.

Null tests were conducted with long pulse ablation only of the Cu doped CD micro-balloon and no detectable K_α yield was observed with the CCD spectrometer. Imaging with the Bragg crystal imager showed only extremely weak Cu K_α emission from the ablation region with sparse single hits [9]. The single hit image suggests a powerful future diagnostic for integrated FI experiments with full scale imploded plasmas being designed at the NIF using very large CCD arrays for single hit imaging

of Kalpha fluorescence . Cross calibration with the CCD spectrometer showed that this corresponded to $<$ 2% of the signal recorded by the CCD spectrometer. The Bragg crystal imager also showed no emission from the implosion core and this is consistent with the low efficiency of imaging the shifted and broadened K emission spectrum for the 75 eV temperature of the implosion inferred from the implosion dynamics . We conclude that the spectrum in figure 2 is emitted from the imploded plasma. This understanding is a significant change relative to an earlier preliminary analysis [9]. The absence of implosion core emission in the x-ray pinhole camera images and absence of D-D thermonuclear yield put upper bounds of 250eV and 750 eV respectively on the short pulse heating of the implosion core.

To interpret these data we first used Monte Carlo modeling with ITS (the integrated Tiger series of coupled Monte Carlo Transport Codes [17]) with a variable assumed Boltzmann temperature in the electron source. 10^6 electrons were injected uniformly via a 30-μm-source diameter (the tip of the cone) in a 30° cone angle (similar to experimental observations of the cone angle of electron transport we made earlier [7]), and the injection plane was located 40 mum from the center of the density profile in figure 4. The K_α yield was computed using the collision cross-section and the total energy in the electrons was obtained by scaling their number to fit the experimentally measured K_α yield. Sensitivity to changes in the assumed source area and cone angle of the electrons was found to be slight because of the rather large imploded plasma. Sensitivity to the peak density in the implosion assuming conser-

vation of mass, was such that if the density were higher the deduced energy in the electrons would be reduced as $\rho^{-2/3}$. The greatest sensitivity was to the electron temperature as shown in figure 3 where the conversion efficiency of laser energy to energy in the electron beam is plotted as a function of the assumed source temperature.

The source temperature as discussed previously is a distribution which has an upper bound of 1.2MeV measured by the electron spectrometer and at its low end includes the ponderomotive potential estimate of 0.4 MeV. The mean is 0.75 MeV and at this temperature figure 3, implies a conversion efficiency of 15% of the laser energy to electrons. Taking the previously discussed temperature extremes a conservative range of uncertainty is from 7% to 22%.

A model was formulated to examine the effects of Ohmic and collisional heating using as input the measured 15% of total energy and 0.75 MeV temperature of the electron source. The density profile of the CD and the initial temperature were those deduced from the radiography and modeling of the implosion respectively. The geometry of the electron injection was the same as used in the MC model. Plasma resistivity has its maximum value [18] at a plateau around 30 to 50 eV with decreasing resistivity at higher temperatures in the Spitzer regime at $> 100\ eV$. In the model it was approximated iteratively as the value at the average temperature and density resulting from the analysis (which was $3 \times 10^{-7}\ Ohm.m$ from the Sesame tabulation [19]). The energy deposited per unit mass was calculated by injecting electrons in energy bins and calculating their collisional energy loss (using a recent analytic model

for electrons in plasma [20]) and their Ohmic potential energy, stepping through axial zones along the axis of the energy transport and assuming an equal return current density. The associated collisional and Ohmic heating were also calculated, Temperature rise was approximated as that in classical plasma ionized to C4+. Hydrodynamic and thermal conduction effects were neglected. Figure 4 shows the results.

The temperature maximum was 166 eV located at the entry plane. It is well below the upper bounds from the x-ray phc and neutron data. The combined Ohmic and collisional heating is greatest at the entry plane because there the electron flux density is highest and the density is lowest. Ohmic heating contributes only modestly to the temperature rise as evidenced by the plot in figure 4 with no Ohmic heating. The 10 keV maximum potential is significantly smaller than the 750 keV electron temperatures. The relatively small range of deduced temperatures in figure 4 makes the approximation of constant resistivity adequate for the estimates made here. The fraction of the injected electron energy absorbed in the target is 9%, a low value consistent with the small mass per unit area and small Ohmic potential.

The electron spectrometer showed in figure 1, that when the imploded plasma was present there was at least an order of magnitude reduction in the electron signal in the range 2 to 5 MeV. In most shots there was a greater than 2 order of magnitude reduction to an un-detectable level. These data imply either enhanced energy loss or strong scattering. Electron spectrometer data from Kodama et al [4] showed a similar but less pronounced reduction. Both effects may be connected with strong excitation

of Weibel-like and two stream instabilities with associated turbulent magnetic fields. 2D particle in cell (PIC) modeling has shown that the resulting B fields can strongly scatter the fast electrons [21]. They can also create a transport barrier by scattering of the return current generating an anomalous resistivity and large Ohmic potential [22]. A 100 fold enhanced resistivity in the heating model was needed to stop the penetration of most of the electrons, but it raised the temperature in the entry region above 3 keV to a level inconsistent with the absence of thermonuclear neutron and x-ray emission from the heated implosion. Enhanced scattering is therefore a more plausible explanation. Linear analysis [23, 24] gives the growth exponent of the Weibel-like instability, which we estimate at 200 where the electron beam enters the CD plasma [21] and 2D PIC numerical modeling [19] for similar injected beam conditions shows strong scattering of the fast electrons. This could be an important issue for fast ignition and needs further study.

In conclusion we have made the first measurement of electron energy transport via an imploded plasma in a fast ignition cone inserted target using a 10 ps pulse duration similar to that required for full scale experiments. We have developed a new K fluorescence diagnostic to determine the efficiency of converting laser energy to electron energy injected into an implosion. Our results suggest that about 15% of the laser energy is converted to electron energy traversing the implosion. The data also show attenuation of the electron flux density recorded in vacuum, which is best explained by scattering from instability generated B fields.

Acknowledgements.

We thank R Petrasso for advice on electron energy loss in plasma and we are grateful to the staff of the Central laser facility, in particular J. Collier, S. Hawkes, R. Heathcote, C. Hernandez-Gomez, D. Neely and M.H.R. Hutchinson for their support. Work performed under the auspices of the U.S.. Department of Energy by the Lawrence Livermore National Laboratory under Contract No. W-7405-ENG-48 and with grant support (GR/R16778) from the UK EPSRC. One of us (MZ) thanks the Royal Society for a Wolfson research merit award.

References

[1] N.G. Basov, S.Y. Guskov and L.P. Feokistov, J. Sov. Laser Res. 13, 396 (1992). And M Tabak et al Phys Plasmas 1 1626 (1994)

[2] M H Key et al J Fusion Energy 17, 231 (1998)

[3] R Kodama et al Nature 412,798 (2001)

[4] M H Key Nature 412, 775 (2001)

[5] R Kodama et al. Nature 418, 933 (2002)

[6] S Atzeni Phys Plasmas 6 3317 (1999)

[7] R.B. Stephens et al. Phys. Rev E. 69, (2004)

[8] C. N. Danson et al J. Mod. Opt. 45, 1653 (1998)

[9] P. Norreys et al Phys Plasmas .11,2746, (2004) and J A King et al Appl. Phys. Lett. 86,191501, (2005)

[10] A J MacKinnon et al Rev Sci. Instr. 75, 3531, 2004) and Phys Rev. Lett. (In

press)

[12] S. P. Hatchett Nucl Fusion

[13] Y. Sentoku et al Phys Rev E 11, 3083, (2004)

[14] C. Stoeckl et al., Rev. Sci. Instrum. 75, 3705, (2004)

[15] M. H. Chen, Phys. Rev. A 31, 1449 (1985)

[16] J. A. Koch et al., Rev. Sci. Instrum. 74, 2130 (2003)

[17] J A Halbeib and T A Melhorn. Sandia National Laboratory Report $\#SAND84-0573$ (1984)

[18] H. M. Milchberg et al., Phys. Rev. Lett. 62, 2364 (1988) and Y. T. Lee and R. M. More, Physics of Fluids 27, 1273 (1984)

[19] S P Lyon and J D Johnson. Los Alamos National Lab Report LA-UR-92-3407 (1992)

[20] C K Li and R D Petrasso, Phys. Rev. E, 70,1 (2004)

[21] J C Adam et.al. to be published

[22] Y Sentoku et al. Phys Rev Lett.90, 155001(2003)

[23] J M Hill et al. Phys. Plasmas 12, 082304 (2005)

[24] C Deutsch et al. Phys. Rev. E, 72,026402, (2005)

Figures

Figure 1. Electron energy spectra from a free-standing cone (1) and via an implosion (2).

Figure 2. (a) The single hit CCD Cu K shell fluorescence spectrum from an imploded shell and (b) from a Cu foil at low energy.

Figure 3. Conversion fraction of laser energy to energy in electrons traversing the implosion as a function of the temperature of the electrons.

Figure 4. Heating model: solid line, density (x50) gcm^{-3}, line with squares, Ohmic potential (x5) keV, dashed line, temperature in eV. dotted line, temperature with no ohmic heating in eV.

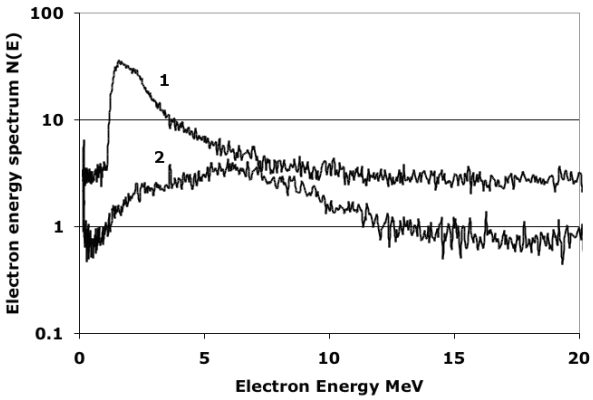

Figure B.1: Fig 1

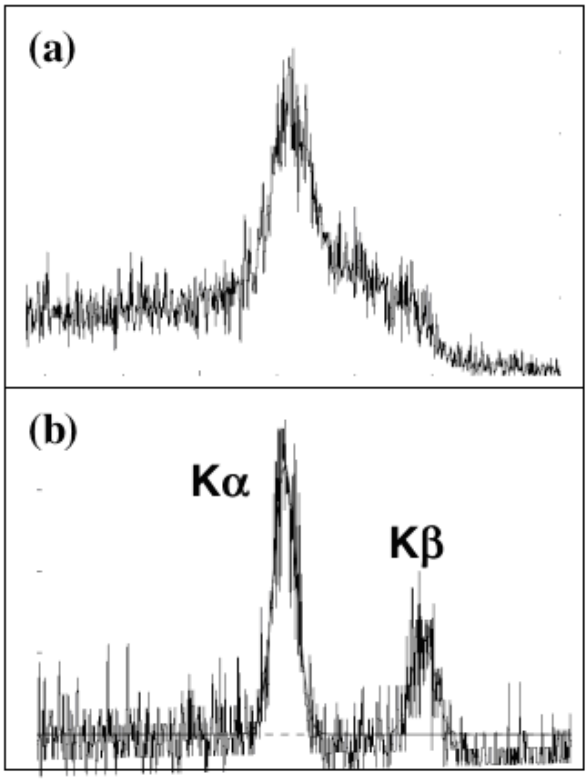

Figure B.2: Fig 2

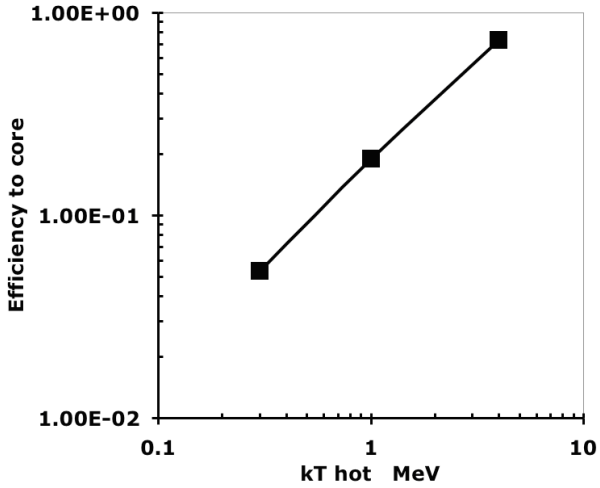

Figure B.3: Fig 3

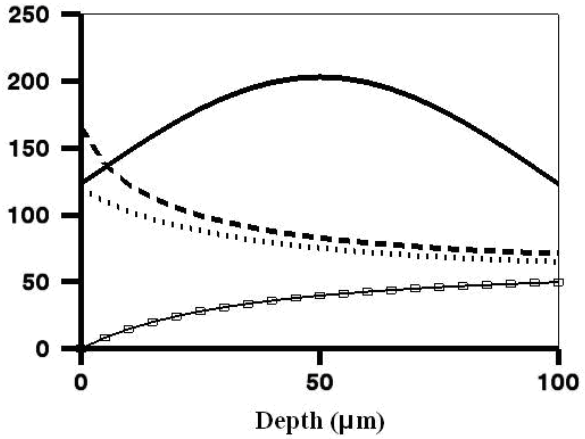

Figure B.4: Fig 4